Title
Design principles for oxide thermoelectric materials

Author
Gaultois, Michael William

Publication Date
2015

University of California
Santa Barbara

Design principles for oxide thermoelectric materials

A dissertation submitted in partial satisfaction
of the requirements for the degree

Doctor of Philosophy
in
Chemistry

by

Michael W Gaultois

Committee in charge:

Professor Ram Seshadri, Chair
Professor Galen D. Stucky
Professor Peter C. Ford
Professor Carlos G. Levi

March 2015

The Dissertation of Michael W Gaultois is approved.

Professor Galen D. Stucky

Professor Peter C. Ford

Professor Carlos G. Levi

Professor Ram Seshadri, Committee Chair

March 2015

Design principles for oxide thermoelectric materials

by

Michael W Gaultois

Talent is cheap; dedication is expensive.

It will cost you your life.

– Bertoldo di Giovanni

Acknowledgements

To my teachers and mentors, who have been patiently guiding me to this point. Ram, Andrew, Arthur, I've learned so much from each of you about such different things. Ram, I couldn't hope to find a more supportive mentor to help me develop into a mature scientist. Being a scientist is more than a career, it's a way of life. You have helped me develop scientific aesthetic, and have shown me how to conduct myself in research, and collaborative endeavours. Everything is *interesting*, but I will continually strive to focus on what is *important*.

To the MeRL, which has been a warm and welcoming home, as well as a dynamic and exuberant research community to belong to. I have discovered what it means to be a part of a research *community*, and it has been my great pleasure and honor to work with such amazing people, at such an incredible institution. My thanks to colleagues, lab staff (Joe, Amanda), admin staff (Sylvia, Maureen, Joni, Maki, Sara, Marisol, Robin, Janet, Fuzzy, Joanne...and Jack), and outreach staff (Dotti, Julie, Mary, Claudia, Frank), for being great scientific citizens, and dear friends. Despite the sizeable bureaucracy in the background, it never got in the way of science. I never had to worry about any serious bureaucracy, and got to focus on research, supported by a great team. In addition to the thrill of research, my involvement with outreach has been so rewarding, and enabled by a community dedicated to creating these opportunities. My experience has been enriched by doing science fairs, mentoring international interns through the CISEI program, running workshops on campus, or giving presentations in the community. There is nothing to remind you that your work is exciting like having hundreds of kids screaming enthusiastically.

To the Chemistry Department staff (Mallarie, Ericka, Jane, Savanna, Kathy, Katie, Pat, Mira), for being so supportive, with particular thanks to Mallarie for guiding us along and making all our degree requirements feel like a straightforward checklist. To the machine shop boys (Bruce and Mike) and groupies (Richard and Cabe) for being so easy to work with when bringing my crazy ideas to fruition, and for being the department cheer squad. Between the jailhouse gang, to building an entire stern of a galleon for a that would not be out of place as a set piece in a production of Pirates of Penzance, your BBQs and parties are the stuff of legend.

To my thesis committee, Martin Moskovits, Galen Stucky, and Carlos Levi, who have been involved throughout my research and whose instrumentation has enabled the research presented here. A special thanks to Peter Ford, who kindly offered to serve on my committee in time of need, despite incredible inconvenience.

To Bryce and Greg at Citrine Informatics. We've only just begun, yet I'm excited to see what the future brings. You were my first collaboration from collaborative whitespace. I've thoroughly enjoyed working with you, and look forward to what comes next.

To the IRG-3 student and faculty members, with special thanks to Jason Douglas, Christina Birkel, Andrew Pebley, Leo Lamontagne, Mandi Buffon, and Anthony Rice for the great collaborative work we were able to perform together, and to Carlos Levi, Tresa Pollock, and Mike Gordon for your active involvement throughout my tenure at UCSB. Thanks also to Deryck Stave in the MPL, for help with maintenance and developing some of my crazy ideas. I haven't met anyone as resourceful, patient, experienced, helpful, and kind; you are inspiring.

To my colleagues and dear friends in the Seshadri family. My enthusiastic Love for you cannot be contained within these pages. Even as I begin to write names, so many thoughts of appreciation and fond memories rush through my mind, just as water gushes swiftly from a faucet when opened. It has been my sincere pleasure to spend time with you at a personal and professional level, and I hope we have many opportunities to work and play in the future. Your work is so exciting, your abilities so humbling, and your future so bright. Taylor, Jason, Moureen, Kristin, Anna, Jakoah, Jaye, Lauren, Kim, Christina, Alex, Leo, Mandi, Megan, Phil, Nate, and the new folks who are just starting: Doug, Clayton, Geneva, and Hayden. We are fortunate to be surrounded by many interns and exchange students. In particular, it's been a pleasure to work with Gregor and Roman, and I look forward to joining you guys across the pond.

To the previous generation of the Seshadri family, Josh Kurzmann, Daniel Shoemaker, Jamie Neilson, and Brent Melot. You guys started this whole journey when I met you at the GRC in 2010. Spending time with you at GRC convinced me that Ram's group was where I wanted to do my PhD. Thanks for being great ambassadors of Ram, and for introducing me to this exceptional family. It's been a delight to spend time with my older siblings at conferences and national labs, and I appreciate the mentorship of Eric Toberer, Efrain Rodriguez, and Kate Page.

To Phil Barton, Justin Poelma, Mike Brady, James Rogers, and Arthur Reading, who hosted me in their cliffside castle when I first visited UCSB. UCSB has been everything I ever dreamed of, and so much more. To the 6-pak +1 (Claude, Jason, Evgeny, Freeze, Carol, Mandi), to my foodies (Jack Zhang and Greg Su), to my lunch revolutionaries (Derka and Simpson), and to our strange band of misfits (Hoskins, Freeze, Gina, Evgeny, Santosh, Cynthia, Anna, and Claudia). Maybe, one day, we'll be able to go surfing and enjoy pie together.

To Anthony, Nate, and Andrey, it's been my pleasure sharing a living space with you, and feeding the masses pancakes; I'm happy that we could be friends in addition to room mates. Not everyone is lucky enough to have room mates actively trying to use Pavlovian conditioning to spend more time at home. Anthony, it's been my pleasure joining you on culinary adventures.

To Thomas Kaufmann, who ensures I leave the lab occasionally and experience the high life, whether it be flying to Mammoth for a weekend ski trip, sponsoring model searches, or walking down the red carpet with VIP passes at the opening gala of a film festival. It's been an incredible journey together over the past couple years, and it all began with a conversation on visit weekend about an alarm clock that reads your mind while you sleep.

To my family, and to my parents, who continue to amaze me. Life is a beautiful thing.

Curriculum Vitæ

Michael W Gaultois

Education

2015	Ph.D. in Chemistry, University of California, Santa Barbara, USA.
2012	M.Sc. in Chemistry, University of Saskatchewan, Saskatoon, Canada.
2010	B.Sc. in Chemistry, University of Alberta, Edmonton, Canada.

Publications from work at UCSB

14. Michael W. Gaultois, Taylor D. Sparks, Jason E. Douglas, and Ram Seshadri. Controlled microstructure and thermoelectric properties of reduced early transition metal oxide composites. (Prepared)
13. Michael W. Gaultois, Anton O. Oliynyk, Arthur Mar, Taylor D Sparks, Gregory J. Mulholland and Bryce Meredig. A Recommendation engine for suggesting unexpected thermoelectric chemistries, with experimental validation. (Submitted)
12. Kristin Denault, Jakoah Brgoch, Simon Kloss, Michael Gaultois, Joan Siewenie, Katharine Page, and Ram Seshadri. Average and local structure, Debye temperature, and structural rigidity in some oxide phosphor host compounds. (Submitted)
11. Michael W. Gaultois, Moureen C. Kemei, Jaye K. Harada and Ram Seshadri. Rapid preparation and magnetodielectric properties of trirutile Cr_2WO_6. *J. Appl. Phys.* 117:014105 (6pp), 2015. [**doi**]
10. Jakoah Brgoch, Michael W. Gaultois, Mahalingam Balasubramanian, Katharine Page, Byung-Chul Hong, and Ram Seshadri. Local structure and structural rigidity of the green-emitting β-SiAlON phosphor. *Appl. Phys. Lett.* 105:181904 (4pp), 2014. [**doi**]
9. Phillip T. Barton, Moureen C. Kemei, Michael W. Gaultois, Stephanie L. Moffitt, Lucy E. Darago, Brent Melot, Matthew R. Suchomel, and Ram Seshadri. Structural distortion below the Néel temperature in spinel $GeCo_2O_4$. *Phys. Rev. B* 90:064105 (7pp), 2014. [**doi**]
8. Gregor Kieslich, Ulrich Burkhardt, Igor Veremchuk, Christina S. Birkel, Jason E. Douglas, Michael W. Gaultois, Ingo Lieberwirth, Ram Seshadri, Galen D. Stucky, Yuri Grin, and Wolfgang Tremel. Enhanced thermoelectric properties of the n-type Magnéli phase $WO_{2.90}$: Reduced thermal conductivity through microstructure engineering. *J. Mater. Chem. A*, 2:13492–13497, 2014. [**doi**]
7. Adam J. Hauser, Jeremy M. Lucy, Michael W. Gaultois, Molly R. Ball, Jennifer R. Soliz, Yongseong Choi, Wolfgang Windl, Richard Rosenberg, John W. Freeland, Daniel Haskel, Patrick M. Woodward, and Fengyuan Yang. Magnetic structure in epitaxially strained Sr_2CrReO_6 thin films by element-specific XAS and XMCD. *Phys. Rev. B*, 89:180402 (6pp), 2014. [**doi**]

6. Kristin A. Denault, Jakoah Brgoch, Michael W. Gaultois, Alexander Mikhailovsky, Ralf Petry, Holger Winkler, Steven P. DenBaars, and Ram Seshadri. Consequences of optimal bond valence on structural rigidity and improved luminescence properties in $Sr_xBa_{2-x}SiO_4$:Eu^{2+} orthosilicate phosphors. *Chem. Mater.* 26:2275–2282, 2014. [**doi**]

5. Michael W. Gaultois and Taylor D. Sparks. How much improvement in thermoelectric performance can come from reducing thermal conductivity? *Appl. Phys. Lett.*, 104:113906 (4pp), 2014. [**doi**]

4. Gregor Kieslich, Christina Birkel, Jason E. Douglas, Michael W. Gaultois, Igor Veremchuk, Ram Seshadri, Galen D Stucky, Wolfgang Tremel. SPS-assisted preparation of the Magnéli phase $WO_{2.90}$ for thermoelectric applications. *J. Mater. Chem. A*, 1:13050–13054, 2013. [**doi**]

3. Moureen C. Kemei, Phillip T. Barton, Stephanie L. Moffitt, Michael W. Gaultois, Joshua A. Kurzman, Ram Seshadri, Matthew R. Suchomel, and Young-Il Kim. Crystal structures of spin-Jahn-Teller ordered $MgCr_2O_4$ and $ZnCr_2O_4$. *J. Phys. Condens. Matter*, 25:326001 (7pp), 2013. [**doi**]

2. Michael W. Gaultois, Taylor D. Sparks, Christopher K. H. Borg, Ram Seshadri, William D. Bonificio, and David R. Clarke. Data-driven review of thermoelectric materials: Performance and resource considerations. *Chem. Mater.*, 25:2911–2920, 2013. [**doi**]

1. Michael W. Gaultois, Phillip T. Barton, Christina S. Birkel, Lauren M. Misch, Efrain E. Rodriguez, Galen D. Stucky, and Ram Seshadri. Structural disorder, magnetism, and electrical and thermoelectric properties of pyrochlore $Nd_2Ru_2O_7$ *J. Phys. Condens. Matter*, 25:186004 (10pp), 2013. [**doi**]

Abstract

Design principles for oxide thermoelectric materials

by

Michael W Gaultois

Over 60% of the energy in the United States is wasted, most of it as heat. This amounts to staggering losses of natural and economic resources, and although some of this heat is Carnot heat that is unavoidable, even recovering a small fraction of the remaining waste heat would lead to economic and environmental benefits. Thermoelectric materials are a class of materials that can generate power from heat, but their widespread deployment has been limited because thermoelectric materials are currently inefficient, made from rare elements, and decompose at high temperatures when operated in air. Researchers have sought to develop oxide thermoelectric materials to overcome these shortfalls, but development of oxide materials is still relatively new, and has lacked guiding principles that have led to significant advances in traditional thermoelectric materials.

The work presented here outlines the development of design principles for oxide thermoelectric materials, which until this point were not clear. Initial work targeted a Ru pyrochlore system with tunable electrical resistivity, with the goal of finding the optimal zone for electrical performance. This initial work revealed traditional design criteria are not helpful for guiding research of most oxide thermoelectric materials, and new strategies were developed to determine the parameter space of interest for oxide thermoelectrics. Building on this work, a database was created with thermoelectric materials data extracted from over 100 publications (`www.mrl.ucsb.edu:8080/datamine/thermoelectric.jsp`), and a visualization framework was built to quickly survey performance and resource considerations and define a parameter space for good thermoelectric performance. Most im-

portantly, all systems with high performance exhibit metallic electrical transport, with electrical resistivity below the Mott maximum resistivity ($\rho < 10^{-2}\,\Omega\,\mathrm{cm}$). Further, although normally in this regime one would expect a negligible Seebeck coefficient, all high performance materials exhibit anomalously high Seebeck coefficients ($|S| > 100\,\mu\mathrm{V/K}$) given the low electrical resistivity. This work focused on tools for discovery of new materials, though was expanded upon by developing screening methods to look at which existing systems can be optimized and improved, and which are already nearing their maximum possible performance using currently available methods in the field.

The requisite metallic electrical transport considerably restricts the parameter space of oxides, and this knowledge was used to target reduced early transition metal oxides with highly connected crystal structures. Owing to the high structural connectivity in three dimensions and the intrinsic crystallographic defects that lead to low thermal conductivity, a series of WO_3–Nb_2O_5 materials was rapidly prepared using spark plasma sintering (SPS). The resulting materials are composites with embedded W-rich precipitates that are stable to repeated thermal cycling. These composites exhibit good thermoelectric properties; the best-performing composition studied displays a thermoelectric figure of merit $zT = 0.1$ at 950 K, the highest temperature measured, and zT increases at higher temperatures not accessible using our instrumentation. Even without optimization these materials display superior performance to most n-type oxides that have been actively researched, and are a promising platform for future research.

WO_3–Nb_2O_5 was prepared in a single step under 30 minutes of processing using SPS, but owing to the presence of multiple observed phases and precipitates, a study was undertaken to ensure W cation mobility is sufficient to allow diffusion and pseudo-equilibration under the rapid SPS processing conditions. Cr^{3+} is a notoriously inert cation due to crystal field energy stabilization, so the SPS reaction of Cr_2O_3 and WO_3 binary oxides was investigated under similar processing conditions. Remarkably, >99 mol% purity Cr_2WO_6

can be formed from SPS reaction of oxide precursors in as little as 3 min at 1473 K, which we attribute to the reducing conditions present during SPS processing. The reducing conditions during SPS lead to rapid diffusion of cations and anions from partial reduction of inert Cr^{3+} species to labile Cr^{2+} species, as well as oxygen ion mobility due to vacancy formation that accompanies partial reduction of W^{6+}.

Following the successful use of human-based "small data" mining, machine learning algorithms developed in this work were trained on our thermoelectrics database to create software capable of predicting broad changes in thermoelectric properties. This recommendation engine can suggest chemical compositions likely to exhibit good thermoelectric performance, and has successfully identified a new class of thermoelectric materials that is compositionally distant from previously reported thermoelectric materials. Given the difficulty and slow pace with which new material discovery has traditionally occurred, computer-aided materials discovery may provide the ability to systematically explore chemical whitespace and increase the rate of material discovery and technological progress.

Contents

Chapter 1

Introduction

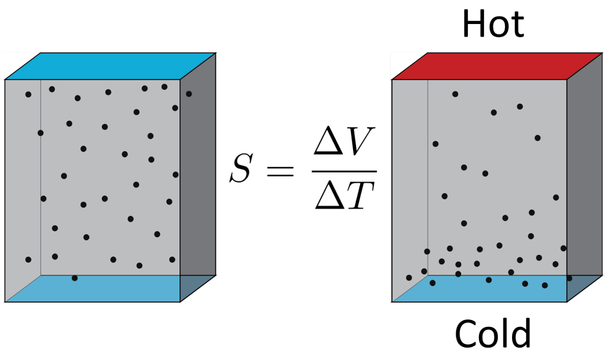

Figure 1.1: When a temperature gradient is maintained across a thermoelectric material, a corresponding electric potential is established, and can be used to do external work. This phenomenon is known as the Seebeck effect, which is typically on the order of ∼100 V/K for typical thermoelectric materials. To maintain equal chemical potential, the hot side of a thermoelectric materials has fewer, higher-energy carriers compared to the cold side.

1.1 Thermoelectric materials as solid-state heat engines

Thermoelectric materials are a class of materials that generate electricity when they are heated unevenly. Specifically, when a temperature gradient is maintained across a thermoelectric material, a corresponding electric potential is established, and can be used to do external work. This phenomenon is known as the Seebeck effect, which is typically on the order of ∼100 V/K for typical thermoelectric materials. The Seebeck effect occurs because carriers will seek a state with minimum chemical potential energy. Consequently, excited carriers at the hot side of a thermoelectric material have higher chemical potential energy and will diffuse to the cold side. If there is an asymmetry in the type of carriers that can diffuse (*i.e.*, holes compared to electrons), an electrical potential develops that can drive an electrical current (Figure 1.1).

The Seebeck voltage is an intrinsic material property, and in order to generate useful voltages, a thermoelectric generator will typically consist of many thermoelectric elements connected in an electrical series. Unlike other heat engines, thermoelectric materials have no moving parts, and devices can be easily scaled to arbitrary dimensions to suit the desired application. This makes thermoelectric generators ideal for applications where light weight, small form factors, and reliability are key.

$$zT = \frac{S}{\rho\kappa}T \tag{1.1}$$

Despite having been initially discovered in 1821, the conversion efficiency of thermoelectric materials is poor, so thermoelectric materials remain viable only in niche applications where other heat engines are unsuitable. The performance of a thermoelectric material is given by zT (Equation 1.1), a dimensionless figure of merit influenced by the Seebeck coefficient S, the electrical resistivity ρ, the thermal conductivity κ, and the absolute temperature T. For perspective, current high-performance materials have zT >1 [1, 2], the best bulk materials made to date have zT ∼2 [3, 4], and widespread deployment outside niche applications will require zT >3. Increasing the thermoelectric performance is difficult because the underlying electrical and thermal transport properties are correlated and cannot be tuned independently. For example, the electrical resistivity and thermal conductivity are intrinsically linked by the Wiedemann-Franz law [5], which is why good electrical conductors tend to also be good thermal conductors (*e.g.,* copper). Further, both the electrical resistivity and the Seebeck coefficient depend on the concentration of electrical carriers, so decreasing the electrical resistivity (good) also decreases the Seebeck coefficient (bad). Although materials with low electrical resistivity are desirable for high thermoelectric performance, they tend to have negligible Seebeck coefficients and high thermal conductivity, resulting in an overall low zT and poor performance.

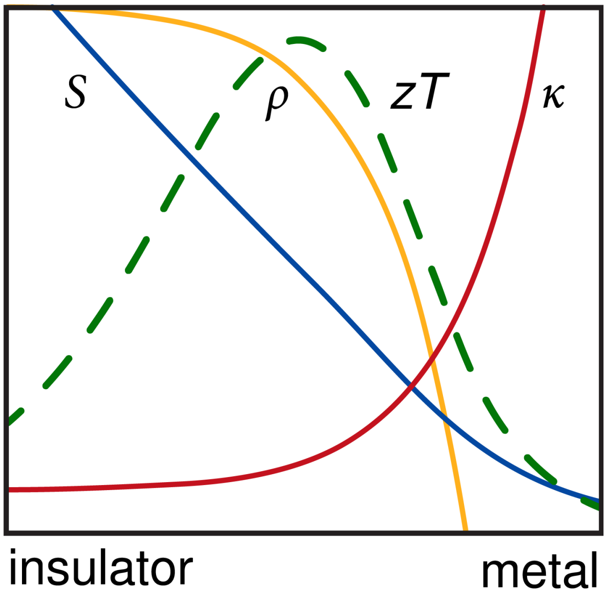

Figure 1.2: In most intermetallic and semiconductor thermoelectrics, carrier doping is performed to optimize the zT of materials, where the maximum zT occurs at a point of ideal compromise between high S, low ρ, and low κ. There are many factors that complicate this process in oxide materials, and it is often not obvious where the zone of maximum performance lies. Figure adapted from [6].

1.2 Optimizing electrical transport

In most intermetallic and semiconductor thermoelectrics, carrier doping is performed to optimize the zT of materials, where the maximum zT occurs at a point of ideal compromise between S, ρ, and κ (Figure 1.2). However, the doping behaviour of bulk oxides is often much less controlled. In many cases, introducing additional elements in the form of dopants will stabilize new phases instead of electronically doping the primary phase. Additionally, dopants tend to alter the crystal structure, which changes the band structure and has effects far more dramatic than a change in the carrier concentration alone. For these reasons, it is unclear where the ideal parameter space lies for oxides, and this has been clearly determined in this work.

The first step towards understanding the optimal zone of electrical transport began by examining a system of rare-earth Ru pyrochlores ($A_2Ru_2O_7$; $A = $ Pr, …, Lu, Y, Bi), an

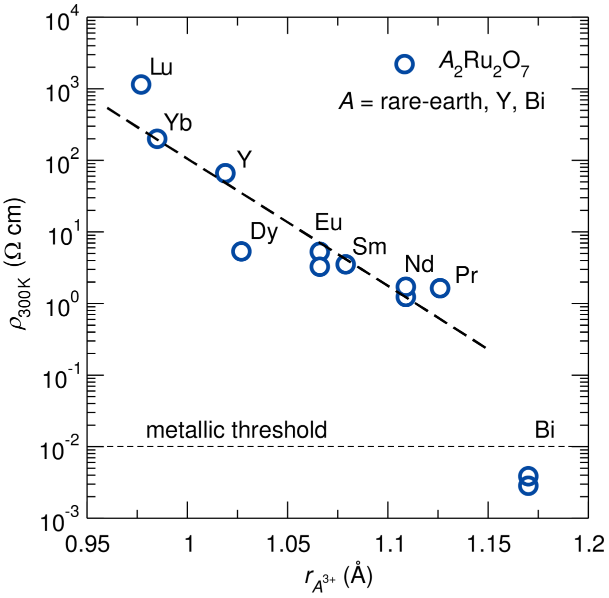

Figure 1.3: Room-temperature electrical resistivity of $A_2Ru_2O_7$ ($A = $ Pr, ..., Lu, Y, Bi) decreases smoothly with increasing average A^{3+} cation radius. The thin dashed line at $\rho = 0.01\,\Omega\,\mathrm{cm}$ represents the Mott minimum metallic conductivity at room temperature. Ionic radii of 8-coordinate 3+ cations were taken from Shannon [7]. Values of electrical resistivity were taken from references [8, 9, 10, 11, 12, 13, 14, 15].

oxide system deliberately chosen for the tunability of electrical resistivity near a metal-insulator transition (MIT) (Figure 1.3). In these materials, electrical conduction occurs through the Ru–O–Ru framework via Ru 4d – O 2p states, and the degree of orbital overlap is influenced by the size of the rare-earth ions. Increasing the ionic radius of the rare-earth ion increases the Ru–O–Ru bond angle, flattening out the bond and increasing orbital overlap, which increases bandwidth and decreases the electrical resistivity [16]. This allows the preparation of materials with arbitrary electrical resistivity; we present the study of $Nd_2Ru_2O_7$, chosen for our belief that the insulating nature of the material would lead to a high Seebeck coefficient while proximity to a MIT would lead to sufficiently low electrical resistivity to result in good thermoelectric performance.

1.3 Structure and electrical conductivity in oxides

Oxides can assume a wide range of possible electrical resistivities, with electrical transport ranging from metallic (*e.g.*, RuO_2 or ReO_3) to insulating (*e.g.*, TiO_2 or SiO_2). There are many factors associated with this gamut of properties, and the crystal structure, which dictates the arrangement of atoms in three dimensions, is one of the central determinants. Convincing evidence can be seen by examining systematic changes in crystal structure within a compositional series. For example, in the perovskite $Ln\mathrm{NiO_3}$ ($Ln = \mathrm{La}, \ldots, \mathrm{Lu}, \mathrm{Y}$) compositional series, it has been shown that the Ni–O–Ni bond angle determines whether the compound displays metallic or insulating electrical transport [17, 18]. When the lanthanide cation is large, the Ni–O–Ni bond angle is close to 180° and allows good Ni 3d – O 2p orbital overlap, which leads to large bandwidth and metallic electrical transport. As the size of the lanthanide cation decreases, the Ni–O–Ni bond angle shrinks, and the poor orbital overlap leads to low electronic bandwidth and insulating electrical transport. For this reason, $LaNiO_3$ is metallic at all temperatures, whereas all other lanthanide members are insulating at low temperatures and undergo an insulator-to-metal transition that increases in temperature with decreasing lanthanide ionic radius [17, 18]. At the other extreme, $LuNiO_3$ remains insulating up to 600 K.

High atomic connectivity within a crystal structure is also very important to ensuring metallic electrical transport. This can clearly be seen by examining the change in electrical properties with changing dimensionality within the $La_{n+1}Ni_nO_{3n+1}$ ($n = 1, 2, 3, \ldots, \infty$) homologous series from La_2NiO_4 ($n = 1$) to $LaNiO_3$ ($n = \infty$) [19]. This is analogous to the Ruddlesden-Popper homologous series (Figure 1.4) [20]; n dictates the number of contiguous $LaNiO_3$ layers (NiO_6) octahedra), and larger values of n correspond to more highly connected structures. In this series, $n = 1$ corresponds to isolated 2-dimensional $LaNiO_3$ sheets, and $n = \infty$ corresponds to an infinite 3-dimensional network of $LaNiO_3$.

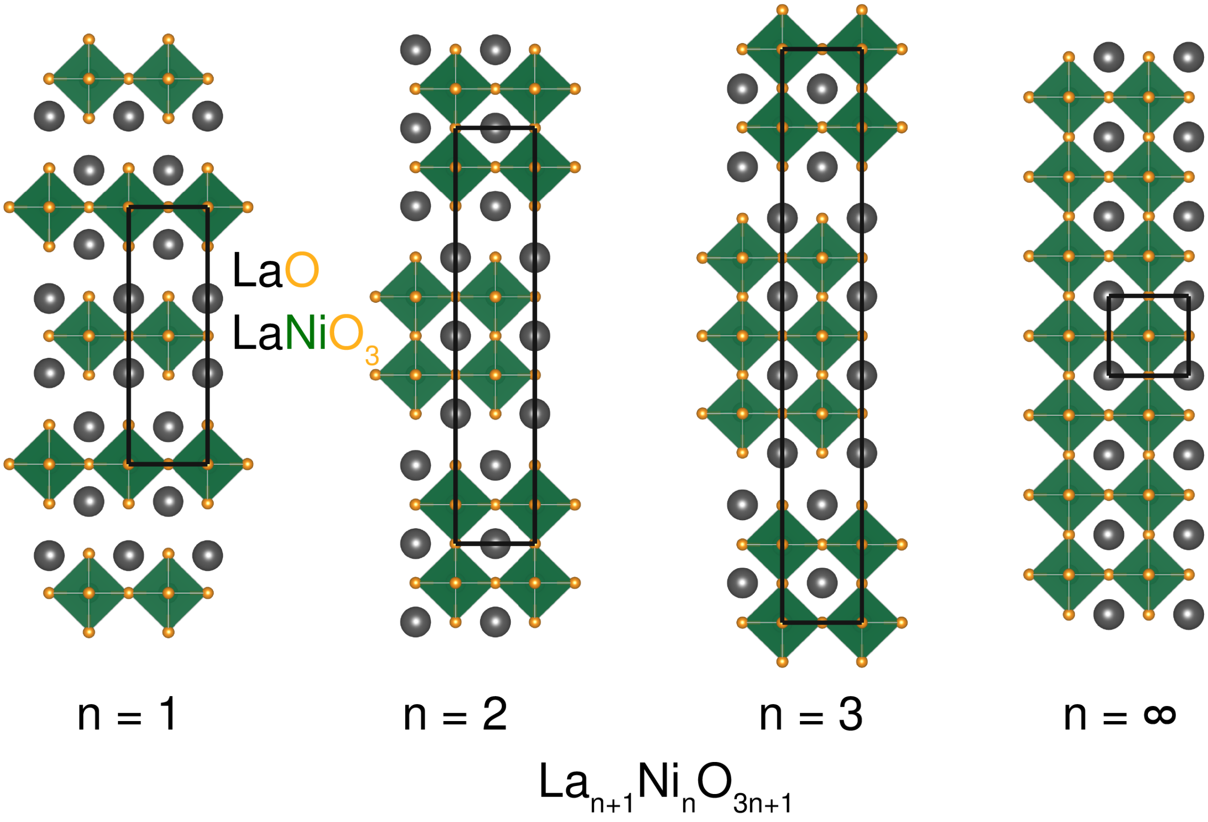

Figure 1.4: A simplified representation of the structural evolution within the $La_{n+1}Ni_nO_{3n+1}$ ($n = 1,\ 2,\ 3,\ \ldots,\ \infty$) homologous series from La_2NiO_4 ($n = 1$) to $LaNiO_3$ ($n = \infty$). n dictates the number of contiguous $LaNiO_3$ layers (NiO_6) octahedra) separated by an LaO layer, and larger values of n correspond to more highly connected structures. In this series, $n = 1$ corresponds to isolated 2-dimensional $LaNiO_3$ sheets, and $n = \infty$ corresponds to an infinite 3-dimensional network of $LaNiO_3$. The unit cell is shown in black.

At the extreme of low dimensionality within this series (La_2NiO_4; $n = 1$) there are alternating planes of $LaNiO_3$ and LaO layers stacked along the c axis of the unit cell. This pseudo-2D material is insulating at all temperatures. In the next member ($La_3Ni_2O_7$; $n = 2$), there are blocks of two layers of $LaNiO_3$ interleaved with one LaO layer, and an insulator-to-metal transition is seen below 300 K, though the exact point depends on oxygen stoichiometry. By the next member ($La_4Ni_3O_1$9; $n = 3$), the sample is metallic, as is the end-member $LaNiO_3$, which has infinite blocks of NiO_6 octahedra connected in 3 dimensions. As nicely highlighted by Mohan Ram *et al.* [19], highly connected structures result in good electrical transport, whereas low connectivity localizes carriers and leads to poor electrical transport.

1.4 Reducing thermal conductivity

Optimizing the electrical properties of thermoelectric materials has been difficult because of the many competing effects, and this is to say nothing of the thermal conductivity. As highlighted in the previous discussion, low electrical resistivity in oxides requires a highly connected crystal structure. Unfortunately, the same features that promote low electrical resistivity also generally lead to high thermal conductivity, which is unfavorable for thermoelectric materials. The inevitable question becomes how to achieve the high structural connectivity required for metallic electrical transport while maintaining a low thermal conductivity.

The total thermal conductivity results from contributions from both electronic and lattice components ($\kappa = \kappa_e + \kappa_l$). Electronic carriers can be either holes and/or electrons, which carry heat in addition to charge. As scattering electronic carriers directly increases the electrical resistivity, this contribution to thermal conductivity is somewhat intractable to reduce in thermoelectrics where a low electrical resistivity is desired. However, the lattice component of thermal conductivity is largely independent of electrical resistivity. The active carriers involved in the lattice component of thermal conductivity are phonons, which are waves with a broad distribution of wavelengths (from nm to μm) that result from the concerted oscillations of atoms in a solid. These waves propagating through a material carry heat, and can be scattered by features with similar characteristic lengthscales.

Crystal structure engineering can be undertaken to reduce the thermal conductivity through the deliberate introduction of defects designed to scatter phonons [21]. These defects can take the form of crystallographic site defects (substitution of atoms or oxygen vacancies), or crystallographic shear, which involves the extended condensation of a polyhedral network and introduces variation in the long-range crystal structure to scatter phonons. These shear planes can be easily formed in early transition metal oxides (*e.g.*, TiO_x, VO_x, NbO_x, TaO_x, MoO_x, WO_x, etc.) [22], a family of materials that often have highly connected crystal structures and can often be partially reduced to improve the electrical transport.

Not all crystal structures lend themselves easily to crystal engineering, so many recent gains in performance have been made by moving away from single-phase materials towards biphasic materials. Microstructure engineering can be performed to create features at lengthscales ranging from nm to $/mu$m, which is well paired to the phonon distribution of most materials. Secondary-phase inclusions within a primary-phase matrix have been shown to reduce the material thermal conductivity by scattering phonons with wavelengths similar to the dimensions of the secondary phase inclusions [23]. Because the mean free path lengths of phonons are much longer than electrons, the secondary phase inclusions preferentially scatter phonons without dramatically increasing the rate of electron scattering. This phenomenon leads to composites with reduced thermal conductivity without adversely increasing the electrical resistivity, and is used in this work explicitly for this beneficial purpose.

The ability to independently reduce thermal conductivity and improve thermoelectric performance has led to widespread microstructure engineering in known thermoelectric materials [2, 24], and has resulted in record-breaking thermoelectric materials with zT values above 2 [4]. It is obvious that lower thermal conductivity will increase the performance of a material, but it remains unclear to what extent this can be done, particularly for materials that have already undergone extensive microstructural engineering. Accordingly, we have employed a simple mathematical derivation and developed visualization tools and screening methods to visualize the performance gains possible by reducing the thermal conductivity in existing thermoelectric materials. Combined with the large thermoelectrics database described in this work, these tools allow researchers to quickly identify which materials are nearly optimized and which materials have room for improvement and deserve further study.

1.5 Using large datasets to gain insight

Breaking out of the common composition space to discover new chemistries is a difficult challenge in all materials disciplines, and even then it involves considerable luck and extensive study to produce viable materials, as has been observed in the recent renaissance of perovskite solar cells [25]. Many of the most notable materials classes under investigation today—from $\mathrm{Na}_x\mathrm{CoO}_2$ derived thermoelectrics [26] to iron arsenide superconductors [27]—were discovered fortuitously. As a result, experimental efforts often gravitate toward incrementally improving *known* chemistries (via chemical substitution, doping, microstructure engineering, etc.), as these efforts are more likely to bear fruit than high-risk searches through chemical whitespace for entirely new materials.

Moreover, principles and beliefs about what constitute potentially interesting materials are based only on the existing paradigm, which may be irrelevant for other classes of materials. For example, research in developing superconductors with higher critical temperatures was based informally on several empirically-derived principles—the Matthias rules of superconductivity, for example, suggested that magnetism and superconductivity were mutually exclusive. These rules turned out to directly oppose many of the features present in the later-discovered cuprates, and then again with pnictides, both of which surpassed traditional BCS superconductors in terms of critical temperatures. In similar ways, the experimental search for new thermoelectric materials remains largely confined to a limited set of successful chemical and structural families, such as chalcogenides, skutterudites, and Zintl phases [28, 6, 29]. Given the heavy focus on traditional, intermetallic thermoelectrics, the development of new high-performance oxide materials may require different design principles, and it is important to look broadly at the wealth of data available in the literature in a comprehensive manner without bias.

1.5.1 "Small data" mining through visualization

To assemble as much information in order to ascertain the parameter space of interest for oxide thermoelectric materials, we extracted data from over 100 reports of thermoelectric materials across 11 material families, and created a database with over 1 000 datapoints and 30 000 pieces of metadata using a set of relevant material parameters and properties at several key temperatures of interest. We also created a web-based interactive visualization framework to explore the data, as visualization strategies become difficult with larger datasets (`www.mrl.ucsb.edu:8080/datamine/thermoelectric.jsp`). To maximize the dimensionality and information content, the scatter plots we employ provide a third dimension of marker size, which indicates a performance metric, and a fourth dimension of marker colour, which indicates the family of related materials (Fig-

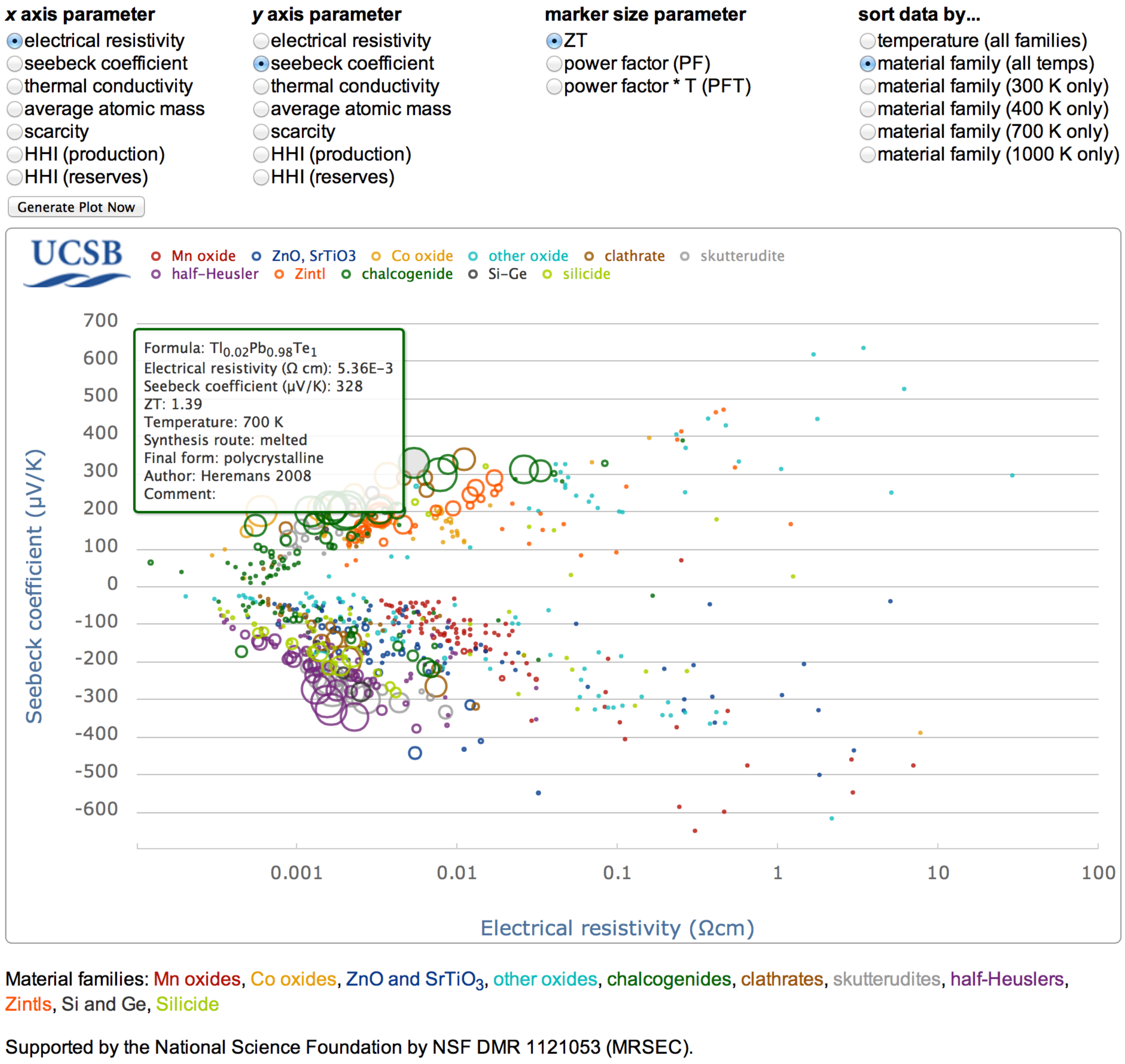

***x* axis parameter**
- ● electrical resistivity
- ○ seebeck coefficient
- ○ thermal conductivity
- ○ average atomic mass
- ○ scarcity
- ○ HHI (production)
- ○ HHI (reserves)

***y* axis parameter**
- ○ electrical resistivity
- ● seebeck coefficient
- ○ thermal conductivity
- ○ average atomic mass
- ○ scarcity
- ○ HHI (production)
- ○ HHI (reserves)

marker size parameter
- ● ZT
- ○ power factor (PF)
- ○ power factor * T (PFT)

sort data by...
- ○ temperature (all families)
- ● material family (all temps)
- ○ material family (300 K only)
- ○ material family (400 K only)
- ○ material family (700 K only)
- ○ material family (1000 K only)

Formula: $Tl_{0.02}Pb_{0.98}Te_1$
Electrical resistivity (Ω cm): 5.36E–3
Seebeck coefficient (μV/K): 328
ZT: 1.39
Temperature: 700 K
Synthesis route: melted
Final form: polycrystalline
Author: Heremans 2008
Comment:

Material families: Mn oxides, Co oxides, ZnO and $SrTiO_3$, other oxides, chalcogenides, clathrates, skutterudites, half-Heuslers, Zintls, Si and Ge, Silicide

Supported by the National Science Foundation by NSF DMR 1121053 (MRSEC).

Figure 1.5: Screenshot of the web-based visualization tool (`www.mrl.ucsb.edu:8080/datamine/thermoelectric.jsp`), that permits the simultaneous visualization of four parameters: abscissa, ordinate, marker size and color. Several variables can be chosen as abscissa and ordinate, and measures of thermoelectric performance can be represented by the radius of the data points. To simplify navigation, families of related materials can be displayed or hidden by clicking their legend marker. Further, hovering over a data point intuitively reveals a tooltip with pertinent information: the names and values for the abscissa and ordinate, the chemical composition, the sample form (*e.g.*, polycrystalline, single crystal, nanoparticles), the preparatory route (*e.g.*, ceramic method, arc melting), the author and year, and either the power factor, κzT, or zT value. Clicking on a data point leads the web-browser directly to the source publication *via* the document object identifier (DOI).

ure 1.5). Through these endeavours, we have incorporated both performance and resource considerations to create a set of tools for researchers and have outlined design criteria and a parameter space of interest to guide the discovery of new thermoelectric materials with favorable performance.

It is obvious why considering the material performance is important to the development of thermoelectric materials, but it is also important to be concerned about resource considerations, which we also present. Although materials with the highest performance will always be desired, widespread deployment may be limited in some applications by intense material use. Further, heavy reliance on a single supplier can lead to significant risk to manufacturers and larger industries, and must be considered if intense deployment is expected. The resource considerations we present here will depend on the scale of deployment and intensity of resource use, and we explicitly deal with the crustal abundance and geopolitical distribution of primary resources.

1.5.2 "Big data" mining with machine learning

Visually interpreting large amounts of data will always be limited by the human component, and lacks the high dimensionality to observe underlying correlation that may exist in complex datasets. The visual plots discussed earlier attempt to maintain as much information by providing a third dimension of marker size and a fourth dimension of colour, but even this has its limits. "Big data" strategies involving machine learning benefit from the ability to exploit large, multidimensional, and complex datasets, and are useful to develop more complicated and less evident approaches for new material discovery. Due to the complicated nature of the underlying physics, these correlation-driven approaches may yield new insight into our understanding of what leads to high thermoelectric performance. Principal component analysis (PCA) is one way to examine large datasets and examine correlation, but this primarily concerns dimensionality reduction and collapsing the data onto a set of axes that maximizes the spread within the data. Machine learning algorithms, on the other hand, are not constrained to any functional forms, and are thus a highly nonlinear regression able to regress all input variables to model a target variable, such as a physical property or thermoelectric performance.

Machine learning algorithms are popular datamining tools, but require large training sets to be effective. These training datasets require examples of materials with good performance, but also materials with poor performance. This poses an existential problem for materials science, as literature reports of functional materials are biased towards materials that perform well. Nevertheless, the machine learning algorithms were trained on the thermoelectrics database created here, and used to create a model that predicts physical properties that constitute zT ($zT = S\rho^{-1}\kappa^{-1}T$). The resulting material recommendation engine can suggest chemical compositions likely to exhibit good thermoelectric performance. This recommendation engine has successfully helped discover a new class of thermoelectric materials from chemical whitespace, and the new materials exhibit surprising thermoelectric performance given the metal composition (Ln_{12}Co$_5$Bi, $Ln =$ Gd, Er).

1.6 Using spark plasma sintering to rapidly explore new material systems

Materials discovery involves the identification of potential chemical compositions, but also the preparation of new materials. Spark plasma sintering (SPS) offers a rapid preparatory route to react and consolidate material in a single processing step, which provides a quick method to prepare dense samples suitable for measurement of physical

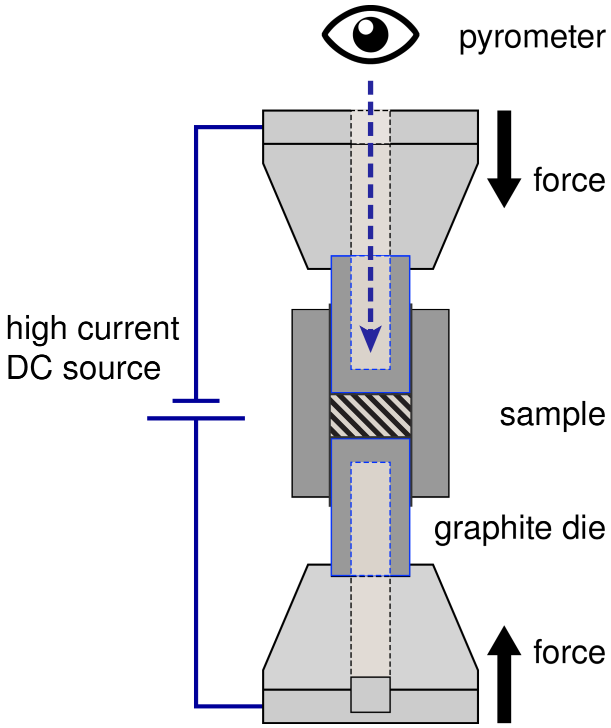

Figure 1.6: Spark plasma sintering (SPS) offers a rapid preparatory route to react and consolidate material in a single processing step, and provides a quick route to prepare dense samples suitable for measurement of physical properties. A typical instrument will have a vacuum chamber inside which a die set can be mounted and subjected to a mechanical load and electrical current.

properties. This is ideal for quickly preparing and characterizing many new compositions to explore the phase space of possible thermoelectric materials.

The name initially came from early investigations where sparks and plasma were believed to be central to the rapid densification rates, though these phenomena have since been disproven. Nevertheless, while the colloquial name of "SPS" remains, the technique is more accurately described as current-assisted, pressure-activated densification (CAPAD) [30]. A typical instrument will have a vacuum chamber inside which a die set can be mounted and subjected to a mechanical load and electrical current (Figure 1.6). During a typical process, the sample will be rapidly heated by Joule heating of the conductive die set while under an applied load, and temperature is increased until densification is

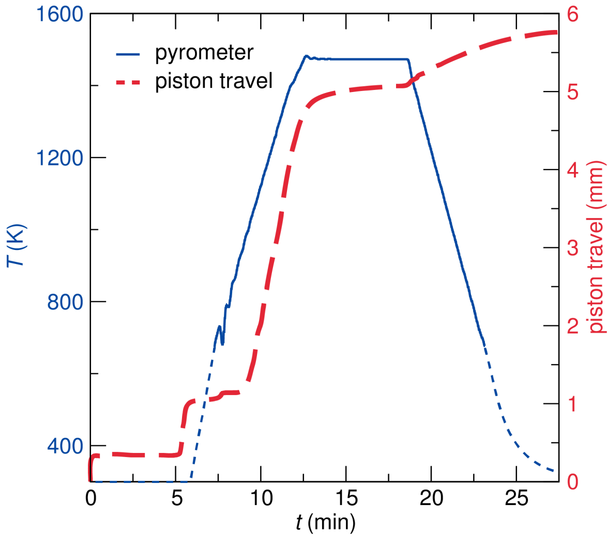

Figure 1.7: SPS processing allows rapid heating and cooling at rates greater than 200 K/min. Further, full densification takes only minutes, compared to hours required by traditional hot pressing. For typical processes near 1500 K, a potential of 5 V and a current of 1000 A are used. The applied mechanical force is generally limited by the integrity of the die set, with pressures up to ∼80 MPa available for graphite die sets.

observed; the whole heating, densification, and cooling process takes less than 30 minutes (Figure 1.7). For typical processes near 1500 K, a potential of 5 V and a current of 1000 A are used. The applied mechanical force is generally limited by the integrity of the die set, with pressures up to ∼80 MPa available for graphite die sets.

In addition to densification, SPS can also prepare phase-pure materials from precursors. The preparation of phase-pure single-cation $WO_{3-\delta}$ phases from WO_3 and W metal has been previously demonstrated citeKieslich2013JMCA, and the preparation of multi-cation WO_3-containing phases are demonstrated in this work. For example, we show in this work that Cr_2WO_6 can be made from WO_3 and Cr_2O_3 powders using SPS at 1473 K for less than 10 min, proving that anion and cation mobility is sufficient to allow diffusion and phase equilibrium in WO_3 systems at these reaction temperatures and timescales. SPS processing generally results in specimens with >95% single-crystal density, which is critical to accurate determination of some physical properties, such as thermal diffusivity. Accordingly, many samples of different compositions can be made in relatively short periods, and can be subjected to physical property measurements with minimal post-processing. In the studies presented here, the entire cylindrical pellet is used for thermal diffusivity measurements, and the cylindrical pellet can be sectioned to provide rectangular prism specimens for electrical property measurement (electrical resistivity and Seebeck coefficient).

The rapid processing times and simultaneous reaction and consolidation during SPS overcome many of the common pitfalls of traditional ceramic sample preparation methods and traditional hot pressing. Traditional solid-state preparation of materials requires extended heat treatments at high temperatures. This is time consuming, but it also is problematic when working with volatile precursors, such as early transition metal oxides of Mo or W [31], or late transition metal oxides of Ru or Ir [32]. In these cases, special measures must be taken, such as the addition of excess reagent and the use of sealed crucibles. Further, the final product after reaction is a powder that must be consolidated and densified before physical property measurements can be performed. This leads to further problems, as traditional hot pressing requires sustained high temperatures for several hours, and these high temperatures and long duration under low oxygen partial pressures often result in decomposition (either through instability or volatility) of the oxide materials.

1.7 Overview and impact

The work presented here outlines the development of design principles for the discovery of high-performance oxide thermoelectric materials, which until this point were not clear. Initial work targeted a Ru pyrochlore system with tunable electrical resistivity, with the goal of finding the optimal zone for electrical performance. This revealed traditional design criteria are not applicable to most oxide systems, and new strategies based on collecting and examining large datasets were developed to determine the parameter space of interest for oxide thermoelectrics. Most importantly, all systems with high performance exhibit metallic electrical transport, with electrical resistivity below the Mott maximum resistivity ($\rho < 10^{-2}\,\Omega\,\mathrm{cm}$). Further, although normally in this regime one would expect a negligible Seebeck coefficient, all high performance materials exhibit anomalously high Seebeck coefficients ($|S| > 100\,\mu\mathrm{V/\,K}$) given the low electrical resistivity.

This large dataset and new knowledge was used to discover new thermoelectric materials. Specifically, we began by deliberately targeting WO_3–Nb_2O_5 phases, a series of early transition metal oxides with highly connected crystal structures. To explore the large phase space, we demonstrated spark plasma sintering (SPS) is well-suited for the rapid preparation of complex WO_3-containing phases at 1473 K, and prepared a compositional series of dense specimens with metallic electrical transport. The resulting materials are composites with embedded W-rich precipitates that are stable to repeated thermal cycling, and exhibit superior thermoelectric performance to most n-type oxides that have been actively researched. In addition to the demonstrated success of the guiding principles for oxide thermoelectrics developed here, we have used machine learning algorithms to create a materials recommendation engine, and have successfully discovered new thermoelectric materials in chemical whitespace that exhibit surprising performance. Given the difficulty and slow pace with which new material discovery has traditionally occurred as well as the promise of computer-aided materials discovery demonstrated here, it will be important to assess to what extent these tools can be generalized to other disciplines. Towards this end, the thermoelectrics database, visualization tools, and the recommendation engine are all freely available online for use by the larger research community.

Chapter 2

Structural disorder, magnetism, and electrical and thermoelectric properties of pyrochlore $Nd_2Ru_2O_7$

---

[1] A version of this chapter has been published, and is reproduced with permission from: Michael W. Gaultois, Phillip T. Barton, Christina S. Birkel, Lauren M. Misch, Efrain E. Rodriguez, Galen D. Stucky, and Ram Seshadri. *J. Phys. Condens. Matter*, 25:186004 (10pp), 2013. [**doi**] © 2013, IOP Publishing Ltd.

Polycrystalline $Nd_2Ru_2O_7$ samples have been prepared and examined using a combination of structural, magnetic, and electrical and thermal transport studies. Analysis of synchrotron X-ray and neutron diffraction patterns suggests some site disorder on the A-site in the pyrochlore sublattice: Ru substitutes on the Nd-site up to 7.0(3)%, regardless of the different preparative conditions explored. Intrinsic magnetic and electrical transport properties have been measured. Ru 4d spins order antiferromagnetically at 143 K as seen both in susceptibility and specific heat, and there is a corresponding change in the electrical resistivity. The onset of a second antiferromagnetic ordering transition seen below 5 K is attributed to ordering of Nd 4f spins. $Nd_2Ru_2O_7$ is an electrical insulator, and this behaviour is believed to be independent of the Ru-antisite disorder on the Nd site. The electrical properties of $Nd_2Ru_2O_7$ are presented in the light of data published on all $A_2Ru_2O_7$ pyrochlores, and we emphasize the special structural role that Bi^{3+} ions on the A-site play in driving metallic behaviour. High-temperature thermoelectric properties have also been measured. When considered in the context of known thermoelectric materials with useful figures-of-merit, it is clear that $Nd_2Ru_2O_7$ has excessively high electrical resistivity which prevents it from being an effective thermoelectric. A method for screening candidate thermoelectrics is suggested.

2.1 Introduction

The $A_2B_2O_6O'$ pyrochlore structure, shown in Figure 2.1, comprises two interpenetrating B_2O_6 and A_2O' sublattices [8]. The electrical properties of pyrochlore ruthenium oxides ($A_2Ru_2O_7$, $A=$ Pr through Lu, Y, and Bi) are of long-standing interest. In $A_2Ru_2O_7$ ruthenates, electrical conductivity is expected to take place through the network of corner-sharing RuO_6 octahedra (*i.e.*, the B_2O_6 sublattice). While all the rare-earth members are insulating, $Bi_2Ru_2O_7$ is metallic. Several investigators have sought to

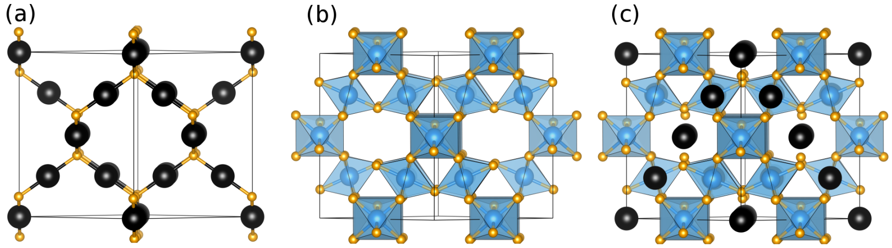

Figure 2.1: Interpenetrating a (a) "cubic-ice" diamondoid A_2O′ lattice with (b) a lattice of corner-connected BO$_6$ octahedra gives the (c) A_2B_2O$_6$O′ pyrochlore structure of $Nd_2Ru_2O_7$. Space group $Fd\bar{3}m$ [No. 227, A at $(\frac{1}{2}, \frac{1}{2}, \frac{1}{2})$, B at $(0, 0, 0)$, O at $(x_O, \frac{1}{8}, \frac{1}{8})$, and O′ at $(\frac{3}{8}, \frac{3}{8}, \frac{3}{8})$]. Black spheres are Nd, blue octahedra surround Ru, and the orange spheres are O.

explain the difference in conductivity by examining changes in Ru–O–Ru bond angle — determined by the combination of Ru–O bond length and the size of A — and consequent changes in orbital overlap and bandwidth [16, 9]. Electron spectroscopic investigations of $Y_2Ru_2O_7$ compared with $Bi_2Ru_2O_7$ led Cox *et al.*[33] to conclude that the principle difference seen is the participation in conduction of Bi 6s states in $Bi_2Ru_2O_7$. This participation broadens the Ru 4d band width sufficiently that a metallic ground state is preferred over one that is correlated and insulating. However,Shoemaker *et al.*[34] contrasted the computed electronic structures of insulating $Bi_2Ti_2O_7$ with that of conducting $Bi_2Ru_2O_7$ and found no difference in the presence or absence of Bi 6s states near the Fermi energy in these two compounds.

Pyrochlore-type rare-earth ruthenium oxides are also of great interest for their magnetic properties. The sub-lattices of corner-connected A_4 and B_4 tetrahedra can result in magnetic frustration when either A or B is separately magnetic [35]. While magnetic properties of $Nd_2Ru_2O_7$ have been reported previously [36], we show here that the presence of ferromagnetic impurity phases compromised the earlier analysis. There has also been some confusion in the literature about the nature of the ordering of the Ru 4d spins in $Nd_2Ru_2O_7$; several reports have suggested that the ordering is glassy [37, 38, 39]. We find compelling evidence that ordering of Ru 4d spins in $Nd_2Ru_2O_7$ is not consistent with spin-glass behaviour, and propose a reason for the observed history-dependence of the ZFC-FC magnetic susceptibility and weak ferromagnetism below the ordering temperature. Heat capacity studies of the magnetic transition in $Nd_2Ru_2O_7$ are also presented here.

In $A_2Ru_2O_7$ pyrochlores the structural modifications between metallic and semiconducting members are small, suggesting that the electrical transport properties are delicately positioned near the edge of localized and itinerant behaviour. This positioning, at the edge of metal-insulator divide, potentially serves as a prime locator for thermoelectric materials: a high Seebeck coefficient is generally found in insulators, with potentially acceptable electrical conductivity on the metallic side, striking the right balance in properties [6, 1]. For this reason, we investigate the high-temperature thermoelectric properties of $Nd_2Ru_2O_7$. When compared to well-known chalcogenide thermoelectric materials (for example, PbTe, Bi_2Se_3, and Bi_2Te_3), metal oxides are of interest due to the expectation of higher stability at elevated temperatures and the prospect of using less toxic and more abundant elements. The discovery of high thermoelectric performance in Na_xCoO_4[26] has led to renewed interest in oxide thermoelectric materials, despite the figure of merit (zT) of this system and other bulk oxide materials being too small for widespread use [1, 40]. Towards the goal of a more directed and effective search for high-performance metal-oxide thermoelectric materials, we also introduce a new type of plot for data visualization that can be used to rapidly screen potential candidates for thermoelectric performance.

2.2 Experimental details

Polycrystalline samples were made by direct reaction of constituent oxide powders (RuO_2, 99.99%, Sigma-Aldrich; Nd_2O_3, 99.99%, Alfa Aesar). Owing to the volatility of

Ru oxides in air at high temperatures ($\geq$1313 K), samples were prepared with a 1 mol% excess RuO_2. Pellets were cold-pressed and annealed at 1273 K for 7 days with several intermediate grindings, after which starting materials were still found by lab XRD. Following this initial reaction, pellets were wrapped in Pt-foil and annealed in evacuated silica ampoules at 1373 K for 7 days. The samples were cooled to 1073 K at 0.5 K/min, and further annealed at 1073 K for 7 days to promote healing of defects. Finally, samples were cooled slowly to room temperature at 0.5 K/min. If $Nd_2Ru_2O_7$ is annealed in air at 1313 K or 1333 K for 12 days, Rietveld analysis of XRD patterns indicates the sample contains 78 mol% Nd_3RuO_7 and 22 mol% $Nd_2Ru_2O_7$ when the annealing temperature is 1313 K, and pure Nd_3RuO_7 when the annealing temperature is 1333 K.

To avoid the formation of Nd_3RuO_7 at the high temperatures and extended annealing times required for solid state reactions, polycrystalline samples of >99% purity were also made by ultrasonic spray pyrolysis (USP) of aqueous nitrate precursors [$Ru(NO)(NO_3)_3$, Sigma-Aldrich; and an aqueous solution of Nd^{3+}, prepared by dissolving Nd_2O_3 in $\approx$2 M HNO_3][41, 42]. A modified ultrasonic humidifier was used to generate a mist, which was passed through a tube furnace (30.5 cm heating zone) at 973 K with a positive pressure of air at a flow-rate of 5 scfm ($\approx$140 L/min). The product was collected in water, and the mixture was evaporated at 343 K; the resulting black solid was cold-pressed into a pellet and annealed in air at 1373 K for 8 hours. Samples were then quenched in air (removed from the furnace at 1373 K) or annealed in air for 7 days at 1073 K then cooled to room temperature at 1 K/min. Rietveld refinement of the structure with synchrotron XRD data revealed no significant differences in the bulk long-range structure between samples that were quenched rapidly and samples that were annealed at intermediate temperatures and cooled slowly, nor were there differences in structure between samples made by USP and samples made by solid state reaction. USP offers a rapid preparatory route to prepare $Nd_2Ru_2O_7$ in $\approx$24 hours, rather than $\approx$14 days.

Laboratory XRD was performed using a Philips X'Pert diffractometer with Cu Kα radiation and using mis-cut Si sample holders to reduce background signal. High-resolution synchrotron X-ray diffraction (XRD) data on finely-ground powder was acquired at 100 K and 295 K at beamline 11-BM at the Advanced Photon Source (APS), Argonne National Laboratory, using an average wavelength of 0.413 Å on a diffractometer that has been described in detail by Wang *et al.* [43]. The precise wavelength was determined using a mixture of Si (SRM 640c)and Al_2O_3 (SRM 676) NIST standards run in a separate measurement. Samples were contained in 0.4 mm diameter Kapton capillaries and the packing density was low enough that absorption was not noticeable. Neutron powder diffraction was performed on the BT-1 diffractometer at the NIST Center for Neutron Research. A Cu(311) monochromator was used, with a constant wavelength of $\lambda =$ 1.5402(2) Å and a second-order contribution at $\lambda/2$. Data was collected at 300 K over the range of 3° to 168° 2θ with a step size of 0.05°. All diffraction data shown here are from a sample made by solid state reaction, though Rietveld analysis of data obtained by synchrotron XRD on other samples made by solid state reaction or USP led to identical results.

X-ray total scattering was performed at beamline 11-ID-B at the APS, using a wavelength of 0.137020 Å. The pair distribution function (PDF) was extracted with PDFgetX2 [44] using $Q_{max} = 28\,\text{Å}^{-1}$, and full-profile PDF structure refinement was completed using PDFgui [45]. R_{wf} and χ^2_{red} were refined on 1950 data points. Key instrumental parameters were $Q_{broad} = 0.0551\,\text{Å}^{-1}$ and $Q_{damp} = 0.00963\,\text{Å}^{-1}$, determined by using a CeO_2 standard in a separate measurement.

Magnetic properties of powders were measured using a Quantum Design MPMS XL-5 SQUID magnetometer. Zero-field cooled (ZFC) and field cooled (FC) measurements were performed between 2 K and 380 K with 100 Oe and 1000 Oe applied dc magnetic field. Data was collected in 0.5 K increments while heating or cooling at 1 K/min. In addition to dc measurements, frequency-dependent ac measurements were performed in a small temperature range between 130 K and 155 K. Low-temperature electrical transport properties and heat capacity were measured using a Quantum Design Physical Properties Measurement System. Samples for electrical transport measurements employed the 4-probe geometry on a pellet of sintered powder with dimensions of approximately 9 mm × 3 mm × 3 mm. Electrical contacts were made with copper wire and silver epoxy. Three samples were run to ensure reproducibility: two made using USP with apparent densities of 38% and 53%, and one made by ceramic preparation with an apparent density of 58%. Electrical resistivity at 300 K varied from 1.2 Ω cm to 2.4 Ω cm between the samples, and is consistent with previous reports of 1.8 Ω cm [10]. Despite slight differences in the magnitude of resistivity, all samples displayed consistent temperature-dependent behaviour. Heat capacity measurements were collected on a pellet of mass 13.90 mg made by pressing 50 wt% of sample and 50 wt% of silver powder (99.99%, Sigma-Aldrich)and analyzed using the thermal relaxation dual-slope method. A thin layer of Apiezon N grease ensured thermal contact between the platform and the sample. The heat capacity of the Apiezon N grease and silver were collected separately and subtracted from the measured sample heat capacity.

High-temperature thermoelectric properties (electrical resistivity and Seebeck coefficient) were measured with an ULVAC Technologies ZEM-3. Sample pellets had approximate dimensions of 9 mm×3 mm×3 mm. Measurements were performed under a helium under-pressure, and data was collected through three heating and cooling cycles to ensure sample stability and reproducibility. No changes in physical properties were observed between cycles, and analysis of the lab XRD pattern of the materials after measurements showed no changes in structure nor new phases. Two different samples (USP and ceramic) were tested to verify consistency.

2.3 Results and Discussion

2.3.1 Structure

The high symmetry ideal pyrochlore crystal structure is completely determined by the cubic cell parameter and a single positional structural parameter, given by the position x of O which is sited at $(x_O, \frac{1}{8}, \frac{1}{8})$. However, there are many types of disorder that arise in this structure type, and a careful examination of the structure is necessary to understand properties. For example, Vanderah *et al.* recently described the widespread presence of antisite disorder on the A-site; up to 25% of the large A-sites can be replaced with small B-site metal ions [46]. Placing large A-site ions on the smaller B-sites is less favourable, though previous studies have shown that antisite disorder on the B-site is also possible [47, 48]. Moreover, local off-centering of A-site cations is well-known in Ru pyrochlores such as $Bi_2Ru_2O_7$ [34, 49]. The presence of disordered oxygen vacancies has been observed in metallic members of $A_{2-x}Bi_xRu_2O_7$ solid solutions [50]. Due to the relatively small X-ray scattering factor of O compared to the other elements present in $A_2Ru_2O_7$, use of only lab XRD has led to inaccurate determination of the O atomic position, as demonstrated by Kennedy and Vogt [50]. This inaccuracy has a large effect on the reported Ru–O–Ru bond angles, which are known to critically influence electrical properties. For example, in $Bi_2Ru_2O_7$, there is a 6° discrepancy, and for other $A_2Ru_2O_7$ members there is up to a 2° discrepancy in the reported Ru–O–Ru bond angles [9, 49, 11].

Combined Rietveld refinement was carried out using room-temperature data sets (Figure 2.2), where the structure was refined on 51295 data points. During the combined refinement, the synchrotron X-ray wavelength was fixed while the neutron wavelength was allowed to vary, though the refined wavelength was within two standard deviations of the starting value determined by previous instrumental calibration. Isotropic displacement parameters were used to describe the electron density of the atoms in the structure, as

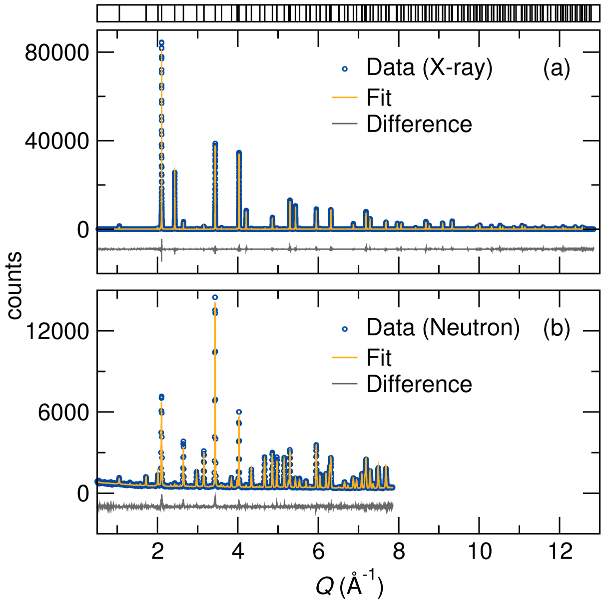

Figure 2.2: Combined Rietveld refinement of the structure with (a) room-temperature synchrotron XRD with $\lambda = 0.41295$ Å and (b) neutron diffraction with $\lambda = 1.5402$ Å. From the refinement, the cell parameter a is determined to be 10.342312(8) Å at room temperature, and the position x_O corresponding to the O atom is 0.33012(7).

refinement of anisotropic displacement parameters did not improve the quality of the fit. Rietveld refinement was performed with XND code[51], and structures were visualized using VESTA [52].

Rietveld refinement of the structure using synchrotron powder XRD (Figure 2.2(a)) data indicates samples were 99.5(1) mol% $Nd_2Ru_2O_7$ and 0.5(1) mol% RuO_2. The minor presence of RuO_2 is not expected to influence the physical properties reported here. There were no significant differences in structure between samples that were quenched rapidly and samples that were annealed at intermediate temperatures and cooled slowly. Additionally, there were no significant differences in structure between samples made by USP and samples made by solid state reaction, nor were there differences between samples annealed under static vacuum and samples annealed in air. Taken together, the long-range structural order of $Nd_2Ru_2O_7$ appears to be insensitive to preparation conditions and methods. In particular, annealing $Nd_2Ru_2O_7$ under low oxygen partial pressures (*i.e.*,

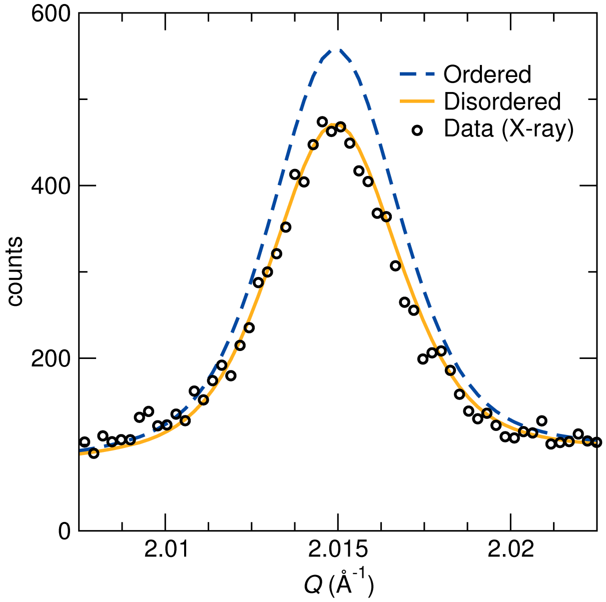

Figure 2.3: Refinement with A-site disorder converges to 7.0(3)% Ru on the A-site and slightly improves the fit to the data, as demonstrated above by the better description of the peak-shape. Changes in the calculated diffraction pattern due to site disorder are small, with the most significant and diagnostic change occurring at the 311 reflection. For comparison, the most intense peak in this pattern has 85 000 counts.

in evacuated ampoules) does not appear to lead to oxygen deficiency. More evidence of this stability is presented in a later subsection, as the electrical resistivity does not change after several heating cycles between 300 K and 900 K under oxygen-free conditions. This suggests that O vacancies not already present in the ordered pyrochlore structure are not formed to an appreciable extent in $Nd_2Ru_2O_7$. To check for the presence of oxygen vacancies, the site occupancy of O$'$ was allowed to refine freely; the best refinements were consistent with complete occupancy. This finding is supported by previous neutron-diffraction studies, which found no evidence for additional oxygen vacancies in $Nd_2Ru_2O_7$ [50]. The oxygen positional parameter $(x_O, \frac{1}{8}, \frac{1}{8})$ converged to $x_O = 0.33012(7)$, identical to previous reports using neutron diffraction [50, 53].

Synchrotron X-ray diffraction studies offer the advantage that the Nd^{3+} and Ru^{4+} X-ray scattering factors are sufficiently distinct due to the large difference in atomic numbers. In contrast, neutron diffraction does not clearly distinguish between the similar coherent scattering lengths of Nd (7.03 fm) and Ru (7.69 fm) [54]. The synchrotron diffraction data allowed the recent findings of Vanderah *et al.* regarding antisite disorder on the cation sites to be tested. The site occupancy and atomic displacement parameters are often correlated, so synchrotron X-ray data was collected at both 100 K and room temperature (295 K). However, these parameters were not strongly correlated in this investigation, and a combined Rietveld refinement using multiple temperatures did not change the outcome of the analysis. Accordingly, we continue our discussion using the combined Rietveld refinement of room-temperature X-ray and neutron diffraction datasets (Figure 2.2). When Ru was allowed to substitute on the A-site, the refinement converged with 7.0(3) mol% Ru and a slight improvement in the fit. A similar trial refinement of Nd on the B-site did not improve the fit. The stability of all refined models (B-site disorder, A-site disorder, no antisite disorder) was verified by perturbing other parameters. Because allowing A-site disorder improves the fit only marginally, it is important to consider whether the improved fit is significant, or if the improvement is merely because more parameters are introduced. Use of a Hamilton test [55] shows the difference is statistically significant at <0.5% confidence interval. Indeed, with only one additional parameter between the two models, the large number of independent measurements makes virtually any improvement in R_{wp} statistically significant. Visual inspection reveals only minor changes between the models, though in the limited areas where antisite disorder causes the largest changes, A-site disorder improves the fit to the experimental peak-shape (Figure 2.3). The same results are obtained in samples made by USP and by solid state reaction. With these considerations in mind, the presence of A-site disorder is suggested.

The X-ray pair distribution function (PDF) obtained by total scattering agrees well with the model generated by the average, long-range structure (Figure 2.4). Refinement of

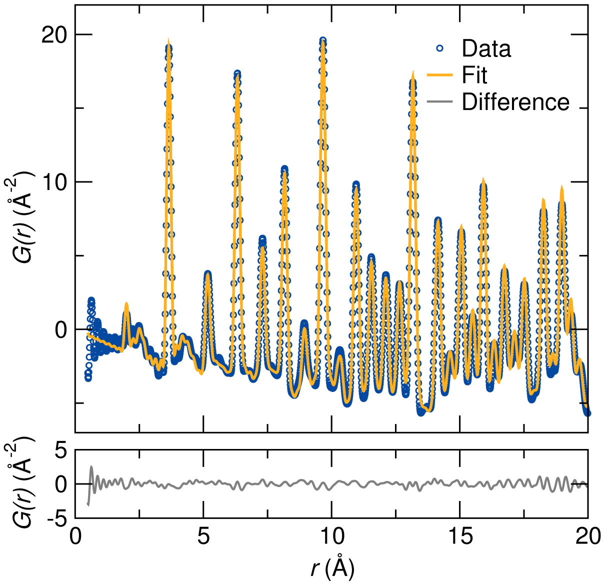

Figure 2.4: Analysis of the synchrotron X-ray PDF reveals $Nd_2Ru_2O_7$ is well-described by an average long-range structural model.

partial Ru substitution on the A-site was attempted, but the refined occupancy converged to unphysical values, potentially due to strong correlation with the scale factor. Ideal cation site ordering $Nd_2Ru_2O_7$ yielded a refinement $R = 10.05\%$ and allowing 7.0% Ru to occupy the Nd site, as suggested from Rietveld refinement, yielded $R = 10.02\%$. The numerical improvement of the fit is marginal, and visual inspection reveals the difference between the models is much less than the level of noise present in the fit to the data. Rietveld refinement of Bragg scattering suggests partial antisite disorder, whereas PDF analysis of the total scattering shows no strong preference between full ordering or partial antisite disorder. This likely occurs because the PDF refinement is strongly weighted by near-neighbor correlations, which has been previously noted in the system La_4LiAuO_8 [56].

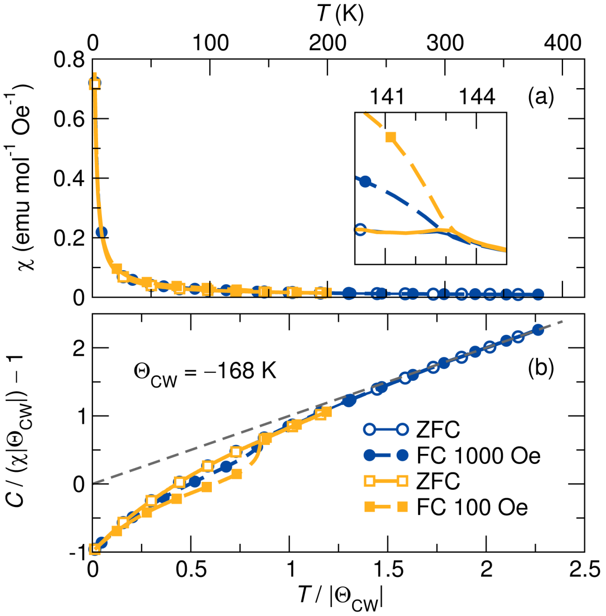

Figure 2.5: (a) Antiferromagnetic ordering of Ru^{4+} 4d spins leads to a small cusp in the ZFC magnetic susceptibility and a splitting of the ZFC and FC curves at 143 K (inset). Nd^{3+} 4f spins do not order at this point, and cause the large increase in susceptibility at lower temperatures. The separation of the ZFC-FC susceptibility is tentatively attributed to spin canting, which leads to weak ferromagnetism. (b) Scaled inverse susceptibility as a function of scaled temperature, as described in the text. The dashed line represents ideal Curie–Weiss behaviour, and the negative deviation in Nd$_2$Ru$_2$O$_7$ is due to short-range ferromagnetic interactions. The Curie–Weiss fit of the high-temperature data reveals a negative Weiss temperature, indicating that the dominant magnetic interactions are antiferromagnetic.

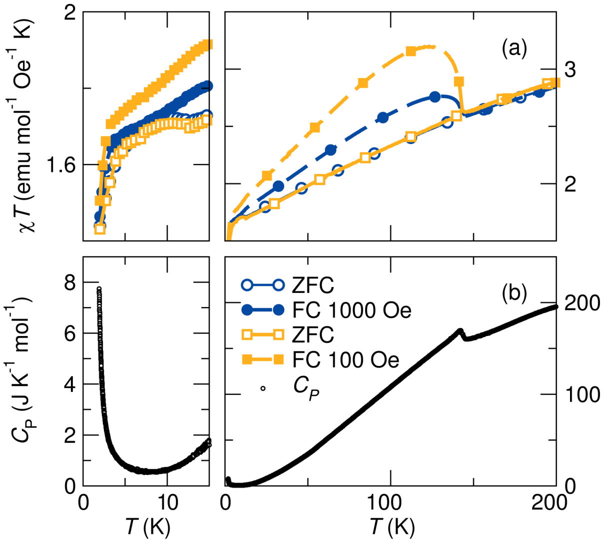

Figure 2.6: (a) The Ru antiferromagnetic ordering seen in the dc magnetic susceptibility at 143 K leads to decreasing χT with decreasing temperature, and corresponds closely with (b) the single anomaly in the heat capacity with a maximum at 142 K. At low temperatures ($T < 5$ K), shown in the left panels, a downturn in χT and an increase in heat capacity are observed, consistent with the onset of Nd antiferromagnetic order.

2.3.2 Magnetic and electrical transport behaviour

Zero-field cooled (ZFC) and field cooled (FC) measurements of the magnetic susceptibility show magnetic ordering of $Nd_2Ru_2O_7$ at $T_N = 143$ K (Figure 2.5), with a small cusp in the ZFC susceptibility. The higher-temperature region (340 K to 380 K) of the susceptibility data was fit to the Curie–Weiss (CW) equation, $\chi = C/(T - \Theta_{CW})$. The effective moment was extracted using the relationship $\mu_{eff}^2 = 3Ck_B/N$, while the estimated spin-only and unquenched moments of $Nd_2Ru_2O_7$ were calculated using $\mu_{eff}^2 = 2\mu_{Ru}^2 + 2\mu_{Nd}^2$. The determined effective paramagnetic moment was $\mu_{eff} = 6.4\,\mu_B$ per $Nd_2Ru_2O_7$ formula unit and the Weiss temperature was $\Theta_{CW} = -168\,K$. The μ_{eff} is close to the calculated spin-only value of $\mu_S = 6.5\,\mu_B$, and significantly less than the calculated unquenched μ_{L+S} of $11.9\,\mu_B$. Curie–Weiss analysis reveals a negative Θ_{CW}, indicating that the dominant magnetic interactions are antiferromagnetic. However, it is apparent from the first derivative (not shown) that the inverse susceptibility remains mildly non-linear as a function of temperature, indicating that $Nd_2Ru_2O_7$ does not display pure Curie–Weiss paramagnetism at these higher temperatures. Consequently, the determined Weiss temperature and μ_{eff} should be treated only qualitatively.

Rearranging the Curie–Weiss equation allows the scaled inverse susceptibility $C/(\chi|\Theta_{\text{CW}}|)-1$ to be displayed as a function of $T/|\Theta_{\text{CW}}|$ and provides a convenient way to visualize deviations from ideal Curie–Weiss paramagnetism [Figure 2.5(b)] [57]. These deviations from Curie–Weiss behaviour are due to short-range interactions, and the negative deviation seen in $Nd_2Ru_2O_7$ arises from uncompensated moments. Additionally, the plot provides a convenient method to visualize magnetic frustration (the frustration index $f = \Theta_{\text{CW}}/T_{\text{N}}$) [58]. Moderately frustrated systems tend to have $f \geq 3$ [58], whereas for $Nd_2Ru_2O_7$ $f = 1.2$, indicating the antiferromagnetic ordering is not strongly frustrated.

Previous studies have shown that the transition at 143 K is the result of antiferromagnetic ordering of Ru^{4+} 4d spins, as an analogous transition is observed in $Y_2Ru_2O_7$, where there are no 4f spins at the A site [35, 39]. This is consistent with the the negative Weiss temperature (Figure 2.5b) and the decrease in χT with decreasing temperature (Figure 2.6a), which indicate the dominant magnetic interactions are antiferromagnetic. However, the Nd^{3+} 4f spins continue to display paramagnetic behaviour, with an increase in susceptibility at lower temperatures. Previous studies have shown the rare-earth (RE) spins in Ru-pyrochlores are slightly polarized by the weak RE-Ru exchange coupling, so the behaviour of the RE spins below ordering of the Ru sublattice is not truly paramagnetic [59, 60, 61]. Additionally, the history-dependence of the ZFC and FC measurements and the increased susceptibility at lower applied fields suggest there are weak uncompensated (*i.e.* ferromagnetic) moments [Figure 2.5]. The weak ferromagnetic interaction saturates at lower applied fields, so it has a diminished contribution to the field-normalized susceptibility at higher applied fields. Meanwhile, the ZFC–FC bifurcation of the mag-

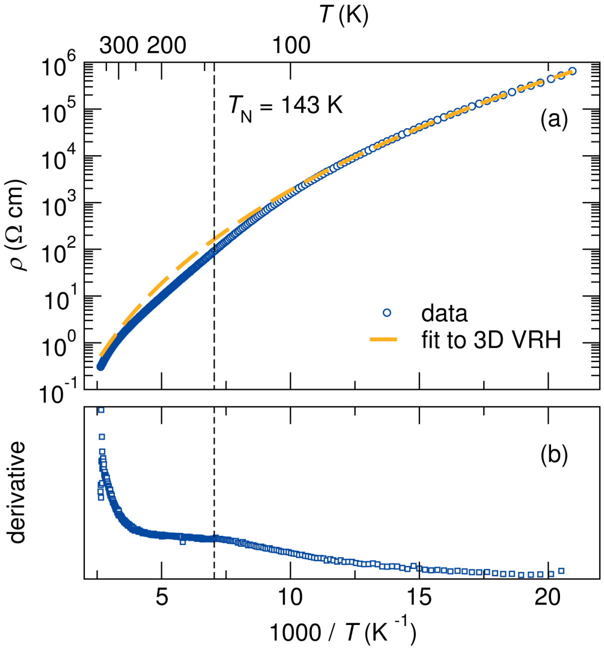

Figure 2.7: (a) Low-temperature electrical resistivity follows a Mott 3D variable-range hopping model, but deviates at the magnetic ordering temperature ($T_N = 143\,K$). Magnetic ordering of the Ru 4d conduction electrons leads to a change in the electrical transport, as shown in the derivative (b).

netic susceptibility is consistent with weak ferromagnetism arising from spin-canting, and is described later in more detail. Below ≈5 K, there appears to be another transition, which causes a downturn in the χT and an upturn in the C_p [Figure 2.6]. Although no maxima are present, these observations are consistent with the onset of Nd 4f antiferromagnetism. This is supported by neutron diffraction experiments on related systems, which have confirmed the onset of long-range RE 4f magnetic order in $Er_2Ru_2O_7$ at low temperatures [59, 60]. Transitions between Nd crystal field levels could also lead to an increase in the specific heat [62], but we would not expect a corresponding change in the magnetic susceptibility (Figure 2.6a).

The antiferromagnetic ordering of Ru 4d spins at $T_N = 143\,K$ causes notable effects in other measurements as well. The specific heat contains a corresponding λ-type anomaly with a maximum at 142 K [Figure 2.6(b)], consistent with a second-order phase transition. Additionally, the electrical resistivity near the magnetic ordering temperature displays anomalous behaviour. An Arrhenius-style plot shows a change in slope at the magnetic ordering temperature (Figure 2.7). Electrical conduction in $A_2\mathrm{Ru}_2\mathrm{O}_7$ materials involves Ru 4d states, and magnetic ordering of Ru 4d spins causes a subtle change in electrical transport due to changes in scattering, as shown in the derivative of Figure 2.7. Low-temperature electrical resistivity follows a 3D variable-range hopping model with $\rho(T) = \rho_0 \exp(\frac{T_0}{T})^{\frac{1}{4}}$ [63, 64], with a change in the hopping barrier at the magnetic ordering temperature ($T_\mathrm{N} = 143\,\mathrm{K}$). Fitting the entire dataset yields $\rho_0 = 5.64\times10^{-10}\,\Omega\,\mathrm{cm}$ and $T_0 = 6.89\times10^{7}\,\mathrm{K}$.

There has been considerable confusion in the literature about the nature of the ordering of the Ru 4d spins in $Nd_2Ru_2O_7$ and analogous Ru-pyrochlores, in part due to the unusual field-dependent hysteresis present between the ZFC and FC susceptibility measurements, and also due to the many types of disorder and exotic phenomena that sometimes accompany geometric frustration in magnetic pyrochlores. In particular, several reports have mentioned that the glassy nature of the ordering of Ru 4d spins is evident in bulk magnetic susceptibility measurements [37, 38, 39, 65, 61]. However, neutron diffraction experiments below the ordering temperature show that Ru spins order with a long correlation length [38, 39]. This is incompatible with a glassy-state, where there is no long-range magnetic order. This is not the only signature of a spin-glass that is violated by experimental evidence. Notably, the temperature-dependence of the specific heat should vary smoothly near the magnetic ordering temperature [66], a stark contrast with the λ-type anomaly at 143 K, shown in Figure 2.6(b).

Ac magnetic susceptibility measurements were also conducted, as another signature of a spin-glass is a magnetic ordering temperature that varies with the frequency of the applied magnetic field [66, 67]. The real, in-phase, component of the ac susceptibility (χ') is shown in Figure 2.8(a),while the imaginary, out of phase, component of the complex

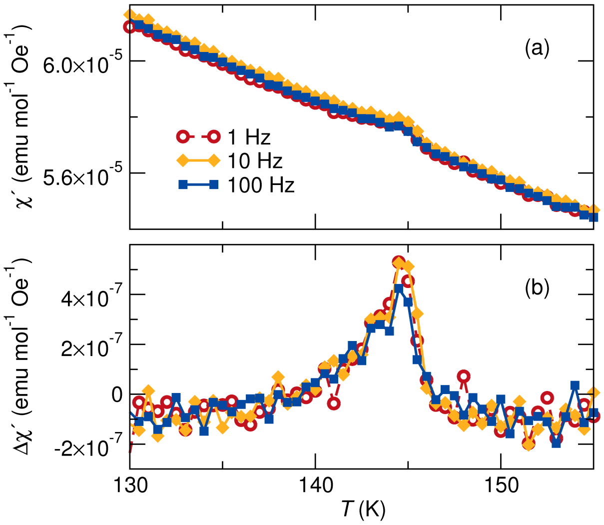

Figure 2.8: (a) The real component of the ac susceptibility shows a small peak due to the antiferromagnetic ordering of Ru 4d spins. (b) Background-subtracted data show the transition temperature is frequency-independent, which indicates the antiferromagnetic ordering of Ru 4d spins is not glassy, and that $Nd_2Ru_2O_7$ is not a spin-glass.

susceptibility (χ'') was below the instrumental detection limit (not shown). Because the response of the Nd^{3+} dominates the total susceptibility, a paramagnetic background was fit using the Curie–Weiss equation and subtracted to obtain the change in susceptibility due to antiferromagnetic ordering of Ru 4d spins [Figure 2.8(b)]. The antiferromagnetic ordering temperature associated with the Ru 4d spins is independent of frequency, which is inconsistent with canonical spin-glass behaviour [66, 67].

A spin-glass, by definition, must lack long-range order and display a frequency-dependent peak in the susceptibility [66, 67]; neither condition is satisfied in $Nd_2Ru_2O_7$. Moreover, owing to the weak exchange coupling between rare-earth 4f spins and Ru 4d spins, the nature of magnetic ordering of Ru 4d spins is not expected to differ as the identity of the rare-earth atom changes in the $A_2Ru_2O_7$ ($A = $ Pr, . . . , Lu, Y) series, so it is also unlikely that other members are spin-glasses.

Adding to the confusion regarding the magnetic behaviour of $A_2Ru_2O_7$ (A = Pr,

…, Lu, Y), previous studies of $Nd_2Ru_2O_7$ have claimed there is ferromagnetic ordering at 20 K, and reported a hysteresis in the low-temperature field-dependent magnetization [36], neither of which were observed here in samples of >99% purity. Additionally, a later study of the specific heat of $Nd_2Ru_2O_7$ showed multiple anomalies at 130 K and 20 K, in addition to the anomaly observed here at 142 K [37]. However, the ferromagnetic ordering at 20 K and the other specific heat anomalies are features of Nd_3RuO_7, a secondary phase that is easily formed during preparation of $Nd_2Ru_2O_7$ and to which we attribute the ferromagnetic ordering and other specific heat anomalies. Extensive study of Nd_3RuO_7 by neutron diffraction, magnetization, and specific heat measurements has shown the material undergoes a transition with a peak at 19 K due to ordering of both Ru^{5+} and Nd^{3+} spins [68]. Additionally, there is a peak in the specific heat at 130 K, corresponding to a first-order structural phase transition. Although preparation of $A_2Ru_2O_7$ (A = Pr, …, Lu, Y) by a ceramic method appears straightforward, care must be taken at high temperatures in air to prevent slow decomposition of the product. To demonstrate this, $Nd_2Ru_2O_7$ was annealed in air at 1313 K and 1333 K for two weeks, and led to the formation of Nd_3RuO_7 as a dominant, or single phase. In the literature, preparation of $Nd_2Ru_2O_7$ appears to consistently lead to appreciable amounts of Nd_3RuO_7 as a secondary phase, with some studies showing up to 10 mol% [38]. Due to the similar properties and chemistry of analogous $A_2Ru_2O_7$ systems, it is not surprising to see similar features near 20 K in the magnetic susceptibility and the specific heat (*e.g.*, ferromagnetic ordering and a λ-type anomaly)[37], as these features may originate from an A_3RuO_7 secondary phase.

2.3.3 Electrical transport in Ru pyrochlores

The nature of the electrical transport behaviour in ruthenium pyrochlores ($A_2Ru_2O_7$) has been of considerable interest, as the nature of the A-site ion dictates whether the material will be insulating (*e.g.*, A = Pr, . . . , Lu, Y) or metallic (*e.g.*, A = Tl, Pb, Bi) [9, 53, 69, 70, 71]. The most intuitive model has sought to explain the different behaviour strictly with the A-site ionic radius, as increasing the A-site radius increases the Ru–O–Ru bond angle. Electrical conduction takes place in the Ru_2O_6 network through overlap of Ru 4d and O 2p orbitals, so a larger Ru–O–Ru bond angle increases this overlap, the bandwidth, and the electrical conductivity [16, 9, 70].

Unfortunately, testing this relationship is not straightforward, as no lanthanide leads to metallic behaviour. Although the La^{3+} radius is similar to Bi^{3+} and should thus be large enough to induce metallic behaviour, $La_2Ru_2O_7$ is outside the pyrochlore stability-field [8, 35, 72]. Several studies interested in the electrical conductivity of these systems have examined solid solutions with Bi or Pb to overcome this hurdle and increase the average ionic radius to the point at which the system becomes metallic [9, 10, 50, 11, 53, 73]. However, it is not appropriate to compare rare-earth Ru pyrochlores with those containing Pb or Tl (*e.g.* $Pb_2Ru_2O_{6.5}$, $Tl_2Ru_2O_{7-y}$), as these contain either A-site ions of different formal charge in the case of Pb^{2+}, or have contributions from overlap between empty 6s states and filled states, as in the case of Tl^{3+}. Even an isovalent substitution of Ln^{3+} by Bi^{3+} may not allow straightforward comparison; structural studies of $Bi_2Ru_2O_7$ have shown that Bi^{3+} atoms are off-centered due to the stereochemically-active $6s^2$ lone-pair [34, 49]. Indeed, Kennedy and Vogt, among others, point out that, while several structural or physical parameters of insulating $A_2Ru_2O_7$ (A = Pr, . . . , Lu, Y) pyrochlores tend to follow a simple trend (*e.g.*, a linear variation in oxygen positional parameter and Ru–O bond distance as a function of lattice parameter), the behaviour of metallic

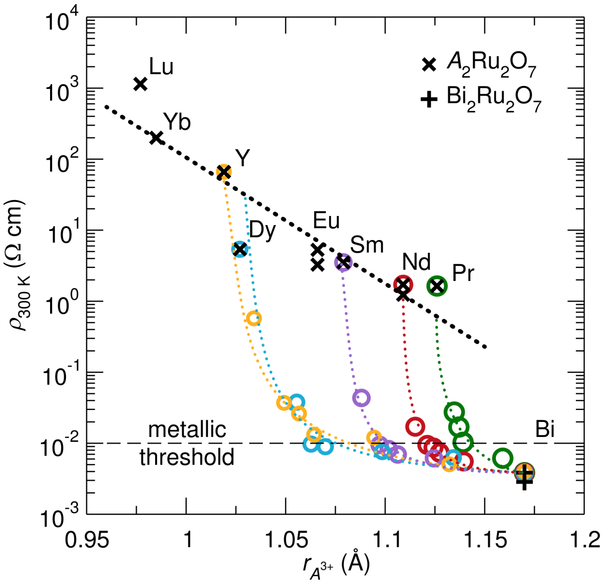

Figure 2.9: Room-temperature electrical resistivity of $A_{2-x}Bi_xRu_2O_7$ (A = Pr, . . . , Lu, Y) solid solutions decrease smoothly with increasing average cation radius. Introduction of Bi drastically changes the behaviour (circles); the materials become metallic near a typical substitution of $x = 0.5$. Dotted lines are guides to the eye, and the thin dashed line at $\rho = 0.01\,\Omega\,\mathrm{cm}$ represents the Mott minimum metallic conductivity at room temperature. Ionic radii of 8-coordinate 3+ cations were taken from Shannon [7]. Values of electrical resistivity were taken from references [8, 9, 10, 11, 12, 13, 14, 15].

ruthenium pyrochlores is aberrant [16, 50].

To examine the influence of the A-site ionic radius on the electrical transport, measurements of the electrical resistivity at 300 K for several Ru pyrochlore systems have been gathered and are presented in Figure 2.9. Although examining the relationship between the Ru–O–Ru bond angle and electrical resistivity might be more direct, the lack of reliable structural data makes the number of available systems less informative. As mentioned earlier in detail, Kennedy and Vogt demonstrated the use of lab XRD has led to inaccurate determination of the O atomic position[50]. On the other hand, the ionic radius is independent of the reported crystallographic data, so it is used as the abscissa in this case. Additionally, when examining these systems and structure-property relationships, it is common to show parameters plotted *vs.* lattice parameter. However, the variation in lattice parameter is strongly influenced by changes in the nature of bonding, as in the case of metallic $Bi_2Ru_2O_7$. For example, even though 8-coordinate Bi^{3+} has a larger ionic radius than Nd^{3+}, ($r_{Bi^{3+}} = 1.17\,Å$, $r_{Nd^{3+}} = 1.109\,Å$) [7], $Bi_2Ru_2O_7$ has a smaller unit cell than $Nd_2Ru_2O_7$ [10].

Casual examination of Figure 2.9 suggests a monotonic decrease in the room-temperature resistivity as the ionic radius of the A site increases, when only the rare-earth-containing pyrochlores ($A_2Ru_2O_7$, $A =$ Pr, ..., Lu, Y) are considered. However, placing a small amount of Bi on the A site dramatically changes the electrical transport; the onset of metallic behaviour occurs at a typical substitution of $x = 0.5$ in $A_{2-x}Bi_xRu_2O_7$. The difference in electrical resistivity is striking, and suggests there is more than the effect of ionic radius when Bi is incorporated into the material. We argue that local distortion of Bi centres in Ru pyrochlores is responsible for the metallic behaviour and the distinct behaviour of $Bi_2Ru_2O_7$ and $A_{2-x}Bi_xRu_2O_7$ when contrasted with Bi-free samples. Other researchers have pointed to the presence of additional oxygen vacancies (other than the ordered vacancy dictated by the pyrochlore structure) and decreased Ru–O bond distance that accompany metallic behaviour [9, 53], though these are a *result*, rather than the cause, of metallic bonding.

2.3.4 High-temperature thermoelectric properties

The electrical transport properties of rare-earth $A_2Ru_2O_7$ ($A =$ Pr, ..., Lu, Y) members are near the onset of metallic behaviour. This unique position is a good place to examine thermoelectric properties, where there is a balance between a high Seebeck coefficient and low electrical resistivity. Electrical resistivity and Seebeck coefficient of $Nd_2Ru_2O_7$ are presented from 300 K to 900 K (Figure 2.10). The thermoelectric properties of $Nd_2Ru_2O_7$ do not change over three measurement cycles, despite the low oxygen

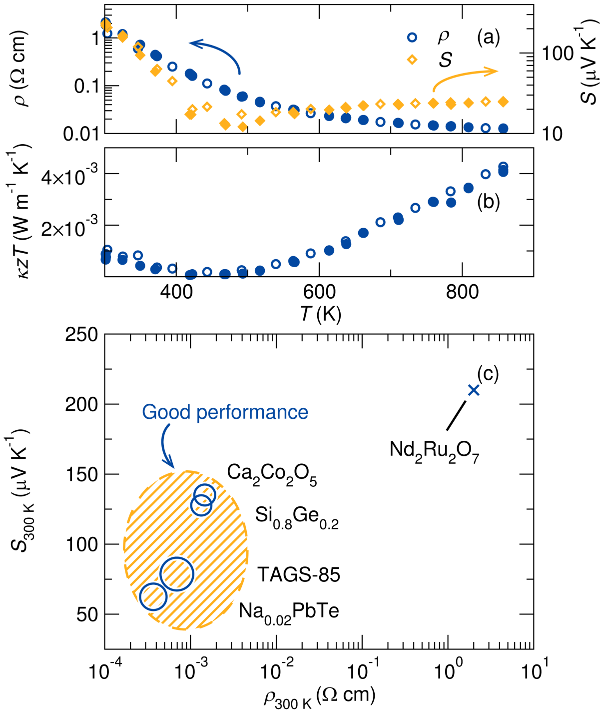

Figure 2.10: (a-b) High-temperature thermoelectric properties demonstrate that $Nd_2Ru_2O_7$ has poor thermoelectric performance from 300 K to 900 K. Three heating and cooling cycles were performed to ensure the stability of the sample; the first cycle is represented by hollow symbols, subsequent cycles by filled symbols. (c) Comparison with high-temperature p-type thermoelectrics reveals that high-performance materials are clustered in one region of the plot, while the performance of $Nd_2Ru_2O_7$ is limited by high resistivity. This method of visualization can be used as a rapid screening tool to determine whether a material is likely to have reasonable thermoelectric performance. The radius of the circle is $\kappa z T$ at 700 K. Since $\kappa z T$ of $Nd_2Ru_2O_7$ is very small, it is represented by $\times$. Values are presented for $Ca_2Co_2O_5$ [74], $Si_{0.8}Ge_{0.2}$ [75], $(AgSbTe_2)_{0.15}(GeTe)_{0.85}$ (TAGS-85) [76], and $Na_{0.02}PbTe$ [77].

partial pressure and high temperature during measurements. The room-temperature electrical resistivity is $2.0\,\Omega\,\mathrm{cm}$, and decreases with increasing temperature, as expected for a non-metal. The room-temperature Seebeck is promising ($\approx$220 μV/K), but quickly decreases with increasing temperature, and $\approx$20 μV/K above 420 K. κzT is also presented [Figure 2.10(b)], as a proxy for the thermoelectric figure of merit, and is several orders of magnitude too small for $Nd_2Ru_2O_7$ to be a competitive thermoelectric material. The thermoelectric figure of merit, zT, is given by $zT = S^2T/(\rho\kappa)$ and is a function of the Seebeck coefficient S, electrical resistivity ρ, thermal conductivity κ, and temperature T. Many materials exhibit a thermal conductivity between $1\,\mathrm{W\,m^{-1}K^{-1}}$ and $10\,\mathrm{W\,m^{-1}K^{-1}}$, so κzT is a useful proxy to compare the electrical performance of thermoelectric materials and estimate zT within an order of magnitude.

Following our investigation of $Nd_2Ru_2O_7$ and learning of its low κzT at high temperatures, we realized that a simple analytical method for estimating the competitiveness of a thermoelectric at high temperatures would be useful for identifying new candidate materials. Such a method would be especially helpful if it did not require high-temperature measurements, as this would save time and resources. Many materials are currently being screened for high-temperature thermoelectric performance, but measurements at elevated temperatures require specialized instrumentation that is not widely available. Room-temperature Seebeck measurements can be performed quickly and with less sophisticated equipment. Additionally, low-temperature (*i.e.*, $T \leq 300$ K) Seebeck and electrical resistivity data are available in the literature for many materials, and could be used to quickly eliminate materials that are likely to have poor thermoelectric performance.

Towards this end, a new type of plot is presented in Figure 2.10(c), where the room-temperature Seebeck ($S_{300\,K}$) is plotted versus the room-temperature electrical resistivity ($\rho_{300\,K}$). The radius of a data point represents the magnitude of κzT at an arbitrary temperature that is common among the data points, and allows easy comparison of the expected thermoelectric performance at that temperature. When examining $Nd_2Ru_2O_7$ and its relation to other high-temperature p-type materials at 700 K using the aforementioned survey plot [Figure 2.10(c)], high-performance materials are clustered in one region of the plot (filled area) while $Nd_2Ru_2O_7$ is isolated. In particular, the location of $Nd_2Ru_2O_7$ indicates the room-temperature electrical resistivity is too high. Because the κzT of $Nd_2Ru_2O_7$ is very small and leads to a vanishingly small point, it is represented by the symbol × in Figure 2.10(c).

This type of analysis is particularly useful in establishing that the performance of a particular class of materials may be ineffectual due to a key property being outside the useful range. The choice of axes is similar to a Jonker plot, in which the Seebeck coefficient is plotted *vs.* electrical conductivity. However, Jonker plots are used to examine the effect of changing the carrier concentration of a single material rather than looking at a field of candidate thermoelectics [78, 79]. Also, while Zhu *et al.* have shown that Jonker plots could be used to to estimate the peak thermoelectric power factor ($S^2\rho^{-1}$) of a material [80], other analyses are involved, and the approach is distinct from the one employed here.

2.4 Conclusion

Pyrochlore $Nd_2Ru_2O_7$ has been prepared and examined using a combination of structural, magnetic, and electrical and thermal transport studies. Some substitutional disorder on the A-site is proposed from the structural studies, but is not anticipated to strongly influence the physical properties. The magnetic behaviour of $Nd_2Ru_2O_7$ has been clarified through a combination of dc and ac magnetic measurements, and heat capacity studies. Despite the potential for geometric frustration of magnetism in the pyrochlore structure-type, we find no such exotic behaviour or glassiness in $Nd_2Ru_2O_7$

above 5 K, and instead tentatively suggest $Nd_2Ru_2O_7$ is a canted antiferromagnet that displays weak ferromagnetism. When the electrical transport properties are regarded in light of published data on rare-earth substituted $A_2Ru_2O_7$ pyrochlores, it is clear that ionic radius plays a key role in determining electrical behaviour. However, the metallic electrical properties that accompany incorporation of Bi^{3+} on the A-site lie outside this description, and we suggest Bi^{3+} off-centering may drive this anomalous behaviour. High temperature measurements of the thermoelectric properties indicate that $Nd_2Ru_2O_7$ has excessively high electrical resistivity for it to be a useful thermoelectric, despite displaying a promising Seebeck coefficient at room temperature. We propose a modified version of the Jonker plot as a powerful tool to screen candidate thermoelectric materials. We find that it is particularly useful in establishing that a particular class of materials may be ineffectual due to a key property being outside the useful range.

Chapter 3

Data-driven review of thermoelectric materials: Performance and resource considerations

---

[1] A version of this chapter has been published, and is reproduced with permission from: Michael W. Gaultois, Taylor D. Sparks, Christopher K. H. Borg, William D. Bonificio, David R. Clarke, and Ram Seshadri. *Chem. Mater.*, 25:2911–2920, 2013. [**doi**] © 2013, American Chemical Society.

In this review, we describe the creation of a large database of thermoelectric materials prepared by abstracting information from over 100 publications. The database has over 18 000 data points from multiple classes of compounds, whose relevant properties have been measured at several temperatures. Appropriate visualization of the data immediately allows insight to the property space of plausible thermoelectric materials. Of particular note is that any candidate material needs to display an electrical resistivity value that is close to $1\,\mathrm{m\Omega\,cm}$ at $300\,\mathrm{K}$; samples should be significantly more conductive than the Mott minimum metallic conductivity. The Herfindahl-Hirschman index, a commonly accepted measure of market concentration, has been calculated from geological data (known elemental reserves) and geopolitical data (elemental production) for much of the periodic table. The visualization strategy employed here allows rapid sorting of thermoelectric materials with respect to important issues of elemental scarcity and supply risk.

3.1 Introduction

The nature of thermoelectric phenomena and materials — competing and contraindicated properties, the complexity and variety of the material systems involved — make it somewhat difficult to develop rational strategies that can lead to significant improvements in performance. Notwithstanding these difficulties, creative approaches have yielded highly promising materials[81, 82, 83, 84, 77, 3, 85, 4]. The guiding principle behind the design of thermoelectric materials, and indeed, any functional material, is to completely understand the causal physics and use such knowledge to rationally optimize material properties. However, even without knowledge of causality, progress across numerous fields is enabled by correlation, without *a priori* understanding of the drivers. Particularly when large datasets are available, robust correlation can be found between seemingly disparate observables. This ability to extract meaningful information from large pools of data has been somewhat under-utilized in the search for new materials.

Thermoelectrics and their historical development have been surveyed by Snyder and Toberer [6]. Nolas *et al.* [28] Goldsmid,[86]. and the two CRC handbooks on thermoelectrics by Rowe [87, 88]. The volume and complexity of research on thermoelectric materials makes the field fertile for a data-driven review — sometimes referred to as data mining, or materials informatics. Informatics-based approaches have been successfully used for estimating some physical properties [89] and the relative stability of selected material systems [90]. and high-throughput methods are becoming increasingly helpful in materials design [91]. Given the volume of information that has been published, knowing the right information to abstract is the first step to such an approach. Furthermore, developing an appropriate visualization strategy to explore the space of thermoelectric materials is crucial. Accordingly, we have reduced the problem of reviewing thermoelectric performance to several key properties at four temperatures of interest, and have created an interactive framework to visualize the large amount of information. Trends in materials properties emerge from such visualization, and lead to guiding principles for the development of high-performance thermoelectric materials. Perhaps more importantly, guidelines are suggested for where *not* to look in the parameter space of candidate materials.

Since the efficiency of a thermoelectric device is related to the thermoelectric figure of merit, $zT = S^2T/(\rho\kappa)$, with S the Seebeck coefficient, ρ the electrical resistivity, and κ the thermal conductivity, these measured parameters were the obvious choice for extraction from publications into a database. A particularly useful format for displaying the large amount of property-based data is based on a modification of a Jonker plot [78], in which the Seebeck coefficient is usually graphed as a function of the electrical conductivity. Jonker plots have traditionally been limited to optimizing the carrier concentration in a single thermoelectric material. In contrast, we display *all* materials in a single plot, with the different material classes grouped by marker color. In the modified version employed by us, we prefer to use the electrical resistivity ρ as abscissa (on a logarithmic scale), and the Seebeck coefficient S as ordinate. The radius of the circular marker represents the performance, which is commonly either zT or the power factor, S^2/ρ.

There is more to a material than just performance. Given the proposed widespread application of thermoelectrics and the potential for high-volume use of materials if certain performance targets are reached, they must be composed of elements that are accessible and not in danger of a supply risk. Crustal abundance of elements, their global production, reserves, and use, are some of the factors that determine supply risk. The criticality of elements in the context of metals that are crucial to energy conversion has been described by Graedel [92]. Homm and Klar have specifically raised these issues for five thermoelectric materials [93]. Following the approach of Graedel [92], we have used our database to calculate several criticality indices for the thermoelectric materials featured here. Resources that are produced almost entirely in a particular region can provide a single entity leverage in determining supplies and prices. This geopolitical influence over materials supply and price can be measured by market concentration, often quantified through the Herfindahl-Hirschman Index (HHI) [94, 95]. The HHI is a financial tool commonly used to measure the monopoly of entities over a commodity or product, and has been previously used as a measure of geopolitical influence on elemental production of a select few elements [96, 92, 97]. Here we calculate the HHI, based on available 2011 data, of almost all of the first 83 elements in the periodic table. Only H, the noble gases, Tc, and Pm are excluded. The HHI is calculated both for elemental production ($\mathrm{HHI_P}$), reflecting the specific geopolitics of the element, as well as for elemental reserves ($\mathrm{HHI_R}$), based on known deposits that could be processed. In conjunction with composition data entered into the database, we employ HHI indices and elemental scarcity values to determine practical issues that influence the likelihood a particular thermoelectric material will find widespread use.

3.2 Methods

3.2.1 Nature and source of data

We have abstracted data from representative publications on a wide variety of thermoelectric materials so they can be accessed and compared easily. The data correspond to four temperatures in different regimes of interest for thermoelectric devices: 300 K, 400 K, 700 K, 1000 K. There are currently over 1100 database entries (rows), each with 17 associated components: temperature, electrical resistivity, Seebeck coefficient, thermal conductivity, power factor, κzT, zT, chemical composition, material family, preparatory route, material form (whether single crystal or polycrystalline), author, year of publication, DOI link, and comments. Additionally, we generate new metadata from the chemical composition of materials, such as $\mathrm{HHI_P}$, $\mathrm{HHI_R}$, scarcity, and average atomic weight, $\bar{M}$. To facilitate comparison of materials, we limit our current systems to bulk samples. In many instances, we employ the power factor or κzT rather than than the actual figure of merit zT for the visualization, because zT requires κ, the thermal conductivity to be measured. Thermal conductivity is not reported for many materials. Furthermore, of all the thermoelectric parameters, thermal conductivity is the least reliable and/or reproducible because it is sensitive to processing conditions.

Data from published work was extracted manually from digital publications using free software such as PlotDigitizer [98] and DataThief [99]. In general, data was extracted from plots of a physical property *vs.* temperature. If data was not explicitly reported at a temperature of interest, values were interpolated, or extrapolated when appropriate. If property traces (curves) were found to rapidly or unpredictably changing in the region of extrapolation, the point was omitted, or data was taken from the nearest reported temperature. In these cases, the temperature of an extrapolated data point is mentioned in the metadata comment. Because data was entered by hand, the power factor and figure of merit (zT) were calculated from the extracted data and checked against the reported values to ensure the data was self-consistent.

HHI values based on production and reserves for each element were calculated from 2011 USGS commodity statistics following the approach used by others [96, 92, 97]. When 2011 data was unavailable, data from 2010 or 2009 was used. This has generated a set of HHI values presented in table 3.1 for much of the periodic table, a significant expansion from previous studies, which focused on eight parent metals [92, 97]. For elements where reserves are seen as adequate or extremely large (*e.g.*, C, O, F, Na, Al, Ca, S, *etc.*) quantitative reserves are not available but their use is unlikely to reduce their availability to critical levels. For elements such as sodium, where multiple commodities are reported separately (carbonates, sulphates, chloride . . .), the reports were combined and the HHI values were generated from the aggregate. Another important consideration is that the production and/or reserve values for a country may be unknown or are withheld. In these instances, where the number of producers and/or the amount of reserves are low, these omissions introduce considerable uncertainty. In these cases, the HHI values were estimated based on the general information provided in the USGS report. Estimates of these elements are denoted by an asterisk in table 3.1.

HHI values were calculated using the following expression, $\text{HHI} = \sum_{i}^{N} s_i^2$, where s_i is the percent market share of country i in the world production or reserves of a given element, and N is the total number of countries with a market share. The US Department of Justice and the Federal Trade Commission have designated markets as unconcentrated

Table 3.1: Herfindahl-Hirschman Index (HHI) calculated for much of the periodic table, using recent USGS data. Asterisks against numbers indicate some uncertainty due to withheld or unknown values.

Element	$\mathrm{HHI}_{\mathrm{P}}$	$\mathrm{HHI}_{\mathrm{R}}$	Element	$\mathrm{HHI}_{\mathrm{P}}$	$\mathrm{HHI}_{\mathrm{R}}$
He	3200	3900	Rb	6000*	6000*
Li	2900	4200	Sr	4200	3000*
Be	8000	4000*	Y	9800	2600
B	2900	2000	Zr	3400	2600
C	500*	500*	Nb	8500	8800
N	1300	500*	Mo	2400	5300
O	500*	500*	Ru	3200*	8000*
F	1500*	1500*	Rh	3200*	8000*
Na	1100	500*	Pd	3200	8000*
Mg	5300	500*	Ag	1200	1400
Al	1600	1000*	Cd	1700	1300
Si	4700	1000*	In	3300	2000*
P	2000	5100	Sn	2600	1600
S	700	1000*	Sb	7900	3400
Cl	1500*	1500*	Te	2900	4900
K	1700	7200	I	4900	4800
Ca	3900	1500*	Cs	6000*	6000*
Sc	5500*	4500*	Ba	3000	2300
Ti	1100	1600	La, . . . , Lu	9500	3100
V	3300	3400	Hf	3400*	2600*
Cr	3100	4100	Ta	2300	4800
Mn	1600	1800	W	7000	4300
Fe	2400	1400	Re	3300	3300
Co	3100	2700	Os	5500*	9100*
Ni	1000	1500	Ir	5500*	9100*
Cu	1600	1500	Pt	5500	9100*
Zn	1600	1900	Au	1100	1000
Ga	5500*	1900*	Hg	5500	3100
Ge	5300	1900*	Tl	6500*	6500*
As	3300	4000*	Pb	2700	1800
Se	2200	1900	Bi	5300	6000
Br	3300	6900			

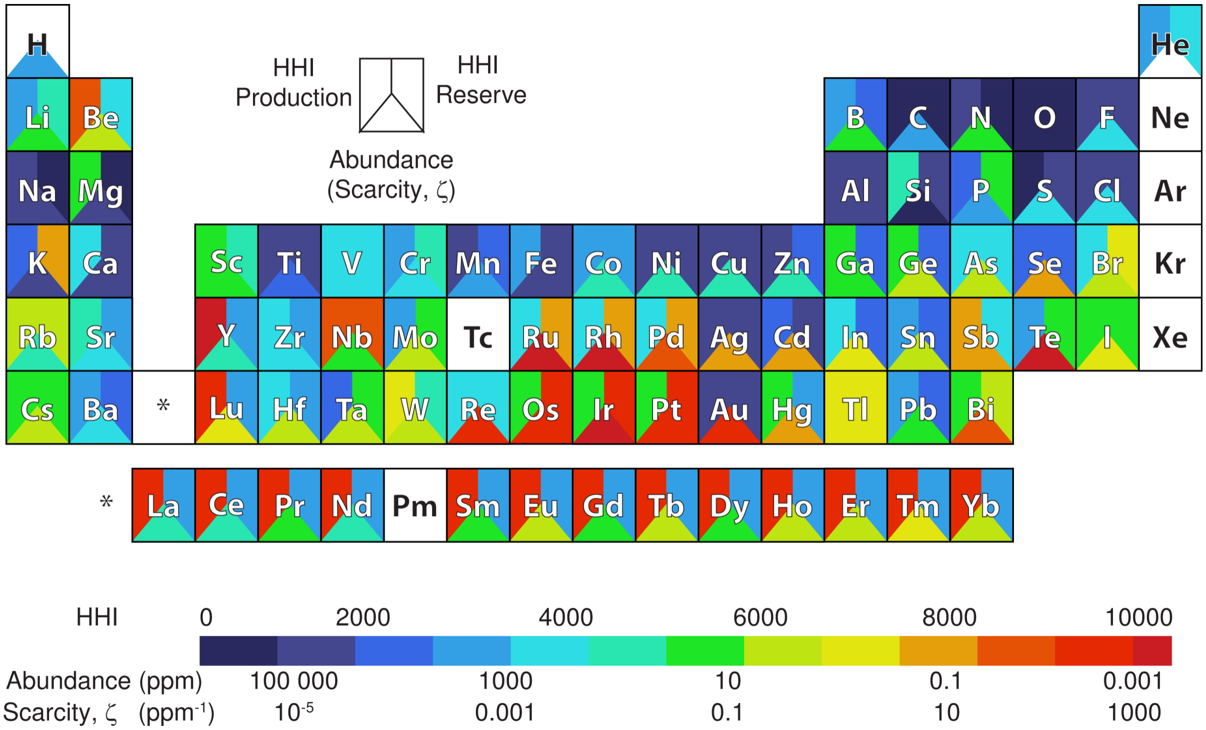

Figure 3.1: Periodic table indicating elemental scarcity and the HHI (production, reserves) indices for most elements. Values were calculated using USGS statistics from 2011, or if unavailable, from statistics no earlier than 2009.

when $\mathrm{HHI} < 1500$, moderately concentrated when the HHI lies between 1500 and 2500, and highly concentrated when $\mathrm{HHI} > 2500$ [100]. If a single country controlled the entire market, $\mathrm{HHI} = 100^2$. Elemental HHI values were then used to calculate weighted HHI production and reserve values based on the *weight* fraction of each element in the chemical formula. Atomic weights were taken from the CRC Handbook [101]. The crustal abundance of elements were obtained from the CRC Handbook and used to generate elemental scarcity values, ζ (crustal abundance in inverse ppm). These scarcity values were used to calculate the effective scarcity of materials based on the weight fraction of elements in the chemical formula, $\zeta = \sum_i^N (\zeta_i \times \frac{m_i}{m_{tot}})$ where ζ_i and m_i are the scarcity and weight of an element i in a material. The scarcity and Herfindahl-Hirschman Index values (based on production and reserves) for much of the periodic table is shown schematically in Figure 3.1.

3.2.2 Mechanics of visualization

At the initial stages of this work, it became evident that gathering large amounts of data would be futile in the absence of an appropriate framework that permitted flexible visualization. In this section we describe a website we have developed and hosted at `www.mrl.ucsb.edu:8080/datamine/thermoelectric.jsp` as an example of a plausible framework for organizing and visualizing the results of such data mining. The flowchart describing the data mining, database formation, and visualization process is summarized in Figure 3.2. A screenshot of the website is shown in Figure 3.3. Because several physical parameters were collected and tabulated, visualizing any number of combinations along the abscissa and ordinate is possible using the website. While not all combinations will yield insightful relationships, the following choices are supported by the website: electrical resistivity, Seebeck coefficient, thermal conductivity, average atomic weight,

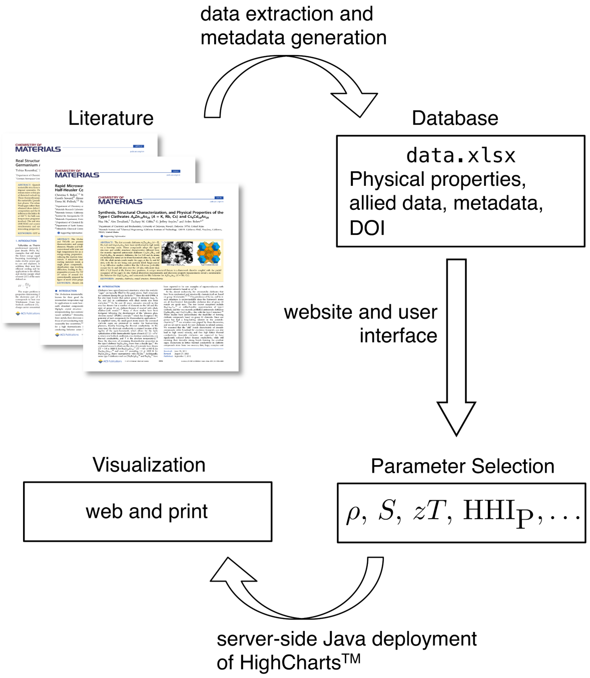

Figure 3.2: Flowchart for extraction, organization, and visualization of data. Note that the first step of data extraction is manual.

elemental scarcity, and HHI based on production or reserves of a material. To increase the information density that can be visualized, a third dimension is also plotted: the size of the data point (the radius of a circle) is proportional to material performance. The marker size can be either power factor (S^2/ρ), κzT, or zT. κzT allows a rough comparison with zT, but does not require the thermal conductivity to have been measured or reported. Many materials have a thermal conductivity between $1\,\mathrm{W\,m^{-1}K^{-1}}$ to $10\,\mathrm{W\,m^{-1}K^{-1}}$, and in the case that $\kappa = 1\,\mathrm{W\,m^{-1}K^{-1}}$, the numerical value of κzT is the same as the numerical value of zT.

The website allows interactive exploration of all the data. Hovering over a data point reveals a tooltip with pertinent information: the values for the abscissa and ordinate, the chemical composition, the sample form (*e.g.*, polycrystalline, single crystal, nanoparticles), the preparatory route (*e.g.*, ceramic method, arc melting), the author and year, and either the power factor, κzT, or zT value. Additionally, clicking on a data point leads

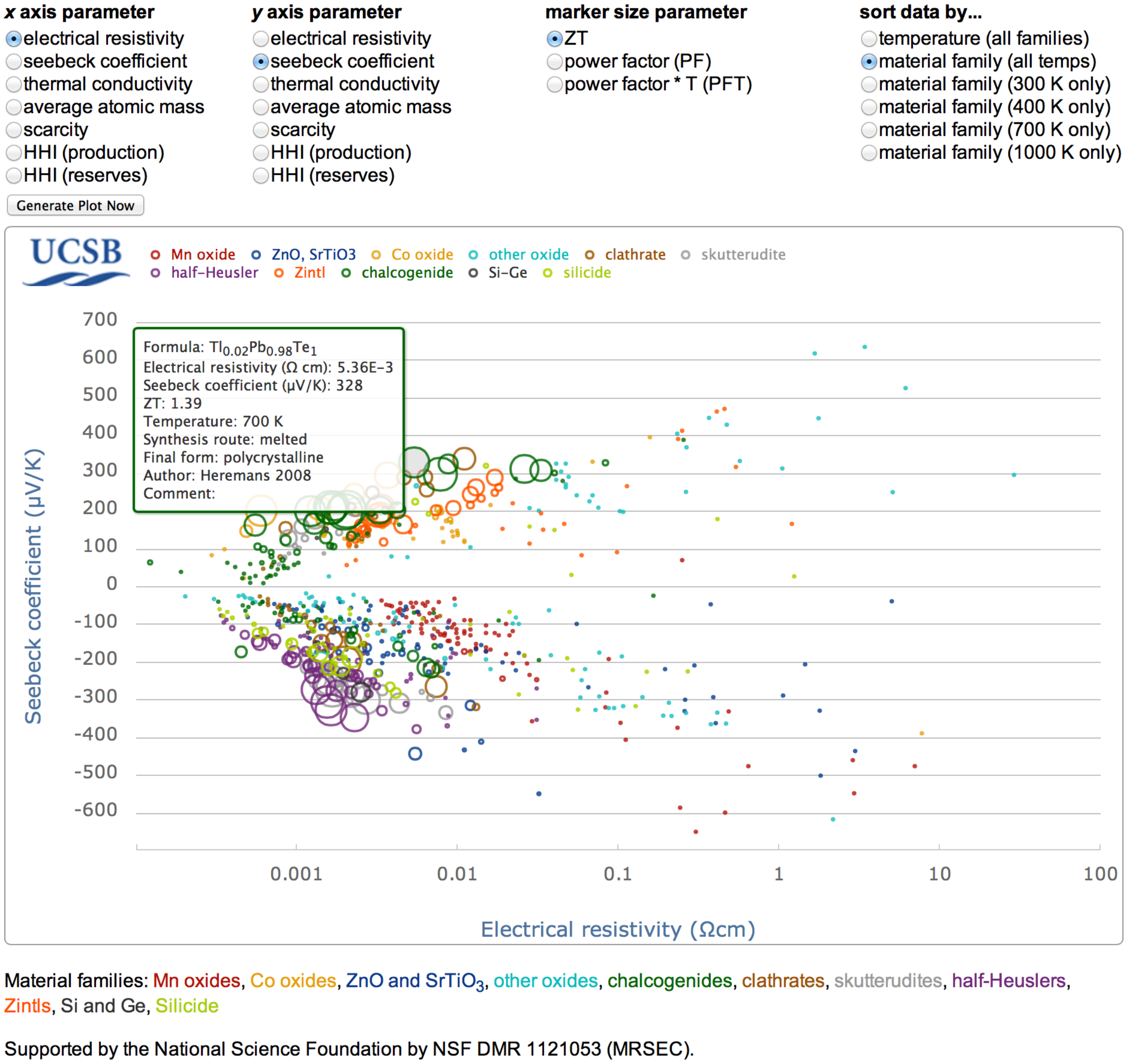

***x* axis parameter**
- ● electrical resistivity
- ○ seebeck coefficient
- ○ thermal conductivity
- ○ average atomic mass
- ○ scarcity
- ○ HHI (production)
- ○ HHI (reserves)

***y* axis parameter**
- ○ electrical resistivity
- ● seebeck coefficient
- ○ thermal conductivity
- ○ average atomic mass
- ○ scarcity
- ○ HHI (production)
- ○ HHI (reserves)

marker size parameter
- ● ZT
- ○ power factor (PF)
- ○ power factor * T (PFT)

sort data by...
- ○ temperature (all families)
- ● material family (all temps)
- ○ material family (300 K only)
- ○ material family (400 K only)
- ○ material family (700 K only)
- ○ material family (1000 K only)

Formula: $Tl_{0.02}Pb_{0.98}Te_1$
Electrical resistivity (Ω cm): 5.36E−3
Seebeck coefficient (μV/K): 328
ZT: 1.39
Temperature: 700 K
Synthesis route: melted
Final form: polycrystalline
Author: Heremans 2008
Comment:

Material families: Mn oxides, Co oxides, ZnO and $SrTiO_3$, other oxides, chalcogenides, clathrates, skutterudites, half-Heuslers, Zintls, Si and Ge, Silicide

Supported by the National Science Foundation by NSF DMR 1121053 (MRSEC).

Figure 3.3: Screenshot of the web-based visualization tool, that permits the simultaneous visualization of four parameters: abscissa, ordinate, marker size and color. Several variables can be chosen as abscissa and ordinate, and measures of thermoelectric performance can be represented by the radius of the data points. To simplify navigation, families of related materials can be displayed or hidden by clicking their legend marker. Further, hovering over a data point intuitively reveals a tooltip with pertinent information: the names and values for the abscissa and ordinate, the chemical composition, the sample form (*e.g.*, polycrystalline, single crystal, nanoparticles), the preparatory route (*e.g.*, ceramic method, arc melting), the author and year, and either the power factor, κzT, or zT value. Clicking on a data point leads the web-browser directly to the source publication *via* the document object identifier (DOI).

the web-browser directly to the publication *via* the document object identifier (DOI). To enable sorting of the large number of datasets, the user may choose to sort by material family or temperature regime. Although the material families are shown with different marker color, the ability to hide or show a given family can make direct comparison more clear. This is accomplished by clicking the name of the dataset in the legend. Finally, users can visualize the results of the thermoelectric database employed here, or upload their own data using an Excel$^{\text{TM}}$ template file available on the website. In this way a user can look for trends in their data or use the website's Java$^{\text{TM}}$ code to generate additional non-performance-related data such as scarcity, average atomic weight or HHI.

3.3 Results and discussion

3.3.1 Examples of useful visualization schemes

In table 3.2, we list those combinations of parameters that we have found particularly useful to plot. The various combinations and the findings are described more thoroughly in the following sections.

3.3.2 Rapid screening of materials

We begin by visualizing the general trend in Seebeck coefficient as a function of the electrical resistivity (Figure 3.4): These two properties jointly contribute to zT. Higher information density is achieved by encoding the power factor as the marker size. This style of plot was first introduced in a previous report [32]. Here we enhance it by assigning a color to a family of related materials. Although the axes are similar to those for a Jonker plot (where Seebeck coefficient is plotted *vs.* electrical conductivity) the application is quite distinct. Jonker plots are usually employed to examine the effect of changing the

Table 3.2: The flexibility of the visualization framework allows users to examine the relation between any number of different parameters. Several examples are tabulated here, along with what can potentially be learned.

Abscissa	Ordinate	Size (radius)	Use	Finding
ρ	S	S^2/ρ, κzT, zT	General trends, insight	Compound must be metallic (ρ from $0.001\,\Omega\,\mathrm{cm}$ to $0.01\,\Omega\,\mathrm{cm}$) for high performance
$\bar{M}$	κ	κzT, zT	Effect of $\bar{\omega}$	κ decreases with increasing $\bar{M}$
$\rho_{300\,\mathrm{K}}$	$S_{300\,\mathrm{K}}$	κzT, zT at different temperatures	estimate high-T performance	Rapid screening of high-T materials
ρ	κ	κzT, zT	Effect of κ_e	Slope of κ *vs.* ρ changes linearly with T of dataset
$\mathrm{HHI_P}$	$\mathrm{HHI_R}$	κzT, zT	Material choice and criticalilty	Intensive use of rare-earths and/or Sb may strain markets
ζ	$\mathrm{HHI_P}$	κzT, zT	Material choice and criticalilty	Some elements are abundant, yet will have volatile prices. Many state-of-the-art high-performance materials rank poorly in criticality indices

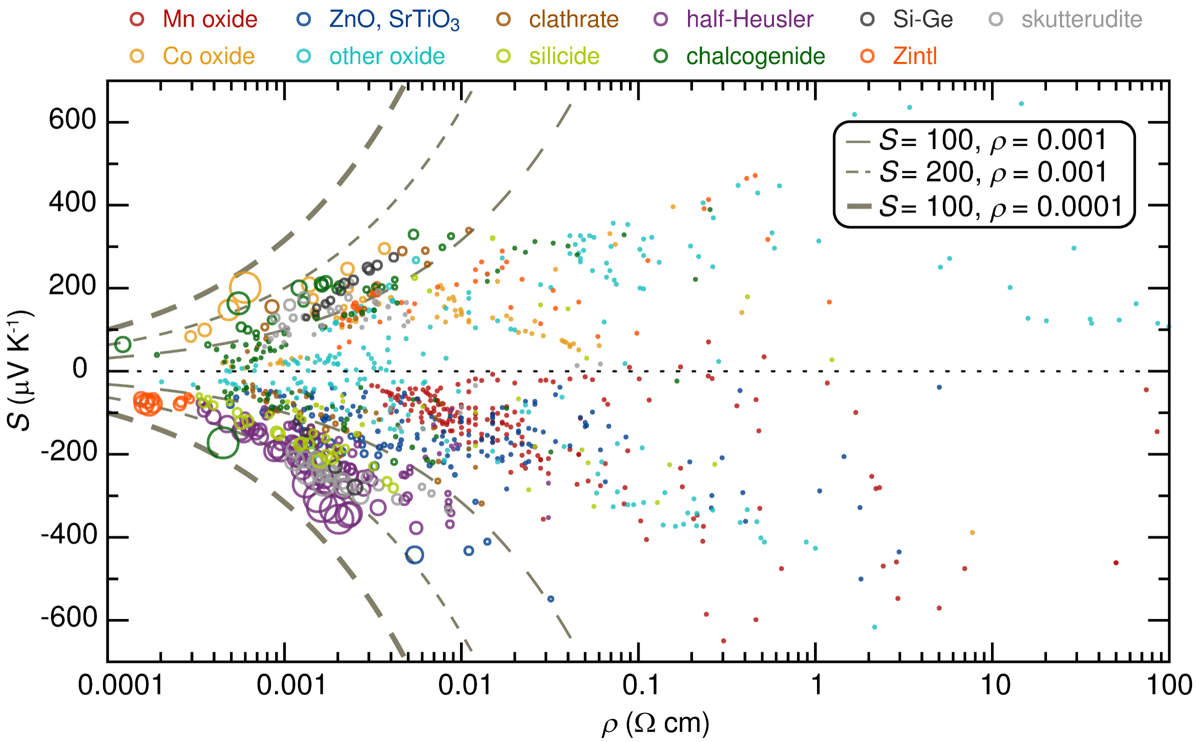

Figure 3.4: The Seebeck coefficient of a wide variety of materials grouped by material family is plotted against electrical resistivity. The marker size (radius) here is proportional to the the power factor. Materials with high performance exhibit an high Seebeck coefficient at a given electrical resistivity, and lie outside the conical envelope defined by most thermoelectric materials. This envelope can be described by lines of constant power factor (S^2/ρ), which are shown to give lower and upper bounds of performance. With few exceptions, all investigated materials with reasonable thermoelectric performance are well described as metals ($\rho_{300\,\mathrm{K}} << 0.01\,\Omega\,\mathrm{cm}$).

carrier concentration in a single material [78, 79].

Looking at the data as a whole, the general envelope of materials is cone-like, widening at higher electrical resistivities (Figure 3.4). The best materials clearly define the left-most edges of the envelope. All the high-performance materials have interesting physics that make them special, even when looking only at the these two properties. Specifically, materials with metallic behavior generally have low Seebeck coefficients, but high-performance thermoelectric materials violate this principle. For example, band asymmetry or high band degeneracy near the Fermi level in BiTe- and PbTe-based systems leads to an unusually high Seebeck coefficient, despite their metallic behavior [102, 77]. Likewise, even though Na_xCoO_2 is metallic ($\rho_{300\,\mathrm{K}} \approx 0.002\,\Omega\,\mathrm{cm}$ for polycrystalline samples); the correlated behavior of electrons and spin contribution to thermopower–or, arguably, the unique band structure–lead to a remarkably high Seebeck coefficient [103, 104].

Looking at the ensemble of data (Figure 3.4) also provides insight about particular families of materials. For example, we find that optimizing non-metallic moderate-performance materials is unlikely to lead to dramatic gains in performance, as the electrical resistivity is too high. For example, $CaMnO_3$-based systems remain a topic of intense study, but when viewed in the context of all materials, their placement in the map suggests it is unlikely that high performance will ever be reached.

It was previously shown that room-temperature thermoelectric properties (Seebeck coefficient and electrical resistivity) of several high-performance thermoelectric materials clustered in one area of the thermoelectric map (Figure 3.4) when compared with low-performance materials [32]. Here we suggest that the relationship between the properties at room-temperature and the properties at the temperature of highest zT for a small set of mid- and high-temperature thermoelectric materials (Figure 3.5). Interestingly, the properties of several different material families appear to cluster at their temperature of highest zT, with the electrical resistivity between $0.001\,\Omega\,\mathrm{cm}$ and $0.01\,\Omega\,\mathrm{cm}$ and the

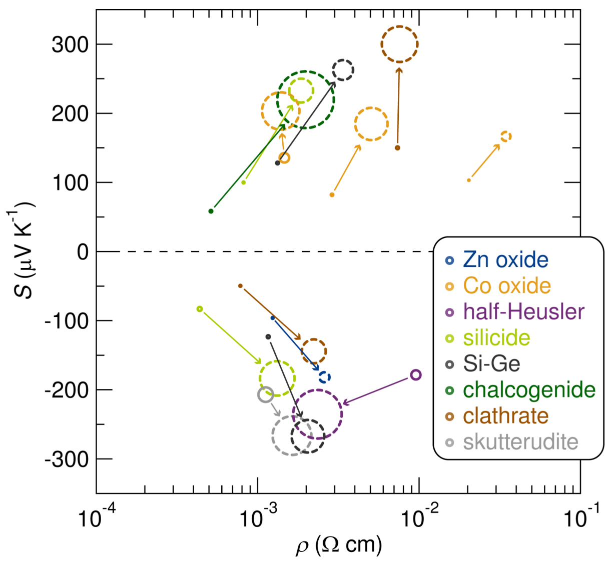

Figure 3.5: Several high-performance thermoelectric materials were chosen to examine how their room temperature properties relate to their properties at the temperature of highest zT. Arrows show the change from room temperature (solid circles) to the temperature of highest zT (dashed circles). The properties of several different material families appear to cluster at their temperature of highest zT, with the electrical resistivity between $0.001\,\Omega\,\mathrm{cm}$ and $0.01\,\Omega\,\mathrm{cm}$ and the absolute value of the Seebeck coefficient between $150\,\mu\mathrm{V\,K^{-1}}$ and $300\,\mu\mathrm{V\,K^{-1}}$. Additionally, nearly all high-performance materials have a room-temperature electrical resistivity below the Mott maximum metallic resistivity ($\rho_{300\,\mathrm{K}} < 0.01\,\Omega\,\mathrm{cm}$). The materials shown are $\mathrm{Zn_{0.98}Al_{0.02}O}$ [105], $\mathrm{Na}_x\mathrm{CoO_2}$ [106], $\mathrm{Ca_2Co_2O_5}$ [74], $\mathrm{(Zr_{0.5}Hf_{0.5})_{0.5}Ti_{0.5}NiSn}$ [107], $\mathrm{Mg_2Si_{0.999}Bi_{0.001}}$ (p-type) [108], $\mathrm{(Mg_2Si)_{0.97}Bi_{0.03}}$ (n-type) [109], $\mathrm{Si_{0.8}Ge_{0.2}}$ (p-type) [75], $\mathrm{Si_{0.8}Ge_{0.2}}$ (n-type) [75], $\mathrm{PbTe_{0.75}Se_{0.25}}$ [77], $\mathrm{CsBi_4Te_6}$ [110], $\mathrm{Ba_8Ga_{18}Ge_{28}}$ (p-type) [111], $\mathrm{Ba_8Ga_{16}Ge_{30}}$ (n-type) [112], and $\mathrm{In_{0.25}Co_4Sb_{12}}$ [113].

absolute value of the Seebeck coefficient between $150\,\mu\mathrm{V\,K^{-1}}$ and $300\,\mu\mathrm{V\,K^{-1}}$. Although the small dataset prevents any strong conclusions, examining more materials may provide some predictive ability of high-temperature properties from room temperature data. Even some hints with regard to high-temperature properties would be powerful: measurement of high temperature properties is time-consuming and requires specialized instruments. Furthermore, there is much more room-temperature data available in the literature and a single room-temperature measurement could facilitate combinatorial testing of a large phase space [114].

The thermoelectric survey shown in Figure 3.4 and the high-temperature trends observed in Figure 3.5 suggest that all thermoelectric materials with any appreciable performance are metallic, with an electrical resistivity well below the Mott maximum metallic resistivity at room temperature, *i.e.* $\rho_{300\,\mathrm{K}} < 0.01\,\Omega\,\mathrm{cm}$. This provides a valuable thermoelectric screening criterion and guiding direction for future studies. Unlike intermetallic compounds, which are generally metallic or semi-metallic, transition metal oxides span the gamut of electrical resistivities, ranging from insulating (*e.g.* $\mathrm{TiO_2}$) to metallic (*e.g.* $\mathrm{ReO_3}$). A common strategy to seeking effective thermoelectric oxides is to examine the metal/non-metal border, *i.e.* proximal to the Mott minimum metallic conductivity, where Seebeck coefficients are often substantial. However, the utility of this approach appears somewhat questionable, given that the good thermoelectrics appear well on the metallic side.

3.3.3 Thermal conductivity

Over the past several decades, the majority of improvements in thermoelectric materials have resulted from decreasing the lattice contribution to thermal conductivity. A number of materials selection guidelines have been identified in order to reduce the

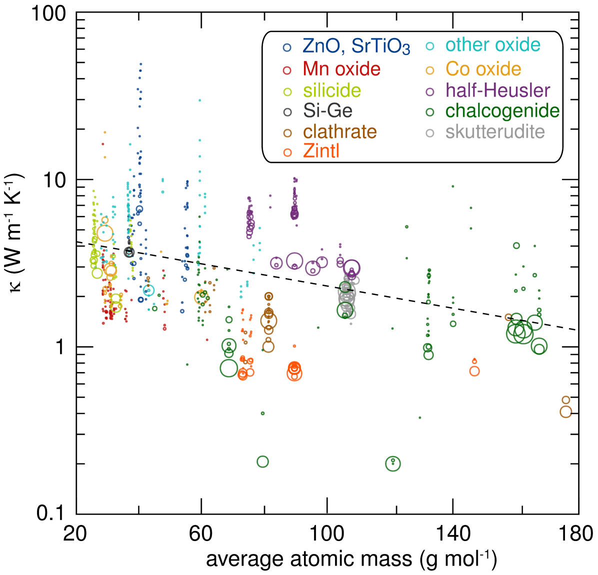

Figure 3.6: Thermal conductivity plotted against average atomic weight for a variety of thermoelectric materials grouped by material family, with marker indicating zT. The dashed line represents a best fit linear regression. Notwithstanding the combination of pure phase materials and heavily nano-structured materials, the thermal conductivity generally decreases with increasing average atomic weight. However, at fixed average atomic weight, there is considerable tunability.

thermal conductivity in a material [115, 116, 6]. One such strategy is to lower the vibrational frequency, and thus the thermal conductivity, by using materials with a large average atomic weight. This has frequently been touted as a reason for the higher thermal conductivity in oxides relative to compounds with heavier anions such as Te, Se, and Sb. Examination of the relationship between thermal conductivity, κ, and average atomic weight, $\bar{M}$, confirms the general reduction of thermal conductivity in heavier compounds (Figure 3.6). For example, compounds with $\bar{M} \approx 25\,\mathrm{g/mol}$ have an average $\kappa \approx 4\,\mathrm{W\,m^{-1}K^{-1}}$ whereas those with $\bar{M} \approx 105\,\mathrm{g/mol}$ have an average $\kappa \approx 2\,\mathrm{W\,m^{-1}K^{-1}}$. In the absence of point defects or other scattering mechanisms, the reduction in thermal conductivity should scale as $\bar{M}^{-1/2}$ [117]. However, many of the materials contained in this plot rely on additional techniques to reduce thermal conductivity (*e.g.*, increased phonon scattering from defects, alloying, grain boundaries, interfaces, nano-bulk com-

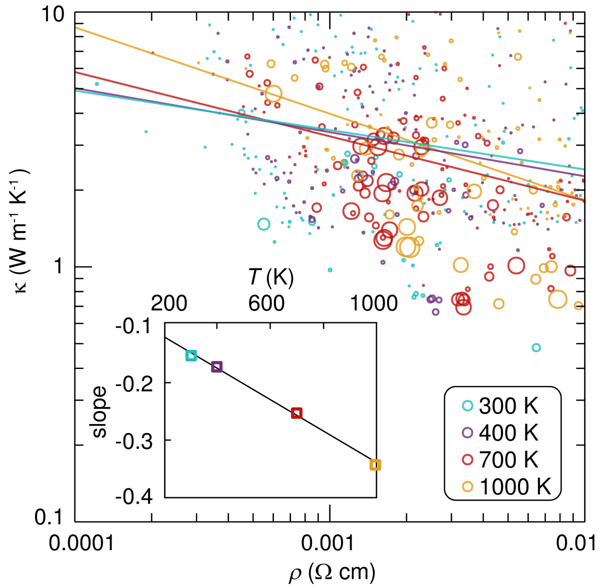

Figure 3.7: Thermal conductivity plotted against electrical resistivity for a variety of thermoelectric materials grouped by dataset temperature with marker size indicating zT. Lines are best fit linear regressions of the data plotted on log-log plot. The slopes are then plotted as a function of dataset temperature in the inset. Despite the large scatter in the data that has been fitted, the general trend that emerges is consistent with the T^{-1} dependence of Umklapp scattering of phonons.

pounds, complex crystal structures, *etc.*). On the other hand, the lower vibrational frequency achieved in compounds with large average atomic weight has only a small impact on the electrical resistivity.

Finally, we examine the relationship between total thermal conductivity and electrical resistivity (Figure 3.7); the thermal conductivity decreases with increasing electrical resistivity. This behavior is expected for the electronic contribution from the Wiedemann-Franz law, $\kappa_e/\sigma = \pi^2 k_B^2/3e^2T = L_0T$ where L_0 is the Lorenz number ($2.44 \times 10^{-8}\,W\,\Omega\,K^{-2}$) and σ is the electrical conductivity. There is another consideration that could be important. For a given composition, the same structural features that give rise to low electrical resistivity, — for example, a highly connected three-dimensional framework — are the same features that often lead to high lattice thermal conductivity.

Examining the broad correlation across all material families in the metallic region

Table 3.3: General class of material family and publications from which data was extracted. Representative publications are chosen for each class of materials.

Material family	References
Mn oxide	[118, 119, 120, 121, 122, 123, 124, 125, 126, 127, 128, 129]
ZnO, $SrTiO_3$	[130, 131, 132, 133, 134, 135, 136, 137, 105, 138, 139, 140, 141]
Co oxide	[142, 74, 143, 144, 106, 145, 146]
other oxide	[147, 148, 149, 32, 150, 151, 152, 153, 154, 155, 132, 156, 157, 158, 159, 160, 161, 162, 163, 164, 165]
Si-Ge	[75, 166]
clathrate	[112, 167, 168, 169, 170, 111, 171, 172]
half-Heusler	[173, 174, 175, 107, 176]
skutterudite	[113, 85, 177, 81]
chalcogenide	[178, 76, 77, 102, 179, 110, 180, 181, 182, 183, 184, 185, 186, 187, 188, 189, 190]
silicide	[108, 191, 192, 109, 193, 194]
Zintl	[195, 196, 197, 198, 199, 200]

($\rho < 0.01\,\Omega\,\mathrm{cm}$) reveals the slope of the log-log plot κ *vs.* ρ decreases linearly with increasing temperature (inset, Figure 3.7). The power-law behavior revealed from the fit is consistent with Umklapp scattering, explained below. Examining correlations across many material families with disparate properties will only provide general trends rather than precise values for a specific material family (Table 3.3). Nevertheless, there is insight to be gained by comparing the correlation (*i.e.* slope) at different temperatures. For example, while there is considerable scatter in the data at each temperature, the temperature dependence of the correlation is strongly linear ($R^2 = 0.997$), in good agreement with the expected behavior as Umklapp scattering begins to dominate at higher temperatures. The changing slope as a function of dataset temperature results from increased phonon scattering lowering the phonon contribution to thermal conductivity at higher temperatures. When the lattice κ_l is minimized, the electronic κ_e dominates, so changes in electrical resistivity have a larger impact on thermal conductivity. The power dependence of temperature on κ *vs.* ρ slope may result from the Umklapp scattering, a three-phonon scattering process. According to the Bose-Einstein expression, $< n >= 1/(exp[\hbar\omega/k_BT] - 1) \approx k_BT/\hbar\omega$, the average phonon population, $< n >$, increases with temperature which increases the likelihood of phonon-phonon scattering. In fact, Grimvall has predicted a T^{-1} temperature dependence for three-phonon scattering at moderate temperatures (near the Debye temperature) [117].

3.4 Resource considerations

In this section we review parameters beyond thermoelectric performance. We analyze resource considerations such as scarcity and supply risk of thermoelectric materials based on their elemental composition. The implications of the analysis on the choice of thermoelectric materials is discussed below. A combined analysis of performance and resource considerations is necessary for identifying thermoelectric materials with the greatest promise of widespread application. Scare elements could be employed in efforts to make high-impact discoveries and to obtain better understanding of materials trends. However, when materials are intended for widespread deployment, the incorporation of scarce elements becomes an important point to consider during the design phase.

We begin by discussing scarcity which places a fundamental limit on the amount of material available for use. The following section addresses HHI, a measure of geopolitical influence. Abundance of raw materials is a key factor that determines cost, in addition to other factors such as actuarial costs, packaging, transportation, and assembly, to name a few. Technologies relying on scarce elements such as Re, Te, or Pt group metals, are susceptible to large materials costs. For example, turbine engines consume 70% of the world's Re production, which drives the cost of Re [201]. The cost of scarce materials

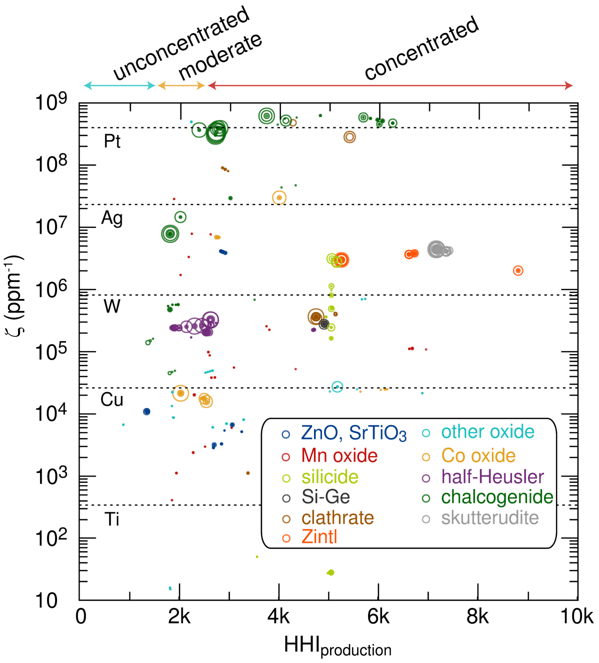

Figure 3.8: Nearly all high-performance thermoelectric materials pose either a scarcity or HHI risk, which will limit any intensive deployment for energy applications. The scarcity (inverse crustal abundance) of familiar elements is shown to give context. Incorporation of Bi, Sb, Te, or rare-earth elements leads to significant risk in either scarcity or HHI. Materials that pose a lower risk of criticality are SiGe, silicides, half-Heuslers, and cobaltates.

can be exacerbated when multiple technologies use the same element, such as the use of In for transparent conducting oxides (TCO) and copper indium gallium selenide (CIGS) photovoltaics. Cost can also be high for relatively abundant materials where both the demand and production are low, such as low purity Si [93].

Plotting scarcity against HHI_P for thermoelectric materials is a useful tool to identify technologies where materials cost can be a concern. About half of the highest efficiency materials contain a large weight fraction of Te. (e.g. Be_2Te_3, PbTe, La_3Te_4, TAGS, Ag_9TlTe_5, SbTe, and Tl_9BiTe_6.) Given that Te has one of the highest scarcity values, these materials may pose problems for widespread deployment. Te may be rare, but the HHI_P is not critical and it does not pose a supply risk because it is produced in many countries as a byproduct of Cu. Additionally, with proper recycling and waste processing policies, Te could be recovered and reprocessed, a practice already carried out by some photovoltaic companies.

An unanticipated finding from analysis of Figure 3.8 was that incorporation of even small amounts of scarce elements in otherwise Earth-abundant compounds may be problematic. Mg_2Si has a low scarcity of $\zeta = 27$, but when doped with trace amounts of Bi to $Mg_2Si_{0.993}Bi_{0.007}$ [108], ζ increases to 1.1×10^6 because of the extremely low crustal abundance (0.025 ppm) and high atomic weight of Bi. Even 0.1% substitution of Bi on the Si site results in a four orders of magnitude increase in ζ.

A compromise between performance and resource considerations is seen in oxide materials. Cobalt oxides, such as $NaCo_2O_4$, $Ca_2Co_2O_5$, and $Ca_3Co_4O_9$, as well as the reduced ferroelectric oxide $Sr_{0.61}Ba_{0.39}Nb_2O_6$, have competitive zT values with scarcity values four orders of magnitude lower than state-of-the-art chalcogenides, two orders of magnitude lower than skutterudites (ACo_4Sb_{12}, $A =$ caged atom) and Zintls (Zn_4Sb_3, $Yb_{14}MnSb_{11}$), and one order of magnitude lower than clathrates ($Ba_8Ga_{18}Ge_{28}$) and half-Heuslers (TiNiSn). ZnO and $SrTiO_3$ are even more abundant, but have lower performance. It is worth noting that, as with Mg_2Si, if Bi is added to improve performance (e.g., $Bi_2Sr_2Co_2O_8$), a dramatic increase in ζ is observed.

Determining the Herfindahl-Hirschman Index (HHI) for all elements has shown the following elements to be most at risk for market abuse: Be, K, Br, Rb, Nb, Sb, Cs, W, the rare-earth (RE) elements including Y, and the platinum group elements (PGE): Ru, Rh, Pd, Os, Ir, Pt. These elements have HHI values of greater than 6000 in either production or reserves. As with scarcity, introduction of even small amounts of elements with high HHI_P or HHI_R such as REs, Sb, or Tl, may not be justified for a marginal gain in performance. Materials like Zintl or clathrate antimonides and rare-earth containing chalcogenides are poor outliers compared to other thermoelectric materials in terms of HHI_P risk.

The importance of HHI when considering thermoelectric materials can be illustrated through recent price spikes in antimony. In 2011, a single country that was responsible for nearly 90% of Sb mining halted much of its production. As a result, Sb prices rose over 15% in less than a year. While Sb is particularly concentrated, over 70% of elements exceed the 2500 threshold to be considered "highly concentrated" according to Federal Trade Commission definition. This makes many thermoelectric materials sensitive to changing market conditions. This analysis signals that emphasis should be placed on developing materials with a lower HHI. Examples of materials that have reasonable performance and low HHI include S- and Se-containing chalcogenides, the half-Heusler materials low in Hf- and Nb-content, and sodium cobalt oxides. Practical consideration of these criticality parameters, although not performance related, would benefit both material and experimental design.

3.5 Future directions

Thermoelectric data mining provides insight, and allows rational material design. There are, in addition to the properties described, a number of additional material properties and parameters that were not included, but that are nevertheless highly desired in comparing different thermoelectric materials. For example, crystallographic data would allow for the calculation of average atomic volume, unit cell volume, and number of atoms in the unit cell. This could be valuable in looking at changes in thermal conductivity. Mechanical properties, coefficients of thermal expansion, and high temperature stability indices would be valuable in thermoelectric device design. Furthermore, additional non-performance related parameters such as toxicity are of great interest in environmental and life-cycle analyses of thermoelectric components. Some of these properties could be extracted from other databases, measured, or approximated. Other properties, such as toxicity, are fundamentally more challenging to obtain. A comprehensive approach to comparing toxicity across compounds is not well established, since it depends on environmental transformations and persistence, exposure route, form (*e.g.*, oxidation state, presence of counter-ions), and many other factors. Finally, adding a dimension of time to the plots we have shown may increase their utility. For example, looking at the evolution of HHI over time may provide a better ability to estimate risk and market volatility of particular materials.

The data-driven approach and visualization can be readily extended to other functional materials. For example, photovoltaics, thermal barrier coatings, dielectrics, fuel cells, transparent conducting oxides, gas turbine superalloys, and batteries are all areas of research where progress depends on optimizing several competing requirements concurrently, and could benefit from a comprehensive, data-driven approach.

3.6 Closing remarks

The framework demonstrated here allows researchers to obtain a birds-eye view of a large domain of thermoelectrics research, and compare new materials of interest. The thermoelectric design space is large, and this overview of the field, including important non-performance related parameters, allows researchers to focus on property regions and material families best suited for a given application. In the case of power generation with thermoelectrics, analysis of HHI, scarcity, and materials properties can be done visually. Using the methods shown here, we highlight several families of materials that combine good performance-related properties with non-critical resource availability: highly conductive (electrically) early transition metal oxides, silicides with low bismuth content, and half-Heuslers. We also observe that all high-zT materials are found in the metallic conduction region $0.001\,\Omega\,\mathrm{cm}$ to $0.01\,\Omega\,\mathrm{cm}$. This visualization framework is also valuable from a design perspective, where it serves as a useful guide to identifying promising new materials.

Chapter 4

Thermal conductivity considerations and limits on thermoelectric performance

---

[1] A version of this chapter has been published, and is reproduced with permission from: Michael W. Gaultois and Taylor D. Sparks. How much improvement in thermoelectric performance can come from reducing thermal conductivity? *Appl. Phys. Lett.*, 104:113906 (4pp), 2014. [**doi**] © 2015, American Institute of Physics.

Large improvements in the performance of thermoelectric materials have come from designing materials with reduced thermal conductivity. Yet as the thermal conductivity of some materials now approaches their amorphous limit, it is unclear if microstructure engineering can further improve thermoelectric performance in these cases. In this contribution, we use large data sets to examine 300 compositions in 11 families of thermoelectric materials and present a type of plot that quickly reveals the maximum possible zT that can be achieved by reducing the thermal conductivity. This plot allows researchers to quickly distinguish materials where the thermal conductivity has been optimized from those where improvement can be made. Moreover, through these large data sets we examine structure-property relationships to identify methods that decrease thermal conductivity and improve thermoelectric performance. We validate, with the data, that increasing (i) the volume of a unit cell and/or (ii) the the number of atoms in the unit cell decreases the thermal conductivity of many classes of materials, without changing the electrical resistivity.

4.1 Introduction

Thermoelectric materials offer the promise of solid state refrigeration and generating electricity from waste heat sources. This great potential of thermoelectric materials has led to vigorous research, with large improvements in performance over the past two decades through the deliberate design of materials with low thermal conductivity [6, 24]. Reducing the thermal conductivity improves the thermoelectric figure of merit of a material $zT = (S^2/\rho\kappa)T$, where S is the Seebeck coefficient, ρ is the electrical resistivity, κ is the thermal conductivity, and T is the temperature. The effect is even more pronounced at a systems level–rather than a materials level–in a working device; decreasing κ makes for better matching of electrical and thermal impedance in a thermoelectric device, which improves device efficiency more than would be expected from increasing zT alone [202].

It is obvious that lower thermal conductivity will increase the performance of a material, but it remains unclear to what extent this can be done, particularly for materials that have already undergone extensive microstructural engineering. For example, the recent hierarchical approach to reducing thermal conductivity by introducing features that scatter phonons on many length scales has led to the highest reported zT values to date [4]. However, with thermal conductivity of these materials now approaching the amorphous limit of $\kappa \approx 0.25\,\mathrm{W\,m^{-1}\,K^{-1}}$ [203, 204], it is unclear how much further optimization is possible via reduction of thermal conductivity. In this report, we introduce a visualization tool to identify which materials are nearly optimized and which materials have room for improvement.

Two approaches have been very successful at reducing the thermal conductivity of materials: (1) creating microstructures with features on the order of phonon mean free path lengths to increase Rayleigh scattering [24, 4], and (2) creating disorder in the crystal structure unit cell through rattling atoms, vacancies, atomic alloying, interstitial sites, and crystallographic shear [6, 23].

There are also simple structural features that influence material properties. The decrease in thermal conductivity with increasing unit cell volume and number of atoms per unit cell has been previously suggested in specific systems [23], and the large dataset used in the present contribution confirms this behaviour is general across many materials. This work builds on a previously established open-access database of physical properties by incorporating structural information from crystal structures reported in the Inorganic Crystal Structure Database (ICSD). This database and the plots generated in the current report are accessible through an interactive, online framework for exploring thermoelectric materials: the MRL thermoelectrics datamining project (`www.mrl.ucsb.edu:8080/datamine/thermoelectric.jsp`) [205].

4.2 Experimental details

Physical properties were manually extracted from previous reports in the literature. This process, and references for the 300 compounds examined in this report, are described in a previous contribution [205]. Structural data, such as the unit cell volume and number of atoms in the unit cell, were taken directly from the ICSD or calculated from the reported data. The electronic contribution to the thermal conductivity (κ_e) was calculated through the Wiedemann–Franz law using the Lorenz number, L. The Lorenz number is not known for all materials, so L was set to the Sommerfeld value of $L_0 = 2.44 \times 10^{-8}\,\mathrm{W\,\Omega\,K^{-2}}$. This approximation is valid for most metals and degenerate semiconductors [23]. The error introduced by this approximation is no more than 50% when verified against materials in the database with known Lorenz numbers. This potential error is small compared to the trends that span several orders of magnitude featured in this report. The Wiedemann–Franz law holds for any system where both electrical and heat transport are due to non-interacting free electrons that are elastically scattered by impurities and/or lattice vibrations. This condition is generally satisfied for metallic band conductors with a long screening length [206].

4.3 Results and Discussion

4.3.1 Maximum achievable zT

$$\sigma = \frac{\kappa_e}{LT} \tag{4.1}$$

$$zT = \frac{S^2}{\kappa}\left(\frac{\kappa_e}{LT}\right)T \tag{4.2}$$

$$zT = \frac{S^2}{L}\left(\frac{\kappa_e}{\kappa}\right) \tag{4.3}$$

To determine the maximum zT of a material, the Wiedemann–Franz law (Eq. 4.1) can be combined with the expression for zT to yield Eq. 4.2. In this formalism, the *maximum* achievable zT occurs at the limit where thermal conductivity is due only to heat transport via electronic carriers (*i.e.* $\kappa_e/\kappa_{\text{total}} = 1$) and depends only on the Seebeck coefficient [207]. The *actual* zT also depends on the fraction of the total thermal conductivity due to electronic transport, $\kappa_e/\kappa_{\text{total}}$ (Eq. 4.3) which is less than 1 for most materials. Intuitively, high thermoelectric performance will be achieved when the lattice thermal conductivity (κ_{lattice}) is small. Further, this method profits by not considering the theoretical minimum thermal conductivity κ_{min} [204, 203], which has been violated in the past [208].

The relationship in Eq. 4.3 is useful to determine the potential of existing thermoelectric materials, as well as how much improvement can arise from further decreases in thermal conductivity. Because the maximum achievable zT depends only on the Seebeck coefficient, an upper bound for existing thermoelectric materials can be defined. Examining a plot of the Seebeck coefficient vs $\kappa_e/\kappa_{\text{total}}$ reveals the max possible zT of a material and how much improvement in performance can be obtained from reducing κ_{lattice} (Figure 4.1). For example, chalcogenides have been extensively studied and tremendous

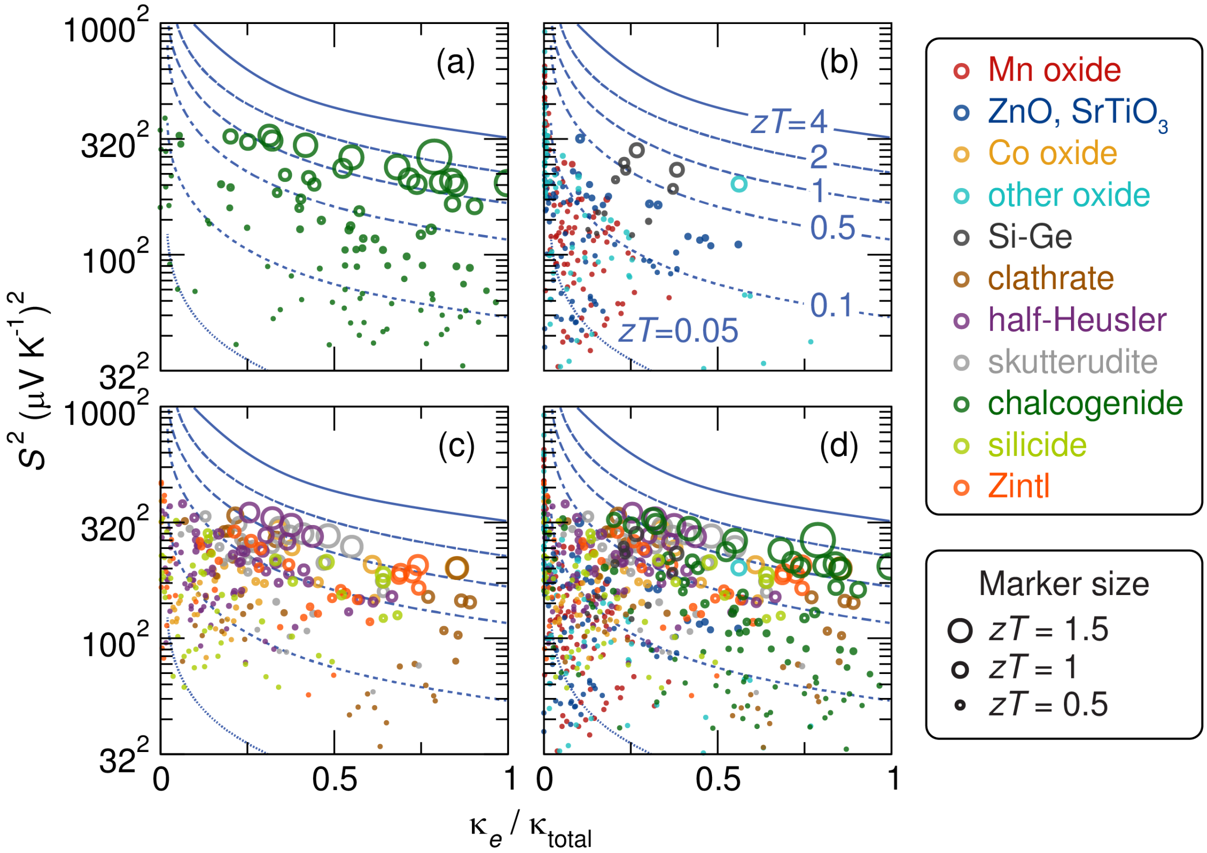

Figure 4.1: Fractional kappa plots of ∼300 thermoelectric materials (a–d). Plotting the Seebeck coefficient vs the fraction of thermal conductivity from electrons ($\kappa_e/\kappa_{\text{total}}$) is an effective way to evaluate how much improvement is possible by reducing the lattice thermal conductivity κ_{lattice}. The marker size (radius) is proportional to the zT, and contour lines represent lines of constant zT. The max possible zT is determined by the Seebeck coefficient, obtained when $\kappa_{\text{lattice}} \ll \kappa_{\text{total}}$ (*i.e.*, $\kappa_e/\kappa_{\text{total}} \approx 1$). Some materials, including select chalcogenides members (a), approach the limit where κ_{lattice} is negligible, whereas other materials such as oxides and SiGe (b), or half-Heuslers and skutterudites (c), could be further engineered to reduce κ_{lattice} and improve thermoelectric performance. A composite of all material families is shown in (d).

effort has been made to improve their performance through band engineering [102] and microstructural engineering [4]. Importantly, examining the aforementioned plot in Figure 4.1 reveals that many chalcogenide thermoelectric materials are reaching the maximum zT attainable by reduction of the thermal conductivity (i.e. when $\kappa_e/\kappa_{\text{total}} = 1$ in Figure 4.1(a)). Future gains in these systems will need to come from increasing the Seebeck coefficient, for example, by band structure engineering [102] and dimensional confinement [83].

Microstructural engineering is still a viable option for most thermoelectric materials. Unlike the chalcogenides, thermal conductivity in most thermoelectric materials is dominated by κ_{lattice}; most materials lie towards the left of the fractional kappa plot (Figure 4.1). For example, Si and SiGe have the requisite electrical properties and have been extensively studied, though there is room for further reduction of κ_{lattice} if new approaches are identified. One notable exception is the family of clathrates, which exhibit an exceptionally low contribution from κ_{lattice} (Figure 4.1(c)). The rattling atoms in clathrate materials are effective at scattering phonons, and lead to this exceptional behaviour [209]. Comparatively, skutterudite materials also have rattling atoms [210], yet their place in the fractional kappa plot suggests they remain good targets for microstructural engineering (Figure 4.1(c)).

4.3.2 Structure-property relationships

Material properties depend on the crystal structure, which can often be rationally modified using fundamental principles, such as knowledge of the ionic radii and the balance of formal charge. Consequently, understanding structure-property relationships is important to design high-performance materials. Accordingly, we have expanded the open-access MRL thermoelectrics database by including reported structural information

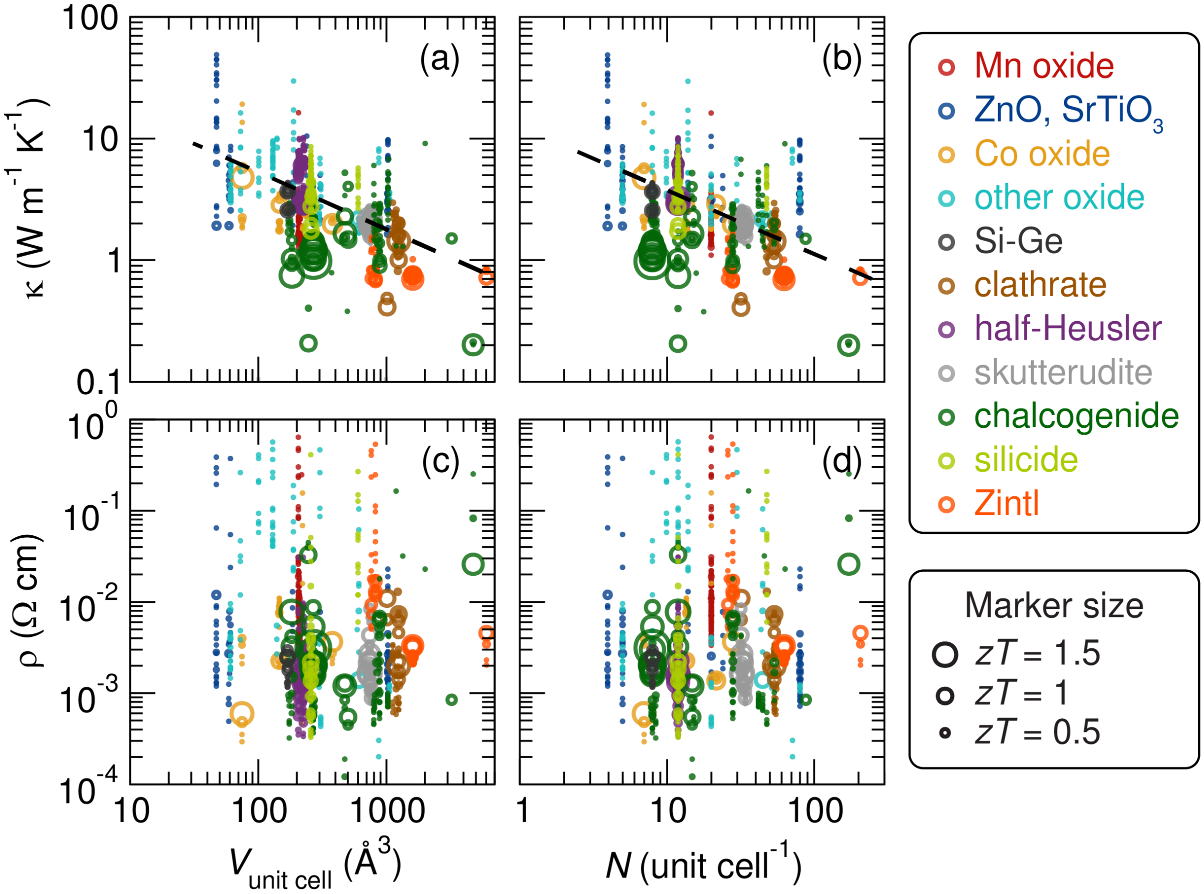

Figure 4.2: The thermal conductivity of thermoelectric materials generally decreases with increasing unit cell volume V (a) and number of atoms in the unit cell N (b). Meanwhile, the electrical resistivity of thermoelectric materials is largely unaffected (c–d). Each data point represents a specific compound at a temperature of interest (300 K, 400 K, 700 K, or 1000 K), and the marker size (radius) is proportional to the zT. Lines of best fit are shown as a guide to the eye.

available from the ICSD. The structural information is used here to validate how electrical resistivity and thermal conductivity of thermoelectric materials are correlated with two intuitive structural parameters: (i) the volume of the unit cell, and (ii) the number of atoms in the unit cell. In both cases, the structural parameters are correlated with thermal conductivity, while the electrical resistivity is invariant (Figure 4.2). These relationships between structure and thermal conductivity have been explained by theory [211, 23] and have been previously examined in a limited number of phases [6]. The results of datamining, presented here, demonstrate these trends can be generalized across many material families and structures.

The contrasting behaviour between electronic and thermal transport is likely due to differences in relevant length scales for appropriate carriers (*i.e.*, electrons or phonons). Electronic transport of electrons and/or holes is sensitive to changes in local structure, whereas phonons tend to have longer mean free path lengths and are thus disproportionately influenced by changes involving lattice periodicity, which is generally on a length scale larger than the size of atomic clusters. Accordingly, changes in the number of atoms per unit cell and/or the unit cell volume show a larger influence on thermal transport than electrical transport.

Though there are numerous subtleties involved in correlations between thermal conductivity and structural details, several important factors have been previously identified. For example, the strong reduction in thermal conductivity with increasing number of atoms per unit cell is likely due to a reduction in the fraction of acoustic phonon modes. For a system with N atoms per unit cell, the fraction of acoustic modes is proportional to $1/N$; optical phonon modes are dominant in crystal structures with a large number of atoms per unit cell [211]. Optical modes tend to have slower group velocity than acoustic modes leading to slower thermal transport, and thus lower κ_{lattice} [23]. The dependence on unit cell volume is likely related to both complexity as well as an increasing number of atoms per unit cell, as originally described by Slack [212] and later validated systematically by others in a small subset of materials, Zintl antimonides [213].

4.4 Conclusion

Improving the performance of thermoelectric materials is an active field of research, and microstructural engineering has led to large gains in performance by reducing the lattice thermal conductivity (κ_{lattice}). However, there is a limit to the extent performance can be improved by these means; fractional kappa plots and $\kappa_e/\kappa_{\text{total}}$ are useful screening tools to evaluate potential improvement of material performance via microstructural engineering. Some materials, like particular chalcogenides and clathrates, are approaching the point where κ_{lattice} is negligible ($\kappa_e/\kappa_{\text{total}} \sim 1$), so these materials may not experience significant gains in performance from further microstructural engineering. In these materials, the focus should be to optimize the electronic structure.

In contrast, κ_{lattice} remains the dominant contribution to thermal transport and is the performance-limiting attribute in many thermoelectric materials. Although we encourage readers to explore the online database interactively, we highlight three materials made from moderately abundant precursors, with promising electrical transport, and clear routes to reduce κ_{lattice}. Half-Heuslers, such as TiNiSn, can be alloyed with site defects and semi-coherent full-Heusler secondary phase inclusions [214]. Other promising materials feature superlattices, secondary phase inclusions, and large number of atoms. Magnéli phases with crystallographic shear, such as WO_{3-x} [215], show promising preliminary results, though our fractional kappa plots reveal the Seebeck coefficient will need to be improved to achieve $zT > 0.5$. In niobates and tetragonal bronzes, such as $Sr_{1-x}Ba_xNb_2O_6$, point defects can be tuned with the composition and oxidation state of the metal ions [163]. Despite considerable work to reduce the thermal conductivity of thermoelectric materials, there are many opportunities left for improvement.

Chapter 5

Rapid SPS preparation and physical property measurement of WO_3-containing complex oxides

---

[1] A version of this chapter has been published, and is reproduced with permission from: Michael W. Gaultois, Moureen C. Kemei, Jaye K. Harada and Ram Seshadri. Rapid preparation and magnetodielectric properties of trirutile Cr_2WO_6. *J. Appl. Phys.* 117:014105 (6pp), 2015. [**doi**] © 2015, American Institute of Physics.

Dense pellets of $>99\%$ purity trirutile Cr_2WO_6 were prepared in one step from starting oxides using spark plasma sintering, leading to simultaneous reaction and consolidation in 3 min at 1473 K. The reducing environment during processing may be partly responsible for the rapid reaction time in these oxides, with partial reduction of Cr^{3+} and the associated oxygen vacancies allowing rapid diffusion of cations. The low-temperature physical properties of Cr_2WO_6 were examined, and a new transition at $T = 5.9\,K$ was observed as an anomaly in the temperature-dependent dielectric permittivity and a corresponding anomaly in the specific heat. A strong enhancement of the magnetocapacitance is observed below this transition temperature at $T = 5.9\,K$, and may be associated with a change from collinear spin order to more complex spin order.

5.1 Introduction

The preparation of complex oxides with multiple metal ions frequently involves cycles of intimate grinding of the starting oxide powders and annealing at high temperatures in a process that can take multiple days. The long heating times are a consequence of the slow rate of solid-state diffusion for most ions in oxide environments. This is particularly true in the case of Cr_2WO_6 [216, 217] — the compound of interest here — as Cr_2O_3 is quite inert and diffuses rather slowly, a property that is responsible for its protective properties as one of the primary protective oxides in engineering materials, such as steels. There are frequently other complications as well. Notably for this material class, WO_3 is a volatile solid, making it challenging to obtain single-phase materials using the extended reaction times required to enable Cr^{3+} mobility. Moreover, the resulting materials after traditional solid state reaction are powders or low density sintered bodies that require consolidation and/or densification to achieve dense bodies suitable for physical property measurement. This can be accomplished by hot-pressing at elevated temperatures

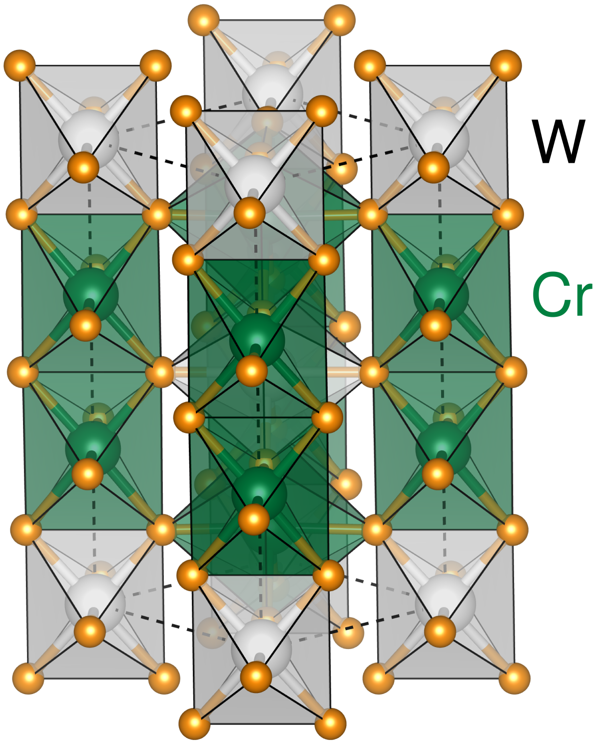

Figure 5.1: Cr_2WO_6 adopts the inverse trirutile structure ($P4_2/mnm$, 136), which consists of parallel columns of edge-sharing MO_6 ($M =$ Cr, W) octahedra extending along the c-axis. Cr^{3+} atoms are shown in green, and W^{6+} in white. These columns are connected through O at the corners of the edge-sharing octahedra.

for extended times (generally several hours), though this introduces further challenges, including the potential for decomposition, or, in this case, volatilization.

This contribution describes the use of spark plasma sintering (SPS), more accurately described as current-assisted, pressure-activated densification (CAPAD) [30], to rapidly prepare multi-gram quantities of high purity, dense samples of Cr_2WO_6 in a single processing step that takes less than an hour. The rapid processing times and simultaneous reaction and consolidation overcome many of the common pitfalls of traditional ceramic methods. Further, we describe how the rapid reaction times allowed by this processing ($<$3 min at 1473 K for Cr_2WO_6) may be related to fundamental rates of well-understood models of ligand exchange in aqueous molecular metal complexes.

Cr_2WO_6 was prepared and studied here as a candidate magnetodielectric material. Cr_2WO_6 adopts an inverse trirutile-type crystal structure (Figure 5.1), and was proposed to have potential magnetodielectric properties by Hornreich [218], and more recent work has investigated the magnetoelectric coupling in Cr_2WO_6 near the antiferromagnetic ordering temperature at $\sim$45 K [219]. The coupling of magnetic and electric properties is of great interest for next generation information storage, where an electric field may control and interrogate the magnetic state of a memory storage device. Complete characterization of mangetodielectric materials is imperative to understand the complex interaction of magnetism and dielectric polarization. This report presents the low-temperature physical properties of Cr_2WO_6, and reveals a new transition at $T = 5.9$ K observed by changes in the dielectric permittivity and specific heat. This is keeping with other recent studies that have revealed dielectric permittivity and magnetocapacitance measurements are sensitive probes of subtle changes in magnetic/crystal structure accompanying magnetic ordering, as well as changes in magnetic symmetry [220, 221].

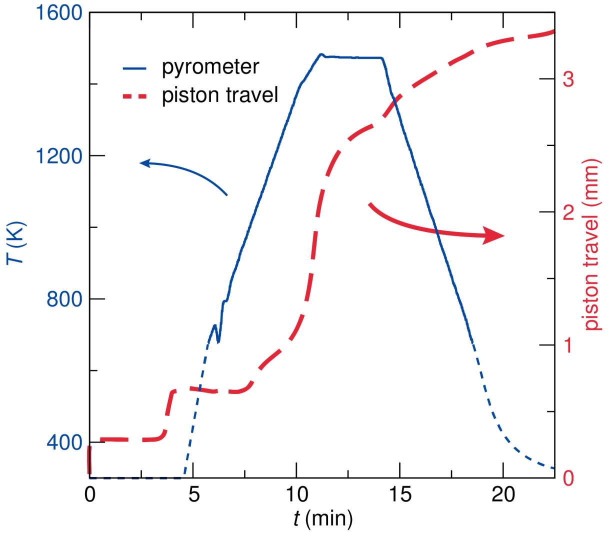

Figure 5.2: SPS can be used to prepare dense pellets of Cr_2WO_6 from a mixture of binary oxides ($Cr_2O_3 + WO_3$) in under 30 min total. 80 MPa of uniaxial pressure was applied and the sample was heated rapidly from 673 K to 1473 K at 200 K/min, annealed for 3 min at 1473 K, then rapidly cooled at 200 K/min. The temperature profile below 673 K is estimated, as the pyrometer is unreliable below 673 K.

5.2 Experimental details

Polycrystalline samples were made by reaction and consolidation of binary oxide powders (WO_3, 99.9%, Sigma-Aldrich; Cr_2O_3, 99.99%, Sigma-Aldrich) using spark plasma sintering on an instrument from FCT Systeme GmbH, Germany. In a chamber base pressure of 10 torr of argon, 80 MPa uniaxial pressure was applied using a 9 mm inner-diameter graphite die (EDM-4, POCO graphite). The sample was then heated rapidly to 1473 K at 200 K/min, annealed for 3 min at 1473 K, then rapidly cooled at 200 K/min (Figure 5.2). During the SPS annealing step, 5.0 V and 980 A were applied across the die set. X-ray diffraction (XRD) was performed on the pellet using a laboratory instrument (Philips X'Pert diffractometer, Cu Kα radiation), and diffractograms were consistent with single-phase Cr_2WO_6; no secondary phases were observed. When ground, the resulting Cr_2WO_6 powder is brown in colour. The conditions in SPS processing are highly reducing (elevated temperatures in a graphite die in low pressures of argon), so pellets were subsequently annealed in air to ensure full oxygen stoichiometry and minimize defects. Pellets were annealed in air at 1273 K for 24 hours and cooled to room temperature at 2 K/min. Reaction with Al_2O_3 or SiO_2 is problematic, so pellets were annealed on a bed of sacrificial Cr_2WO_6 powder. Annealed pellets had a density of 6.74 g/cm^3 to 6.77 g/cm^3 (99% single crystal density), measured by He pycnometry using a MicroMeritics AccuPyc 1340 Pycnometer. Annealed material was used for all experimental measurements reported here; synchrotron XRD of annealed material revealed a 0.7(1) mol% Cr_2O_3 impurity that was not observed by lab XRD because of the lower sensitivity of the lab instrument.

High-resolution synchrotron XRD data on finely-ground powder was acquired at 295 K at beamline 11-BM at the Advanced Photon Source, Argonne National Laboratory, using an average wavelength of 0.413682 Å on a diffractometer that has been described in detail by Wang *et al.* [43]. The precise wavelength was determined using a mixture of Si (SRM 640c) and Al_2O_3 (SRM 676) NIST standards run in a separate measurement. Samples were contained in 0.8 mm diameter Kapton capillaries and the packing density was low enough that absorption was not noticeable. Rietveld refinement was performed using TOPAS 5 Academic [222] and verified using GSAS-II [223]. Instrument profile parameters were determined using Si (SRM 640c) and LaB_6 (SRM 660b) NIST lineshape standards, run in separate measurements. The refined lattice parameters of Cr_2WO_6 were $a = 4.579269(4)$ Å and $c = 8.66328(9)$ Å.

Magnetic properties of powders were measured using a Quantum Design Dynacool vibrating sample magnetometer (VSM). Zero-field cooled (ZFC) and field cooled cooling (FCC) measurements were performed between 2 K and 380 K with 1000 Oe applied dc magnetic field. ZFC–FCC data was collected while heating (ZFC) or cooling (FCC) at 1 K/min, while the field-dependent susceptibility was collected while sweeping the magnetic field at 100 Oe/sec. Low-temperature heat capacity was measured using a Quantum Design Physical Properties Measurement System (PPMS). Heat capacity measurements were performed on a pellet of mass 32.72 mg cut from the SPS-densified material and analyzed using the thermal relaxation dual-slope method. A thin layer of Apiezon N grease ensured thermal contact between the platform and the sample. The heat capacity of the Apiezon N grease was collected separately and subtracted from the measured sample heat capacity.

Dielectric properties were measured by an Andeen-Hagerling AH2700A capacitance bridge connected to the sample by shielded coaxial cables. A dense cylindrical sample (9.57 mm diameter, 1.41 mm thick, 99% apparent density) was placed in a Quantum Design Dynacool PPMS, which provides control of the temperature and field when carrying out dielectric measurements. To confirm the minor Cr_2O_3 impurity (0.7 mol%) did not influence the capacitance, additional measurements were conducted on a single-phase Cr_2O_3 pellet (prepared by the same process conditions described above), and these measurements confirm the lack of similar features in the temperature- and field-dependent capacitance.

5.3 Results and Discussion

5.3.1 Rapid preparation of single-phase material

SPS offers a rapid preparatory route to prepare dense, single-phase material in a single processing step that takes ∼30 min total (including cool-down). SPS led to dense pellets of Cr_2WO_6 with >99% phase purity (Figure 5.3). We have previously observed that extremely high pellet densities are essential for high quality dielectric data. Reaction times to achieve phase-pure materials were as short as 3 minutes at the reaction temperature (1473 K), the shortest time attempted (Figure 5.2). Solid state reactions generally take several days, and the reaction rates are generally limited by diffusion. Although no

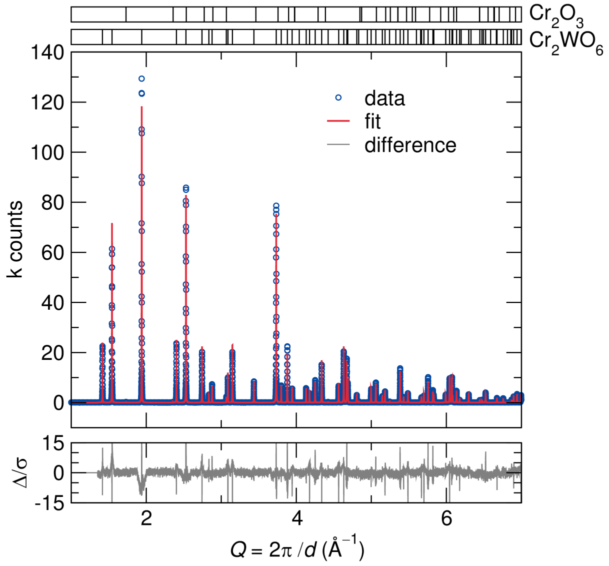

Figure 5.3: Rietveld analysis of synchrotron powder X-ray diffraction data reveals this particular sample contains 99.3(1) mol% Cr_2WO_6, with a 0.7(1) mol% Cr_2O_3 secondary phase, though this minor impurity does not affect the bulk properties in this report. This sample was prepared using SPS from a mixture of binary oxides ($Cr_2O_3 + WO_3$) in 3 minutes at 1473 K.

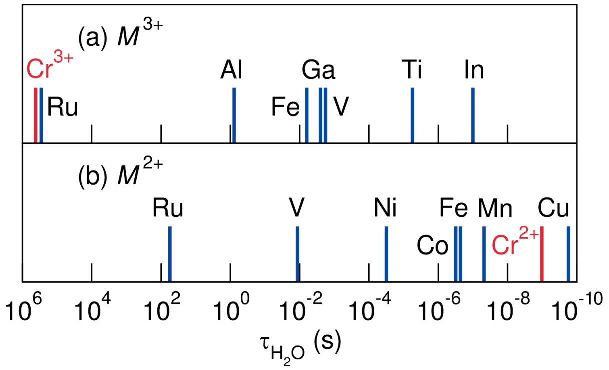

Figure 5.4: The mean residence time of water molecules in metal hexaaqua complexes may be a useful proxy to understand solid state reactions of oxides. Inert cations, such as Cr^{3+}, lie on the left, while reactive cations with labile ligands lie towards the right, such as Cr^{2+}. While ions of lower charge/radius ratio are expected to react more quickly (for example, the series of Al^{3+}, Ga^{3+}, and In^{3+}), the crystal field stabilization energy dominates the reactivity of transition metal ions. The reducing conditions in SPS processing may lead to partial reduction of Cr^{3+} and creation of oxygen vacancies, and may explain the unexpectedly rapid reaction times possible with SPS (<3 min). Data from [[224]].

hard rule set exists to determine the reaction rate of solid metal oxides, we propose the extensive studies of molecular metal aqua complexes may provide useful guidelines.

Cr^{3+} (d^3) is notoriously inert due to the large crystal field stabilization energy provided by a half-filled t_{2g}^3 level in an octahedral coordination geometry (Figure 5.4) [224]. This leads to a stable coordination shell with an extremely long mean residence time of water molecules in the $[Cr(H_2O)_6]^{3+}$ complexes (∼5 days), compared to the blindingly fast residence time in Cr^{2+} hexaaqua complexes ($\sim 10^{-9}$ seconds). In solid Cr oxides, the CrO_6 octahedral coordination shell is expected to be inert, and lead to slow diffusion of Cr^{3+} cations. The unexpectedly short reaction times for Cr_2WO_6 using SPS may result from partial reduction of Cr^{3+} and oxygen vacancies created by the reducing conditions during SPS processing. Creation of Cr^{2+} would lead to much more labile oxide anions, and disordered oxygen vacancies would be expected to decrease the activation energy barrier associated with interstitial or vacancy hopping diffusion of Cr species, thus increasing the rate of diffusion and decreasing the reaction time between powdered metal oxide precursors.

The reducing conditions during SPS undoubtedly lead to partial reduction of WO_3, though this alone is insufficient to lead to the rapid reaction times reported here. Attempts to produce pseudobinary Al_2O_3–WO_3 phases under similar SPS conditions resulted in only minor product formation and the recovery of starting materials, as determined by lab XRD. This is consistent with our suggested model, as Al^{3+} is expected to be much more inert than Cr^{2+} (Figure 5.4; $\tau_{Al^{3+}} \approx 10^9 \tau_{Cr^{2+}}$), and Al^{3+} is not expected to reduce as easily as Cr^{3+} ($Cr^{3+} + e^- \leftrightarrow Cr^{2+}$, $E^\circ = -0.4\,V$; $Al^{3+} + 3e^- \leftrightarrow Al$, $E^\circ = -1.7\,V$) [101].

Because of the reduction during SPS processing, thin pellets (thickness ∼1 mm) were annealed to ensure full oxygen stoichiometry before measuring physical properties. Annealing of powders or pellets resulted in no statistically significant change in lattice

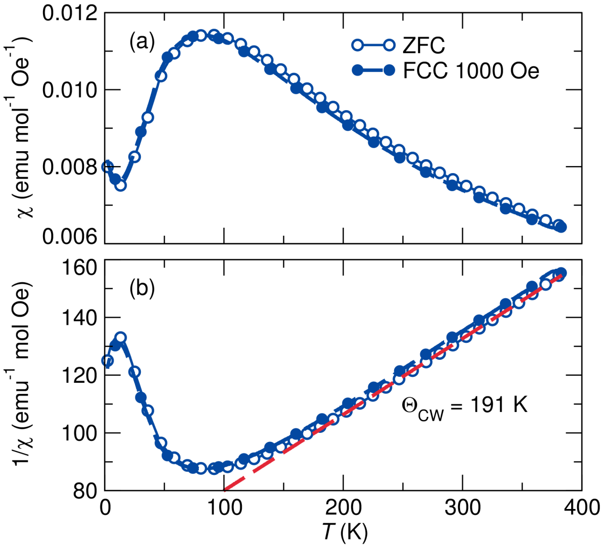

Figure 5.5: (a) Magnetic susceptibility and (b) inverse susceptibility of Cr_2WO_6 (acquired at ∼0.1 K intervals). A Curie-Weiss fit to the ZFC magnetic susceptibility from 300 K to 370 K leads to a $\Theta_{CW} = -191$ K. There is a slight offset between the ZFC and FCC curves at high temperature, likely due to a temperature lag.

parameter detectable by laboratory XRD, and the appearance of the annealed powder is brown, and indistinguishable from samples before annealing. Further, the effective moment extracted from the bulk magnetic susceptibility agrees with the calculated spin-only value for Cr_2WO_6 (see below), suggesting there are no extra spins that might be present due to partially reduced metal centres. Annealed material was used for all experimental measurements reported here.

5.3.2 Magnetic and electrical properties

Complex magnetic interactions arise in the trirutile-type structures because of the unique connectivity in the crystal structure: parallel columns of edge-sharing MO_6 ($M =$ Cr, W) octahedra extending along the c-axis (Figure 5.1). Systematic studies performed by Yamaguchi and Ishikawa have examined the nature of the magnetic phenomena associated with several members of this structural family, including Cr_2WO_6 [225]. Low-

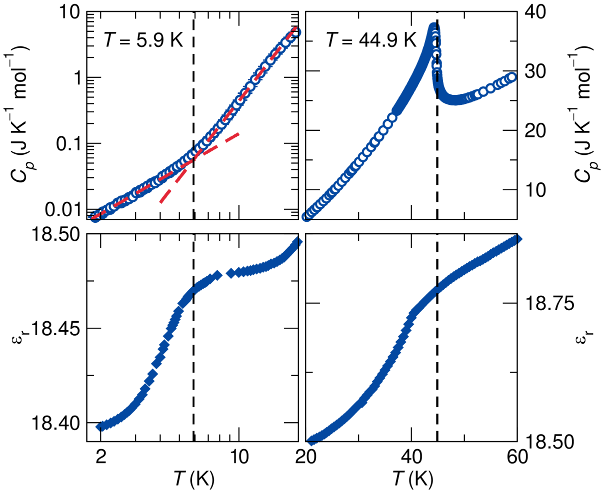

Figure 5.6: Two transitions are observed by specific heat and dielectric permittivity as the temperature is decreased. The onset of the sharp change in the dielectric permittivity at $T \approx 6$ K corresponds to a change in slope of the log-log specific heat.

dimensional, short-range antiferromagnetic correlations give rise to a broad maximum in the magnetic susceptibility [(Figure 5.5(a)], which Yamaguchi and Ishikawa quantitatively describe using an anisotropic 2D Heisenberg model [225]. Long-range 3D antiferromagnetic order takes place at $T_N \approx 45$ K [217], which is more easily seen in the heat capacity (Figure 5.6).

The higher-temperature region (300 K to 370 K) of the ZFC inverse susceptibility was fit to the Curie–Weiss (CW) equation, $\chi = C/(T - \Theta_{CW})$ to extract a Weiss temperature of Θ_{CW} = -191 K [Figure 5.5(b)], which is consistent with previous reports of −189 K [225]. An effective moment of $\mu_{eff} = 5.44\,\mu_B$ per Cr_2WO_6 formula unit was extracted using the relationship $\mu_{eff}^2 = 3Ck_B/N$, where C is the Curie constant from the CW equation. The μ_{eff} is close to the calculated spin-only value of $\mu_S = 5.48\,\mu_B$, and significantly less than the calculated unquenched μ_{L+S} of 7.35 μ_B. Finally, the large negative Weiss temperature is much larger than the antiferromagnetic ordering temperature, which is characteristic of frustrated spin systems. Moderately frustrated systems tend to have a frustration index $f \geq 3$ [58], a criterion that is satisfied for Cr_2WO_6, where $f = 4.3$.

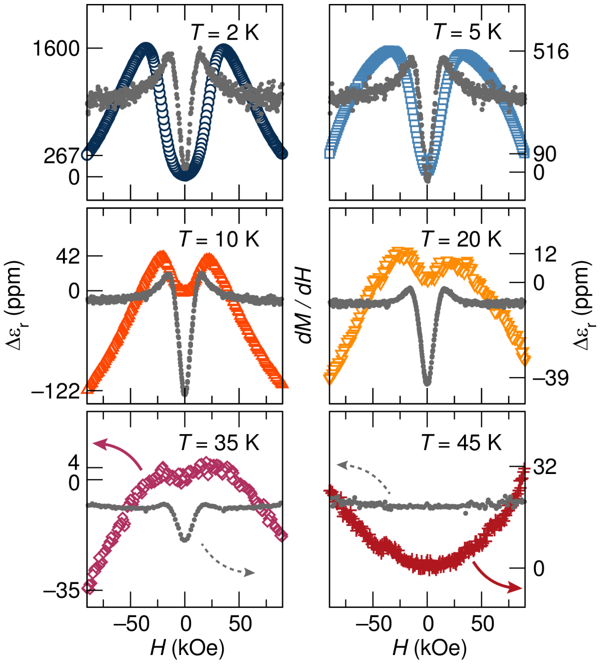

Figure 5.7: Magnetocapacitance measurements show 3 temperature regimes: $T > 45\,\mathrm{K}$, $6\,\mathrm{K} < T < 45\,\mathrm{K}$, and $T < 6\,\mathrm{K}$. The magnetodielectric response changes upon magnetic ordering at $T_\mathrm{N} \approx 45\,\mathrm{K}$, and is strongly enhanced upon the lower-temperature transition at $T \approx 6\,\mathrm{K}$. Compared to the magnetocapacitance at 35 K, the response at 2 K is enhanced by a factor of 400. Corresponding regimes are seen in the field-dependent magnetization, whose derivative is shown above (grey).

Measuring the dielectric permittivity down to 2 K reveals a feature at $T_\mathrm{N} \approx 45\,\mathrm{K}$ due to a known antiferromagnetic ordering transition, as well as a feature at $T \approx 6\,\mathrm{K}$. Corresponding features in the specific heat are observed for both features, with a sharp λ-type anomaly at $T_\mathrm{N} = 44.9\,\mathrm{K}$, and a change in slope of the log-log specific heat at $T = 5.9\,\mathrm{K}$ (Figure 5.6). The transition temperature of $T = 5.9\,\mathrm{K}$ reported here is the intersection of linear fits to the log-log specific heat carried out on the linear regimes above and below the transition (Figure 5.6). (1.8 K to 4.0 K: $C_p = 2.54 \times 10^{-3} T^{1.74}$; 9.0 K to 16.0 K: $C_p = 5.78 \times 10^{-5} T^{3.88}$) The values of the specific heat near $T_\mathrm{N} = 44.9\,\mathrm{K}$ are consistent with a previous report from Yamaguchi *et al.* [225].

The nature of the transition at $T = 5.9\,\mathrm{K}$ was probed using field-dependent dielectric measurements in 3 key temperature regimes (Figure 5.7). Above the magnetic ordering temperature $T_{\mathrm{N}} \approx 45\,\mathrm{K}$, there is a weak, continuous increase of the dielectric permittivity with increasing applied magnetic field. Below 45 K, a local minimum in the field-dependence occurs at zero field, with weak local maxima at moderate applied fields (∼20 kOe). Finally, below 6 K, in the region where a strong change is observed in the temperature-dependent dielectric permittivity, there is a strong enhancement in the magnetocapacitance response and the maxima shift to slightly higher field strength (∼35 kOe). Compared to the magnetocapacitance at 35 K, the response at 2 K is enhanced by a factor of 400. The close correspondence of behavioural changes with known spin ordering and features in specific heat suggest these changes are intrinsic to Cr_2WO_6, and not due to extrinsic resistive magnetocapacitance through a Maxwell-Wagner mechanism involving depleted grain boundaries[226].

These regimes are analogous to behaviour seen in the field-dependent magnetization. The field-dependent magnetization is consistent with paramagnetism above $T_{\mathrm{N}} \approx 45\,\mathrm{K}$, and below the magnetic ordering temperature the magnetization shows small changes in slope at magnetic fields corresponding to the local extrema in the dielectric permittivity visible by magnetocapacitance. These changes are seen more readily in the derivative of the magnetization curves (Figure 5.7).

The sharp change in dielectric constant and strong enhancement of the magnetocapacitance below 6 K may be associated with a change from a collinear spin structure to more complex spin order, such as conical ordering [227, 228, 229, 230, 231]. Noncollinear spin ordering is common in magnetically frustrated systems, so this is not altogether unexpected here, since some frustration was noted ($f = 4.3$). Although the previous magnetic structure determination by Kunnmann *et al.* using neutron scattering at 4.2 K assigned a collinear magnetic structure [217], most of the change in the dielectric permittivity has not yet taken place by 4.2 K (Figure 5.6), and is not complete until below below 2 K. Other neutron scattering studies at 4.2 K observed extra weak reflections that could not be adequately described by a collinear spin structure, and were attributed to magnetostructural distortion, specifically, displacement of Cr ions [232]. This subtle magnetostructural distortion may be associated with changes in spin ordering, as has been demonstrated in recent reports of frustrated spinel oxides [221, 233]. More detailed high-resolution neutron scattering studies at lower temperature may confirm this change in spin ordering.

The change in spin-order and the magnetostructural distortion would both be expected to contribute to the large change in dielectric permittivity reported here, and the magnetostructural distortion may be necessary for this to occur. The undistorted crystal structure symmetry of Cr_2WO_6 ($P4_2/mnm$, 136; D_{4h}^{14}) does not allow for any noncollinear spin structures, and Dzyaloshinskii-Moriya (DM) antisymmetric exchange between nearest neighbour Cr ions is not allowed because of the inversion centre at the midpoint (Wyckoff site $2b$, symmetry $m.mm$). However, displacement of Cr ions through magnetostructural distortion will lower the symmetry of the crystal structure. This will likely break the inversion symmetry to allow for DM interactions, which may lead to canting of spins and a noncollinear spin structure, both of which would become more pronounced at lower temperature. This would lead to minimal changes to the entropy and gradual changes to the neutron diffraction but large changes to the dielectric response, as reported here.

5.4 Conclusion

Dense pellets of $>99\%$ purity trirutile Cr_2WO_6 were prepared by SPS, which led to simultaneous reaction and densification of WO_3 and Cr_2O_3 powders in 3 min at 1473 K. SPS offers a rapid route to prepare multi-gram quantities of high-purity, consolidated, dense materials that are in a suitable form for physical property measurement. The rapid processing times are ideally suited for materials that are volatile, such as WO_3. The reducing environment during processing may be partly responsible for the rapid reaction time in these oxides, where partial reduction of Cr^{3+} and creation of oxygen vacancies may allow rapid diffusion of cations.

The low-temperature physical properties of Cr_2WO_6 were examined, and a new transition at $T = 5.9\,\mathrm{K}$ was observed as an anomaly in the temperature-dependent dielectric permittivity and a corresponding anomaly in the specific heat. Below 6 K, a strong enhancement of the magnetocapacitance is observed, and may be associated with magnetostructural distortion and/or a change from collinear spin order to more complex spin order.

Chapter 6

Controlled microstructure and thermoelectric properties of reduced early transition metal oxide composites

---

[1] A version of this chapter is being submitted for publication: Michael W. Gaultois, Taylor D. Sparks, Jason E. Douglas, and Ram Seshadri. Controlled microstructure and thermoelectric properties of reduced early transition metal oxide composites.

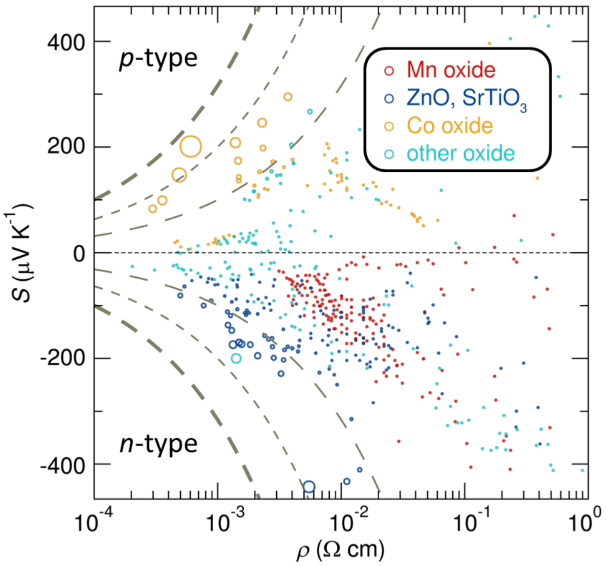

Figure 6.1: A survey plot of current oxide thermoelectric materials, where the size of the circle is proportional to the material power factor, which is the electrical component of zT, the thermoelectric figure of merit. Dashed lines of constant power factor give bounds for reasonable thermoelectric performance, and this plot reveals the lack of high-performance n-type oxide materials. Data from [205].

Reduced early transition metal oxides have been identified as interesting thermoelectric materials using a datamining approach, and 14 compositions in the Nb-rich portion of the WO_3–Nb_2O_5 phase system are explored here using spark plasma sintering (SPS) as a rapid preparation technique. The resulting composite materials contain W-rich precipitates with characteristic length scales that range from $< 20\,\mathrm{nm}$ to $\sim 2\,\mu\mathrm{m}$ within a single sample, and exhibit thermal conductivities of $\sim 2.5\,\mathrm{W\,m^{-1}\,K^{-1}}$ from 300 K to 1000 K. zT was determined for 4 compositions, and the highest-performance composition in this report reaches $zT = 0.1$ at 950 K, the highest temperature measured using our instrumentation.

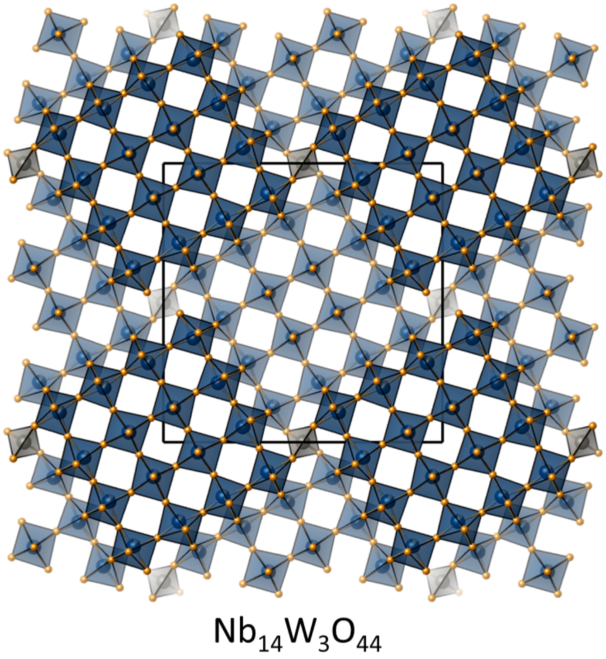

Figure 6.2: WO_3–Nb_2O_5 phases tend to form complex tetragonal tungsten bronze structures, which feature 3-dimensional slabs of corner-sharing NbO_6 octahedra connected by WO_4 tetrahedra. $Nb_{14}W_3O_44$ is one such example of many possible homologues; the size of the slabs can be changed with Nb/W composition. The high polyhedral connectivity is important for good electrical transport, while the intrinsic structural defects (such as the crystallographic shear planes and Nb/W site substitution) are important for low thermal transport.

6.1 Introduction

The promise of solid-state energy conversion and the recovery of energy from waste heat has led to vigorous research on thermoelectric materials. However, widespread deployment of thermoelectric modules on Earth has been limited by the low efficiency, low crustal abundance, and poor thermal stability of existing materials. Researchers have sought to develop oxide materials to address these problems, but limited high-performance *n*-type materials have been discovered (Figure 6.1). A recent datamining study has identified early transition metal oxides as thermoelectric materials of interest due to their low electrical resistivity [205].

WO_3–Nb_2O_5 phases tend to form complex tetragonal tungsten bronze structures, which feature 3-dimensional slabs of corner-sharing NbO_6 octahedra connected by WO_4 tetrahedra [234]. Nb_2O_5 has many polymorphs, but the dominant room-temperature phase is monoclinic, and is a layered structure with large voids and distorted and irregular Nb polyhedra [235]. This poor structural connectivity is not ideal for low electrical resistivity and electrical doping. However, the WO_3–Nb_2O_5 phases can be doped to have low electrical resistivity, which happens in part because of the highly connected structure in 3-dimensions. Highly connected structures also tend to have high thermal conductivity, which is avoided in the tungsten bronze structure-types because of the complex structure, which has intrinsic defects introduced by W–Nb substitution, oxygen deficiency, and crystallographic shear (Figure 6.2). These phenomena are believed to be partly responsible for the anomalously low thermal conductivity of these materials; Winter and Clarke have shown the thermal conductivity of stoichiometric d^0 analogues to be $\approx 2\,\mathrm{W\,m^{-1}\,K^{-1}}$ from 300 K to 1300 K [21].

The present report is a survey of the Nb-rich portion of the WO_3–Nb_2O_5 phase system, which has been selected using a datamining approach and explored using spark plasma sintering (SPS) as a rapid preparation technique. Traditional solid-state preparation of these materials requires extended heat treatments at high temperatures (*e.g.*, 1350°C in sealed platinum crucibles) [31]. This is time consuming, but it also is problematic when working with volatile precursors, such as oxides of W [31]. Further, the final product is a powder that must be consolidated and densified before physical property measurements can be performed. SPS, more accurately referred to as current-assisted pressure-activated densification (CAPAD) [30], provides a rapid preparation route for new oxide materials — a typical reaction takes minutes, instead of hours or days — and yields dense, consolidated solids that can be used for physical property measurements.

6.2 Methods

Polycrystalline samples were made by simultaneous reaction and consolidation of binary oxide and elemental powders (WO_3, 99.9%, Sigma-Aldrich; Nb_2O_5, 99.99%, Sigma-Aldrich, W, 99.99%, Sigma-Aldrich; Nb, 99.8%, Sigma Aldrich) using spark plasma sintering on an instrument from FCT Systeme GmbH, Germany. In a chamber base pressure of 10 torr of argon, 80 MPa uniaxial pressure was applied using a 9 mm inner-diameter graphite die (EDM-4, POCO graphite). The sample was then heated rapidly to 1473 K at 150 K/min, annealed for 6 min at 1473 K, then rapidly cooled at 180 K/min (Figure 6.3). X-ray diffractograms of the resulting dense pellets were measured using a laboratory instrument (Philips X'Pert diffractometer, Cu Kα radiation). Diffractograms collected before and after physical property measurements showed no discernible changes.

High-resolution synchrotron X-ray diffraction (XRD) data on finely-ground powder was acquired at 295 K at beamline 11-BM at the Advanced Photon Source (APS), Argonne National Laboratory, using an average wavelength of ∼0.4137 Å on a diffractometer that has been described in detail by Wang *et al.* [43]. The precise wavelength was determined using a mixture of Si (SRM 640c) and Al_2O_3 (SRM 676) NIST standards run in a separate measurement. Samples were contained in 0.8 mm diameter Kapton capillaries and the packing density was low enough that absorption was not noticeable. Rietveld refinement was performed using TOPAS 5 Academic [222]. Instrument profile parameters were determined using Si (SRM 640c) and LaB_6 (SRM 660b) NIST lineshape standards, run in separate measurements.

SEM was performed on an FEI XL30 microscope using a backscatter electron (BSE) detector; electron dispersive X-ray spectroscopy (EDX) data were collected with an EDAX Si-drift detector. Typical accelerating voltages were 15 or 20 keV. To prepare samples for scanning electron microscopy (SEM), pellets were mounted in epoxy and polished with successively finer abrasives; the final polishing step was performed with $0.25\,\mu$m colloidal diamond suspension on microcloth. A thin layer of Pd–Au, 2 nm to 5 nm, was sputtered on the surface to alleviate charging during imaging. The micrographs presented have not been post-processed in any way. Particle size analysis was performed using ImageJ [236] on a $\sim 33\,\mu\text{m} \times 33\,\mu\text{m}$ area at 2500× magnification to visualize the smallest features, some of which remain sub-pixel diameter even at this magnification. A minimum size cutoff threshold of $0.05\ \mu\text{m}^2$ was used to minimize false positives.

High-temperature thermoelectric properties (electrical resistivity and Seebeck coefficient) were measured with an ULVAC Technologies ZEM-3. Samples had approximate dimensions of $9\,\text{mm}\times 3\,\text{mm}\times 3\,\text{mm}$. Measurements were performed under a helium underpressure, and data was collected through three heating and cooling cycles to ensure sample stability and reproducibility. No changes in electrical properties were observed between cycles, and analysis of the lab XRD patterns from materials after measurements showed no changes in structure nor new phases. Additionally, comparing BSE micrographs collected before and after electrical property measurements revealed no change in microstructure.

The thermal conductivity, κ, was calculated from the density ρ, thermal diffusivity α, and heat capacity C_p, using the relation $\kappa = \rho\alpha C_p$. The densities of consolidated samples were measured using helium pycnometry (MicroMeritics AccuPyc 1340 Pycnometer). To reduce the large systematic errors often introduced by measuring the heat capacity [237], the temperature-dependent heat capacity was estimated using the empirical Neumann-Kopp rule based on the chemical composition and literature values for the heat capacity of WO_3 and Nb_2O_5 [238], as outlined by Leitner *et al.* [239]. The estimated error for the heat capacity introduced by this method is $< 3\%$ at 300 K, and $< 5\%$ at 1000 K. The thermal diffusivity (α) was measured using a Netzsch LFA 457 laser flash system. The samples for the thermal diffusivity measurements were machined to be coplanar with a

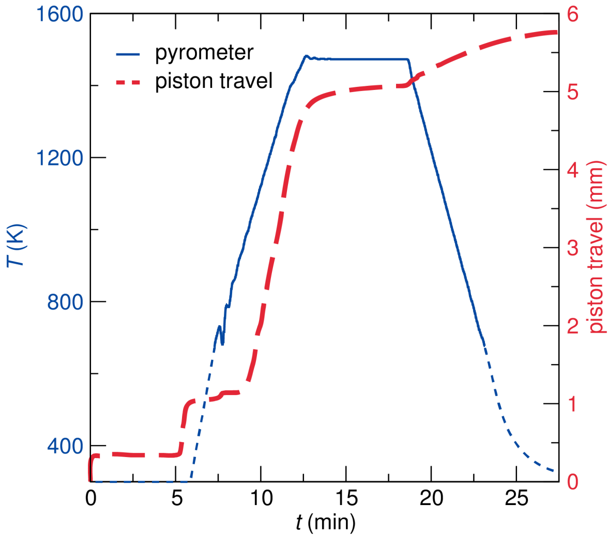

Figure 6.3: SPS was used to prepare dense pellets of $W_xNb_{1-x}O_{2.5+0.5x-\delta}$ composites from a mixture of binary oxides and metal powders in under 30 min. 80 MPa of uniaxial pressure was applied and the sample was heated rapidly from 673 K to 1473 K at 170 K/min, annealed for 6 min at 1473 K, then rapidly cooled at 180 K/min. The temperature profile below 673 K is estimated, as the pyrometer is unreliable below 673 K.

thickness of ∼1 mm and a diameter of ∼8 mm. The samples were then spray coated with colloidal graphite on both sides to ensure full absorption and maximum optical absorption and emissivity. Thermal diffusivity was measured in an argon gas atmosphere from 308 K to 1050 K at intervals of 50 K. A final measurement at 308 K was taken after cooling to ensure reproducibility of the measurements and to ensure the coatings remained intact. The thermal diffusivity values were determined using the Clark and Taylor model [240], which corrects for radiative losses.

6.3 Results and discussion

SPS offers a rapid preparatory route to react and consolidate material in a single processing step, allowing a quick method to prepare samples suitable for measurement of physical properties. The preparation of phase-pure single-cation $WO_{3-\delta}$ and multi-cation

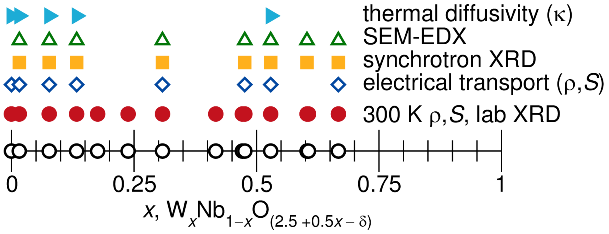

Figure 6.4: SPS was used to prepare 14 samples that were subsequently characterized to elucidate the evolution of thermoelectric properties with composition in the $W_xNb_{1-x}O_{2.5+0.5x-\delta}$ phase system.

Cr_2WO_6 have been previously demonstrated using SPS [241, 242], proving that anion and cation mobility is sufficient to allow diffusion and phase equilibrium in WO_3 systems at these reaction temperatures and timescales. In this work, SPS was used to prepare dense pellets of $W_xNb_{1-x}O_{2.5+0.5x-\delta}$ from a mixture of binary oxides and metal powders in less than 30 min per sample (Figure 6.3). Stoichiometric WO_3, Nb_2O_5, or $(WO_3)_x$–$(Nb_2O_5)_{1-x}$ (d^0 oxides) are good electrical insulators, so the materials were doped with 0.5 electrons per metal cation by adding corresponding amounts of elemental metal to the initial mixture. W is treated as a d^6 donor, Nb is treated as d^5 donor, so 1/12 molar equivalents of W were added for every equivalent of WO_3, and 1/20 equivalents of Nb were added for every equivalent of Nb_2O_5. The final compositions were determined based on the total W and Nb loading, and after initial electrical transport measurements, a subset of these samples were subjected to more rigorous study (Figure 6.4).

Powder X-ray diffraction (XRD) reveals the presence of W metal in many samples, in addition to peaks characteristic of W–Nb–O phases (Figure 6.5). The exact phases were not able to be determined using powder XRD, as the crystal structures have large unit cells with many atomic positions and disorder, the structural similarity between the many phases is revealed only in weak superstructure peaks at low angle ($Q < 1.5$ Å^{-1}). This is particularly difficult because there are many possible superstructures that differ only by small variations in O ordering, and O contributes weakly to the total X-ray scattering

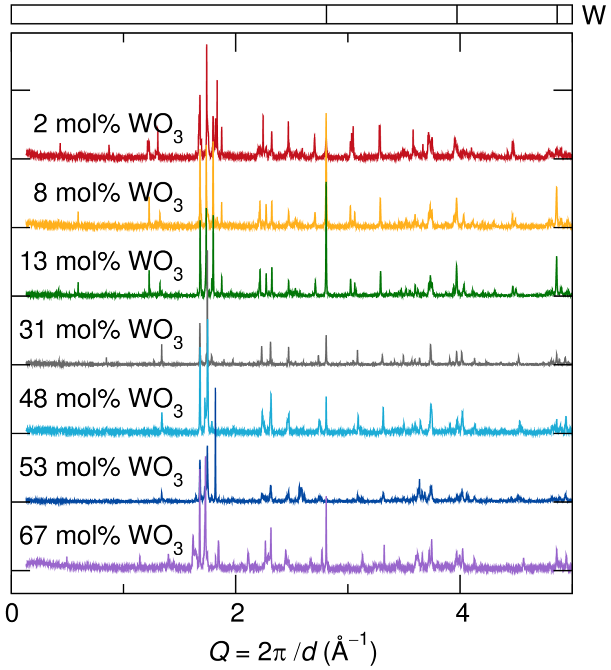

Figure 6.5: Synchrotron XRD was performed on a subset of 8 samples. Although specific W–Nb–O phases were not determined due to the insensitivity of XRD to many of the possible superstructures in these materials, the presence of W metal in most samples is evident.

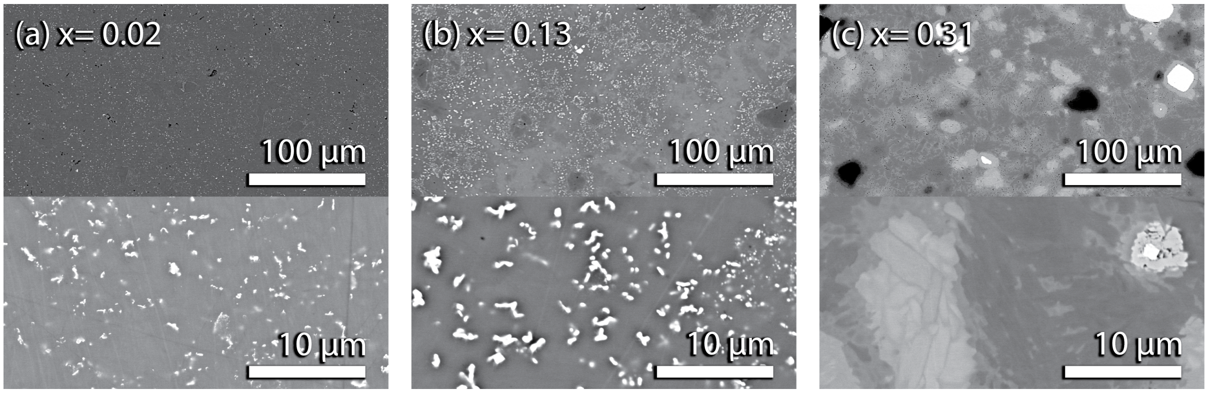

Figure 6.6: Backscatter electron micrographs $W_xNb_{1-x}O_{2.5+0.5x-\delta}$ ($x = 0.02$, 0.13, 0.31) at 200× and 2500× magnification reveal small W-rich precipitates (white) homogeneously distributed throughout samples with low W content ($x \leq 0.13$). At low W content, these secondary phase inclusions form with a range of length scales. The smallest inclusions are sub-pixel diameter ($< 20\,\text{nm}$), whereas the larger inclusions are up to $\sim 2\,\mu\text{m}$ long, covering a wide range of relevant length scales to interact with phonons. The average size and number of precipitates increases with W content in this regime. This microstructure is stable after repeated thermal cycling up to 950 K, the highest temperatures measured. At high W content ($x \geq 0.31$), the microstructure is poorly controlled, and there are larger domains of multiple secondary phases ($\sim 20\,\mu\text{m}$ in width).

because of the high W and Nb content and thus total electron count in these materials. Historically, the difficulties with powder XRD have been addressed, albeit with great difficulty, using single crystal XRD and selected area electron diffraction [243, 244, 245], though this is not possible with the dense composites prepared here.

Scanning electron microscopy (SEM) was performed to better investigate the phase purity and microstructure of the samples, and revealed the presence of multiple phases in each sample. There were no noticeable differences between cross-sections taken from the top or sides of the pellets, suggesting the microstructure is isotropic. Backscattered electron (BSE) micrographs combined with energy-dispersive X-ray spectroscopy (EDX) reveal the presence of W-rich inclusions with a wide range of length scales (Figure 6.6). Owing to the small precipitate size and large interaction volume of EDX, the inclusions may be W metal (as seen by XRD) or W-rich oxides. The smallest inclusions are sub-

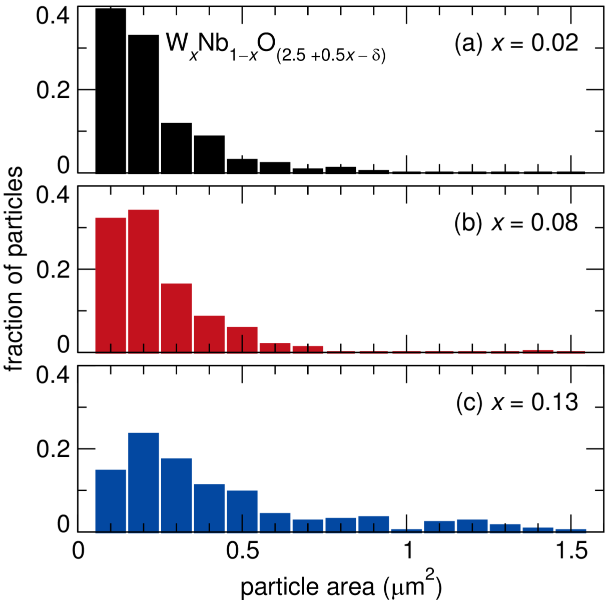

Figure 6.7: The average size of W-rich precipitates measured in BSE micrographs and the area fraction of precipitates increases smoothly with W content when $x \leq 0.13$ in $W_xNb_{1-x}O_{2.5+0.5x-\delta}$. Although many precipitates can be seen in micrographs with sub-pixel diameter (<20 nm; area < 0.001 μm), only precipitates larger than 0.05 μm^2 were used for this analysis in order to minimize false detection events.

pixel diameter (< 20 nm), whereas the larger inclusions are ∼500 nm along their narrow axis and up to ∼2 μm long. The dimensions of these precipitates are ideal for scattering phonons with a broad wavelength distribution and lead to low thermal conductivity at low temperature, as shown later.

Previous studies have demonstrated that WO_3 and W metal can be reacted and consolidated by SPS in a single processing step to prepare single-phase $WO_{3-\delta}$ materials [241]. Further, other work with WO_3-containing materials has demonstrated that cation diffusion rates at 1473 K in SPS are high enough to prepare single-phase materials from powdered oxide precursors in systems with multiple cations, such as Cr_2WO_6 [242]. On the contrary, in the $W_xNb_{1-x}O_{2.5+0.5x-\delta}$ system reported here, we observe multiple phases.

At low W content ($x \leq 0.13$), W-rich secondary phase inclusions are homogeneously distributed and quite small ($< 20\,\text{nm}$ to $\sim 2\,\mu\text{m}$), suggesting possible solubility at high temperature and phase segregation due to precipitation upon rapid cooling (180 K/min) after SPS annealing at 1473 K. Further, the average size and area coverage of the precipitates increases in a controlled fashion with W content (Figure 6.7). Particle size analysis was performed on a $\sim 33\,\mu\text{m} \times 33\,\mu\text{m}$ area at 2500× magnification to visualize the smallest features, some of which remain sub-pixel diameter even at this magnification. The precipitate sizes appear to follow log-normal distributions, though meaningful fitting would require more statistics of particles with smaller sizes. Although many precipitates of sub-pixel diameter ($<20\,\text{nm}$; area $< 0.001\,\mu\text{m}^2$) can be seen in micrographs, only precipitates larger than $0.05\ \mu\text{m}^2$ were used for this analysis to minimize false detection events.

At high W content ($x \geq 0.31$), in contrast, the microstructure is poorly controlled, and there are larger domains of multiple secondary phases ($\sim 20\,\mu\text{m}$ in width). This is not unexpected, as increasing the W content should increase the domain size of W-rich inclusions up to some point at which these secondary phases coalesce and segregate to minimize interfacial area and lower the total energy. This change in behaviour is likely related to the critical percolation threshold, which would occur at 27% site filling in a random close packed 3-dimensional lattice [246].

6.3.1 Thermoelectric properties

Electrical transport properties of $\text{W}_x\text{Nb}_{1-x}\text{O}_{2.5+0.5x-\delta}$ were measured up to 950 K (Figure 6.8). The electrical resistivity (ρ) increases with W content up to $x = 0.13$, after which it begins to decrease up to $x = 0.67$, the highest W content measured. The Seebeck coefficient (S) changes predictably in opposition to the electrical resistivity with composition. The power factor, $S^2\rho^{-1}$, increases monotonically with temperature up to at least 950 K, the highest temperature measured. With regard to sample composition,

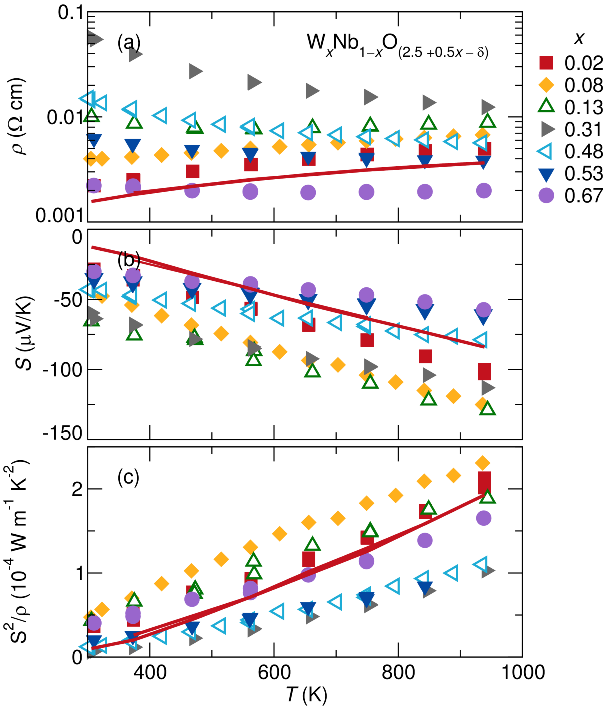

Figure 6.8: $W_xNb_{1-x}O_{2.5+0.5x-\delta}$ displays metallic electrical transport when $x \leq = 0.08$, and maximum electrical performance (S^2/ρ) for thermoelectric considerations is seen at $x = 0.08$. The electrical transport properties of the materials do not change, even after repeated thermal cycling up to the maximum temperatures measured, 950 K. $x = 0.02$ materials made using traditional solid-state (line) method have comparable properties to the one-step SPS materials.

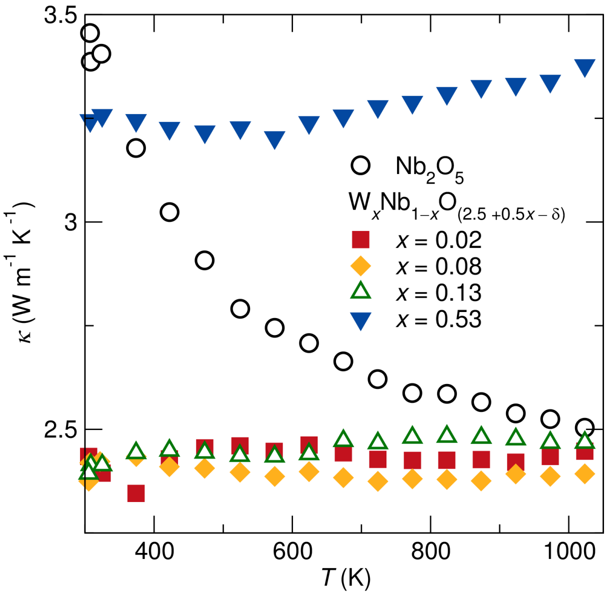

Figure 6.9: Remarkably small W content ($W_xNb_{1-x}O_{2.5+0.5x-\delta}$, $x = 0.02$) is sufficient to decrease the thermal conductivity compared to Nb_2O_5, particularly at low temperatures where longer-wavelength phonons are the dominant carriers of heat. Despite the increase in electrical thermal conductivity, the total thermal conductivity $x = 0.02$ composites is reduced by 30% at 300 K compared to insulating Nb_2O_5. The thermal conductivity of these biphasic materials is largely invariant with temperature, likely because long-wavelength phonons at low temperatures are scattered by the W-rich precipitates that span length scales of < 20 nm to $\sim 2\,\mu$m. At high W content and above the percolation threshold of W-rich domains, the same reduction in thermal conductivity is not seen.

the maximum power factor is obtained for samples with $x = 0.08$.

Several samples were also made by a traditional solid state reaction of precursors in evacuated silica ampoules at 700° for 48 hours [243], followed by densification using the same SPS processing. Samples made using this two-step process displayed similar X-ray diffraction patterns and high-temperature electrical transport properties (electrical resistivity and Seebeck coefficient) as analogous samples made using a one-step process.

Thermal conductivity was determined for a smaller subset of samples (Figure 6.9) to determine the influence of the microstructure observed in BSE micrographs (Figure 6.6). Densities used to calculate thermal conductivity were obtained through He pycnometry on consolidated pellets. Although the relative density (compared to the theoretical maximum single-crystal density) cannot be unambiguously known due to the presence of multiple phases, the samples examined here are likely near 100% single-crystal density; scanning electron microscopy of polished cross-sections reveals no evidence of significant porosity, and previous work on stoichiometric d^0 analogues achieved densities of 97% to 100% using traditional hot pressing [21].

For $W_xNb_{1-x}O_{2.5+0.5x-\delta}$ samples with low W content ($x \leq 0.13$), the thermal conductivity is $\sim 2.5\,\mathrm{W\,m^{-1}\,K^{-1}}$ from 300 K to 1050 K (Figure 6.9). The thermal conductivity of all composites it is largely invariant with temperature, likely because long-wavelength phonons at low temperatures are scattered by the W-rich precipitates that span length scales from $< 20\,\mathrm{nm}$ to $\sim 2\,\mu\mathrm{m}$, which prevents these phonons from carrying heat. For comparison, the thermal conductivity of stoichiometric Nb_2O_5, prepared using the same SPS processing conditions, was determined as a reference. Although the thermal conductivity of Nb_2O_5 approaches the composites at high temperatures ($T > 1000\,\mathrm{K}$), it is clear the composites achieve the minimum thermal conductivity at room temperature due to phonon scattering from precipitates.

Composites with low W content have superior thermoelectric performance in every regard compared to Nb_2O_5. Nb_2O_5 is too insulating to measure electrical resistivity, whereas $W_xNb_{1-x}O_{2.5+0.5x-\delta}$ materials exhibit metallic electrical transport. Despite the expected increase in thermal conductivity due to the contribution from electrical carriers, the thermal conductivity decreases by 30% at 300 K compared to insulating Nb_2O_5. Although the dominant reason for this decrease is likely the secondary phase inclusions, intrinsic defects in the crystal structure may also play a role (*e.g.*, crystallographic shear planes, site defects from oxygen deficiency, and mass contrast from W/Nb site substitution). Taken together with electrical property measurements, thermal conductivity measurements reveal zT achieved in these samples is for the $x = 0.08$ member ($zT = S^2\rho^{-1}T$), which achieves a $zT = 0.1$ at 950 K, the highest temperature measured here (Figure 6.10).

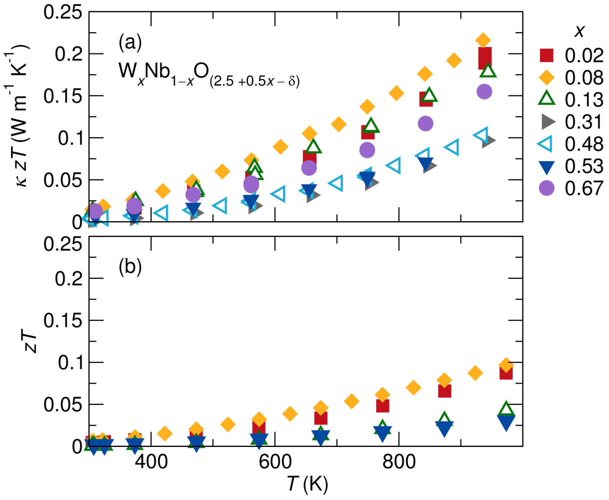

Figure 6.10: Physical property measurements reveal that the highest power factor and zT achieved in these samples is for the $x = 0.08$ member, which achieves a $zT = 0.1$ at 950 K, the highest temperature measured here. κzT is shown to provide a normalized zT without consideration of thermal conductivity.

6.4 Conclusions

Early transition metal oxides were targeted using a datamining approach, and dense pellets of $W_xNb_{1-x}O_{2.5+0.5x-\delta}$ composites were prepared by SPS, which led to simultaneous reaction and densification of WO_3, Nb_2O_5, W, and Nb powders in 6 min at 1473 K. The samples were doped to nominally have 0.5 electrons per metal cation. Backscattered electron micrographs revealed samples with low W content ($x \leq 0.13$) have W-rich secondary phase inclusions with dimensions spanning from < 20 nm to $\sim 2\,\mu$m. The average size and number of these precipitates increases controllably with W content, and the dimensions of these precipitates are ideal for scattering phonons with a broad wavelength distribution. Further, these inclusions are stable even after repeated thermal cycling, and the electrical properties do not change after repeated thermal cycling up to the highest temperatures measured, 950 K. This leads to composite materials with reduced thermal conductivity across all temperatures investigated (300 K to 1050 K), even with W content as low as 0.3 mol% ($x = 0.02$ in $W_xNb_{1-x}O_{2.5+0.5x-\delta}$).

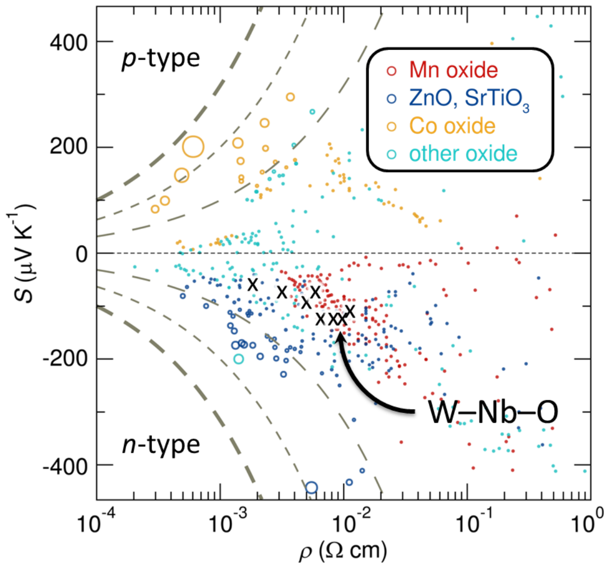

Figure 6.11: W–Nb–O materials contextualized within the larger survey plot of current oxide thermoelectric materials reveals that W–Nb–O materials (X) are an exciting platform for potential n-type oxides. The $W_xNb_{1-x}O_{2.5+0.5x-\delta}$ composites studied here have comparable performance to $CaMnO_3$ based materials, despite not having been optimized at this stage. The size of the circle is proportional to the material power factor, which is the electrical component of the thermoelectric figure of merit (zT). Dashed lines of constant power factor give bounds for reasonable thermoelectric performance, and this plot reveals the lack of high-performance n-type oxide materials. Data from [205].

These $W_xNb_{1-x}O_{2.5+0.5x-\delta}$ composites are a promising platform for n-type oxide thermoelectric materials. Even without electronic optimization (*e.g.* doping studies), these composites are in the same performance class at $CaMnO_3$-based materials, which have been heavily researched (Figure 6.11). Physical property measurements reveal that the highest power factor and zT achieved in these samples is for the $x = 0.08$ member, which achieves $zT = 0.1$ at 950 K. Although this is the highest temperature measured here, the materials are stable to higher temperatures, where the zT should be higher. Further studies should lead to improvement in electrical transport properties, and improved thermoelectric performance in a class of n-type oxides that are stable at high temperature.

Chapter 7

A recommendation engine for suggesting unexpected thermoelectric chemistries

---

[1] A version of this chapter was co-written with Dr. Bryce Meredig, and has been submitted for publication: Michael W. Gaultois, Anton O. Oliynyk, Arthur Mar, Taylor D. Sparks, Gregory J. Mulholland and Bryce Meredig. A recommendation engine for suggesting unexpected thermoelectric chemistries.

The experimental search for new thermoelectric materials remains largely confined to a limited set of successful chemical and structural families, such as chalcogenides, skutterudites, and Zintl phases.[28, 6, 29] In principle, computational tools such as density functional theory (DFT) offer the possibility of rationally guiding experimental synthesis efforts toward very different chemistries. However, in practice, predicting thermoelectric properties from first principles remains a challenging endeavor[247], and experimental researchers generally do not directly use computation to drive their own synthesis efforts. To bridge this practical gap between experimental needs and computational tools, we report an open machine learning-based recommendation engine (`http://thermoelectrics.citrination.com`) for materials researchers that suggests promising new thermoelectric compositions, and evaluates the feasibility of user-designed compounds. We show that this engine can identify interesting chemistries very different from known thermoelectrics. Specifically, we describe the experimental characterization of one example set of compounds derived from our engine, $RE_{12}\mathrm{Co}_5\mathrm{Bi}$ ($RE = \mathrm{Gd}$, Er), which exhibits surprising thermoelectric performance given its unprecedentedly high loading with metallic d and f block elements, and warrants further investigation as a new thermoelectric material platform.

7.1 Introduction

For any materials problem, breaking out of “local optima” in composition space to discover entirely new chemistries remains a notoriously difficult challenge.[248] Many of the most notable materials classes under investigation today–from $\mathrm{Na}_x\mathrm{CoO}_2$ derived thermoelectrics [26] to iron arsenide superconductors [27]–were discovered fortuitously. As a result, experimental efforts often gravitate toward incrementally improving *known* chemistries (via doping, nanostructuring, etc.), as these efforts are more likely to bear fruit than high-risk searches through chemical whitespace for entirely new materials.

The consequence of research communities' focus on further exploitation of known chemistries rather than exploration of unknown chemistries is that much of composition space simply remains uncharacterized. In Figure 7.1a, we illustrate the remarkable chemical homogeneity of most thermoelectric materials investigated to date. We plot each material from the thermoelectric database of Gaultois *et al.*[205] on the periodic table based on the composition-weighted average of the positions of elements in the material. The tight cluster of previously investigated chemistries is, as expected, dominated by chalcogenides and *p*-block elements such as Sn and Sb. In contrast, we also show the positions of $Gd_{12}Co_5Bi$ and $Er_{12}Co_5Bi$, materials derived from our recommendation engine, which we characterize as a new class of thermoelectrics in this work. These materials are almost pure intermetallics, in sharp contrast to thermoelectric compounds investigated to date (Figure 7.1b). The objective of our recommendation engine is to directly enable experimental researchers to rapidly identify new materials, such as $RE_{12}Co_5Bi$, that are very distinct from known compound classes, and worthy of further study.

Experimental details

$RE_{12}Co_5Bi$ (RE = Gd, Er) samples were made by arc-melting freshly filed Er or Gd pieces (99.9%, Hefa), Co powder (99.8%, Cerac), and Bi powder (99.999%, Alfa Aesar). Stoichiometric mixtures (0.5 g total mass) with 5-7% excess of bismuth were pressed into pellets and melted twice in arc-melting furnace under argon atmosphere (Edmund Bühler Compact Arc Melter MAM-1). The total mass loss after melting was $< 1\%$. The samples were sealed in silica tubes and annealed at 1070 K for one week, then quenched in cold water. To produce enough material for physical property measurement, ~70 samples of each compound were prepared, and pure samples were combined by melting into a single ingot of ∼5 g, which was sanded to yield the appropriate geometry (either a rectangular bar, or a cylinder). Density was measured using Archimedes' method; the final pellets had densities 100% of the single crystal values ($\rho_{\mathrm{Gd_{12}Co_5Bi}} = 8.6\,\mathrm{g/cm^3}$, $\rho_{\mathrm{Er_{12}Co_5Bi}} = 9.9\,\mathrm{g/cm^3}$).

Powder X-ray diffraction patterns were collected using an INEL CPS 120 diffractometer with Cu Kα_1 radiation at room temperature. Rietveld refinement was used to confirm the structure and phase purity.

High-temperature thermoelectric properties (electrical resistivity and Seebeck coefficient) were measured with an ULVAC Technologies ZEM-3. Sample bars had approximate dimensions of 9 mm×4 mm×4 mm. Measurements were performed with a helium under-pressure, and data was collected from 300 K to 800 K through three heating and cooling cycles over 18 hours to ensure sample stability and reproducibility.

7.2 A materials recommendation engine

Our recommendation engine is a machine learning-based approach[249, 250] for efficiently driving synthetic efforts toward promising new chemistries. We have trained a machine learning model to make a binary true/false prediction of whether the (1) Seebeck coefficient, (2) electrical resistivity, (3) thermal conductivity, and (4) band gap of input materials are within acceptable ranges for thermoelectric applications. We define these ranges as follows: (1) $|S| > 100\,\mu\mathrm{V\,K^{-1}}$; (2) $\rho < 10^{-2}\,\Omega\,\mathrm{cm}$; (3) $\kappa < 10\,\mathrm{W\,m^{-1}\,K^{-1}}$; and (4) $E_\mathrm{g} > 0\,\mathrm{eV}$. We would classify any material for which the answer to all these questions is "yes" as a potentially promising thermoelectric that may warrant further study. The purpose of our recommendation engine is thus neither to make *quantitative* predictions of these thermoelectric properties, nor to definitively identify record-setting compounds– these remain open challenges for future work. Rather, the engine is intended to greatly augment the chemical intuition of experimental researchers working on materials dis-

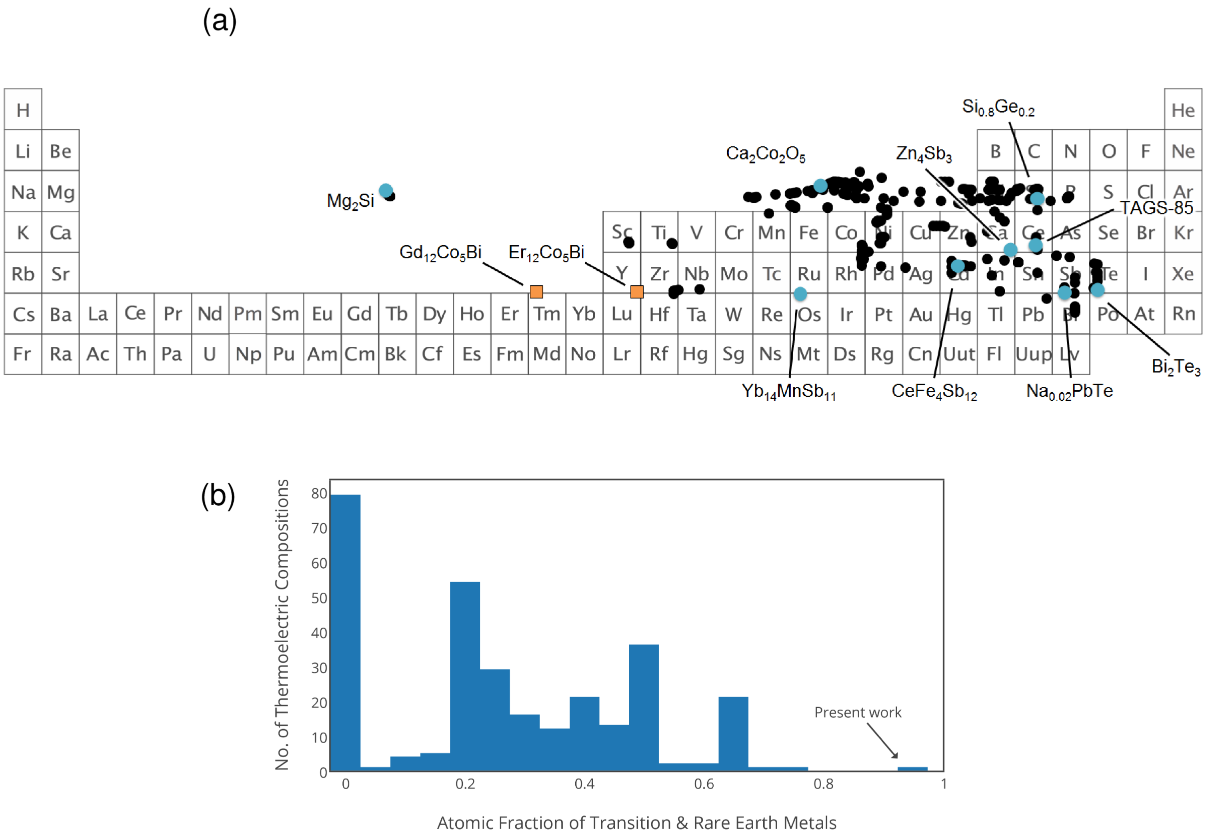

Figure 7.1: (a) Most known thermoelectric materials lie in a tight cluster in composition space (black and blue dots; blue dots have chemical formulae explicitly labeled). The recommendation engine presented here allows the identification of new thermoelectric materials families that are well outside the existing composition space of common systems; in particular, we report the characterization of $RE_{12}Co_5Bi$ ($RE = Gd$, Er; orange squares) in this work, which are chemically and structurally distinct from known thermoelectrics. (b) The strongly intermetallic $RE_{12}Co_5Bi$ compounds we report here lie far outside the norm for metal loading among collected thermoelectric compositions in the Gaultois *et al.*[205] database.

covery. In particular, we have found that our model's ability to screen vast numbers of possible compositions and short-list interesting candidates can inspire materials syntheses that would not have been obvious *a priori*.

Model validation

The training set for our recommendation engine comprises a large body of both experimental thermoelectric characterization data [205] and first principles-derived electronic structure data [248, 251]. Our model uses these input data to learn interesting chemical trends that could be exploited to design new materials. We visualize the accuracy of our recommendation engine's predictions in Figure 7.2, which represents the results of leave-one-out cross-validation (LOOCV) on our training data (in the case of the band gap data, we performed LOOCV on a subset of the extremely large training set). In the LOOCV procedure, if we have n total measurements of a particular property such as thermal conductivity, we train our machine learning model on $n - 1$ of these values and predict the nth (left out) value. We perform one training step and prediction for each property value, and present the error distribution for all n values in Figure 7.2. The error distribution then provides us with a sense of how we may expect the model to perform on new materials of which we have no prior knowledge.

Figure 7.2 indicates that our engine generally makes very reliable assessments of thermoelectric materials properties. The modes of the error distributions are in each case close to 0. For each property, the engine's errors skew toward false negatives (resistivity, band gap, thermal conductivity) or false positives (Seebeck), which reflects the fact that the underlying training data do not contain equal fractions of positive and negative examples. Seebeck coefficients prove most difficult to assess (*i.e.*, the error distribution for that property has the largest standard deviation), likely because there are strikingly

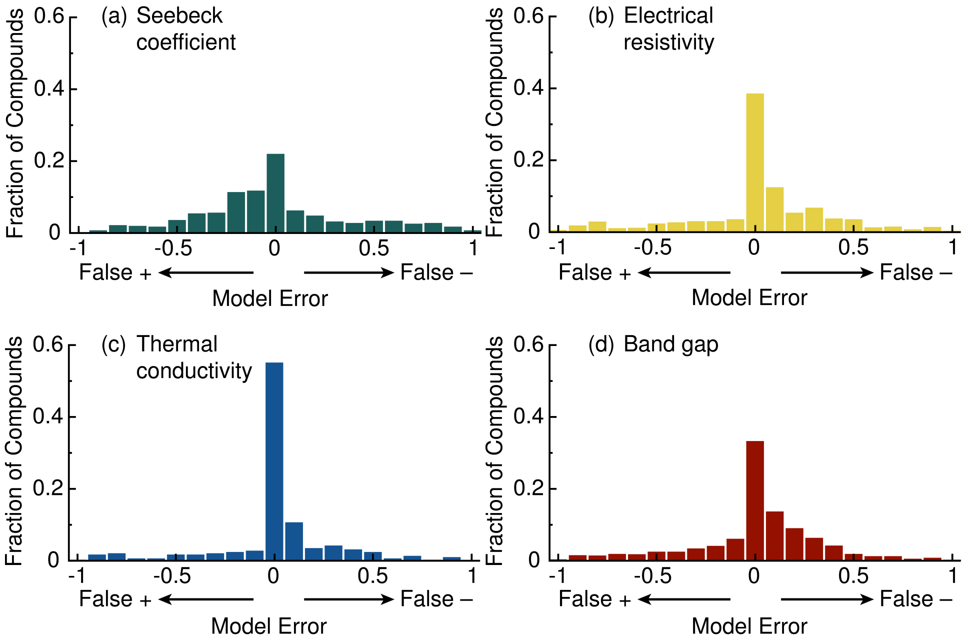

Figure 7.2: Leave-one-out cross validation error histograms for the four key properties estimated by our recommendation engine: (a) Seebeck coefficient; (b) electrical resistivity; (c) thermal conductivity; and (d) band gap. For each material in our training set and each property, the recommendation engine gives a confidence score between 0 and 1 that the property value falls within the ideal windows we have defined for thermoelectric applications. Errors approaching +1 represent false negatives (our engine thought the material would be poor for that property, but it is actually good); and an error of −1 is a false positive (our engine thought the material would be good for that property, but it is actually poor).

different mechanisms that underpin the values, for example, strongly correlated oxides as opposed to degenerate semiconductors.

7.3 Discussion

In this work, we are interested not only in developing a model that gives accurate predictions of materials properties, but also in making it immediately accessible and useful for experimental researchers. To that end, we have published our recommendation engine as a web app at `http://thermoelectrics.citrination.com`, where researchers may explore a pre-computed list of around 25 000 known compounds, and also use our model to evaluate in real-time their own materials candidates. In this way, we hope that the app serves as a rapid triage tool for ideas for potential new thermoelectric materials. Our pre-computed list may be arranged according to the probabilities associated with any one of the four properties we are modeling, and is sorted by default according a composite score that takes all four properties into account. Furthermore, the user may specify cutoff thresholds for any of the properties, and thereby greatly reduce the size of the list.

As we believe our extensive precomputed list contains some interesting and heretofore uncharacterized candidate thermoelectric materials, we now comment on a select set of high-ranking compounds. Several of these compounds are given in Table 7.1.

$TaVO_5$ and $TaPO_5$ occur in an analogous crystal structure to the phosphate tungsten bronzes [252, 253]. These materials can be expected to have good thermoelectric performance given the heavy atoms, the potential for low electrical resistivity provided by the repeating ReO_3-type structural network that is highly connected in three dimensions, and the intrinsic crystallographic shear provided by the crystal structure. Although the phosphate tungsten bronzes themselves are not highly rated, their metallic electrical transport

Table 7.1: Several promising new thermoelectric compounds selected from our pre-computed list. The full list is available for exploration at `http://thermoelectrics.citrination.com`.

Material	P_S	P_ρ	P_κ	P_{gap}	Composite	Comments
$TaPO_5$ and $TaVO_5$	0.894	0.793	0.958	0.987	3.537	High polyhedral connectivity and structural superlattices
Tl_9SbTe_6	0.845	0.871	0.999	0.876	3.46	Recently reported to be a good thermoelectric ($zT \approx 1$ at 600 K)
$TaAlO_4$	0.893	0.703	1	0.977	3.477	High mass contrast, high polyhedral connectivity(edge- and corner-sharing TaO_6 octahedra)
$SrCrO_3$	0.772	0.767	0.996	0.95	3.308	High polyhedral connectivity (3-D corner-sharing CrO_6 octahedra), metallic when made under high pressure
$TaSbO_4$	0.892	0.919	1	0.997	3.559	High polyhedral connectivity: layered, edge-sharing MO_6 octahedra

properties are encouraging for structural analogues [254]. Moreover, $TaVO_5$ has a negative coefficient of thermal expansion and a structural transition at 600○C [255]. This structural transition may lead to softening of phonon modes and anharmonic scattering, which may lead to low thermal conductivity. The second material of interest we present is Tl_9SbTe_6. Though this compound was not included in the thermoelectric database, it scores highly within the recommendation engine, and good thermoelectric performance has been subsequently demonstrated in recent work [256].

The suggestion of $TaAlO_4$, $SrCrO_3$, $TaSbO_4$ and other oxides expected to be insulators can be understood because the recommendation engine uses as training data references where stoichiometric formulas were primarily reported rather than doping details.[257, 258] Nevertheless, with doping through substitution or reduction, these compound may exhibit moderate electrical performance. Further, these materials all feature extended structures that are highly connected in three dimensions, an important feature for low electrical resistivity. Moreover, the large mass contrast on the cation sublattice in $TaAlO_4$ (edge shared TaO_6 and AlO_6 octahedra) could lead to low thermal conductivity, and previous reports have shown that $SrCrO_3$ is metallic when synthesized under pressure [259].

Many of the high-ranking candidate materials are interesting because of their highly connected extended structures, even though the recommendation engine does not use features of crystal structure to make its suggestions. The chief disadvantage to training prediction algorithms using crystal structure is that structure then becomes a *required input* for making predictions, and yet structure is by definition not available for uncharacterized materials. However, the absence of crystal structure does cause our engine difficulty where changes in crystal structure with similar elemental compositions cause large changes in physical properties. For example, both $DyPO_4$ and $LaPO_4$ are predicted to have low thermal conductivity. However, $LaPO_4$ is monazite, a corner edge-shared structure, whereas $DyPO_4$ is xenotime [260], an edge-shared structure leading to inherently higher thermal conductivity.[21]

New materials and their properties

Our final and most important task in this work is to demonstrate that our recommendation engine can indeed guide researchers toward interesting experimental discoveries. Among the set of high-scoring candidate materials, we selected $Er_{12}Co_5Bi$ and $Gd_{12}Co_5Bi$ to characterize as thermoelectric materials due to their facile synthesis through arc melting, and due to the fact they are chemically quite distinct from known thermoelectrics (Figure 7.1). While the $RE_{12}Co_5Bi$ ($RE=$ rare earth) family of compounds has only been sparsely studied in the literature, their crystal structure and initial low-temperature electrical and magnetic properties have been reported by Mar and coworkers [261]. The crystal structure of $RE_{12}Co_5Bi$ is shown in Figure 7.3.

Interestingly, the crystal structure of our candidate thermoelectric exhibits notable similarity to the structures of known thermoelectrics, in spite of the fact that crystal structure was not an input feature for our recommendation engine. $Ho_{12}Co_5Bi$ is the eponymous structure prototype (orthorhombic, space group *Immm*) adopted by a series of rare-earth intermetallics $RE_{12}Co_5Bi$ ($RE = \mathrm{Y}, \mathrm{Gd}, \ldots, \mathrm{Tm}$). In this structure, the $Ho_{12}Bi$ icosahedra play an analogous role to the LaP_{12} icosahedra in the filled skutterudite prototype $LaFe_4P_{12}$; rare-earth atoms “rattling” within their 12-fold coordinated cages is the idiosyncratic feature of filled skutterudites that imparts low thermal conductivity so prized in thermoelectric materials. In fact, if the transition metal atoms, which occupy different sites in these structures, are disregarded, the $Ho_{12}Bi$ framework is an antitype to the LaP_{12} framework, with the roles of the rare-earth and group 15 elements reversed. We hypothesize its crystallographic similarity to skutterudite could be partly responsible

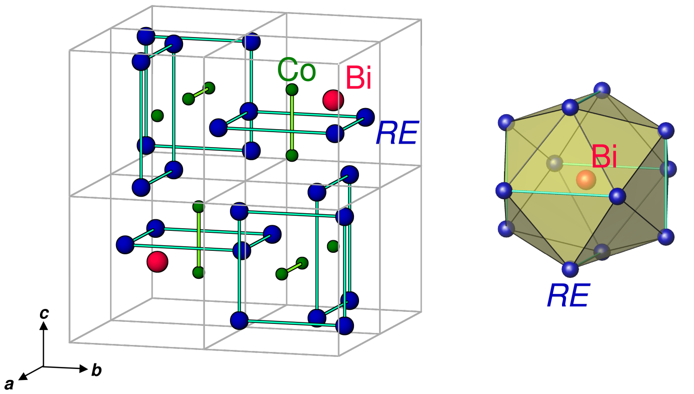
(a) RE_{12}Co$_5$Bi

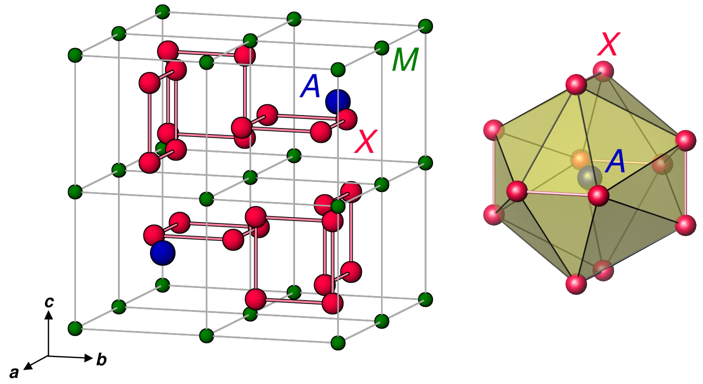
(b) AM_4X_{12}

Figure 7.3: (a) Crystal structure of $RE_{12}\mathrm{Co}_5\mathrm{Bi}$ (prototype $\mathrm{Ho}_{12}\mathrm{Co}_5\mathrm{Bi}$), of which $\mathrm{Er}_{12}\mathrm{Co}_5\mathrm{Bi}$ and $\mathrm{Gd}_{12}\mathrm{Co}_5\mathrm{Bi}$ are exemplars. (b) Crystal structure of the filled skutterudites, which have the generic chemical formula AM_4X_{12}. These two structure types share an icosahedral motif consisting of $RE_{12}\mathrm{Bi}$ and AX_{12} units, respectively.

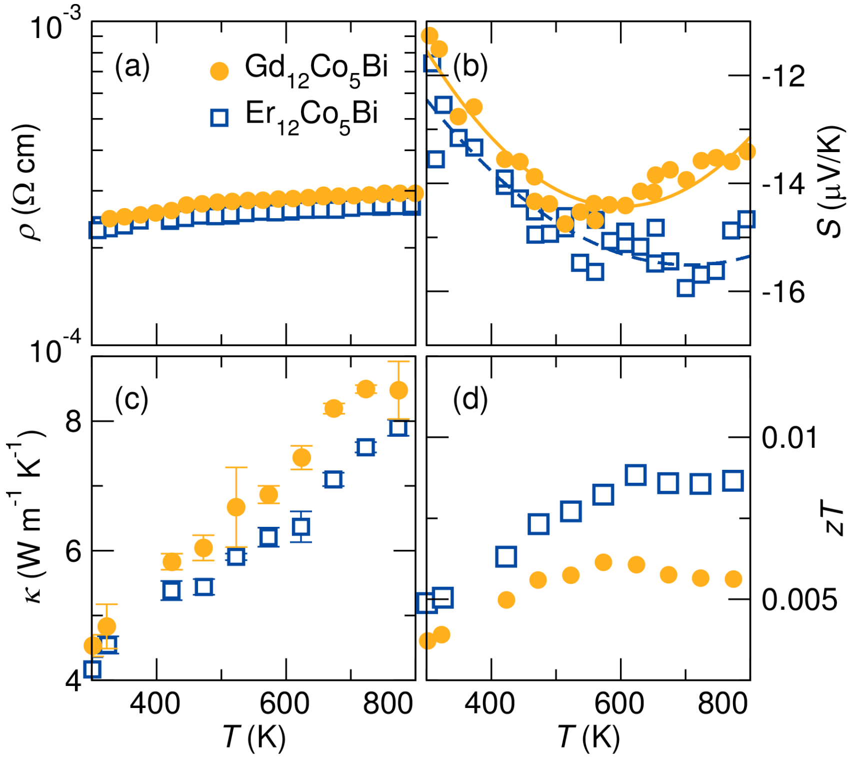

Figure 7.4: Thermoelectric characterization of $RE_{12}Co_5Bi$ (RE = Gd, Er). (a) Electrical resistivity, (b) Seebeck coefficient, (c) thermal conductivity, and (d) thermoelectric figure of merit zT as a function of temperature.

for the thermoelectric behavior of $RE_{12}Co_5Bi$ (RE = Gd, Er).

We give a full thermoelectric characterization of $Er_{12}Co_5Bi$ and $Gd_{12}Co_5Bi$ in Figure 7.4. Based on these results, we report the discovery of a new thermoelectric class, which remains a completely unoptimized, pure bulk material and thus lends itself to further study. Notably, the material falls far outside the usual search space for thermoelectrics (Figure 7.1), and was neither the result of simple interpolation between known compounds nor obvious from a strict chemical intuition standpoint. The electrical resistivity is commensurate with other high-performing materials such as chalcogenides, although the Seebeck coefficient is too low for the material to be competitive with the best-known thermoelectrics. Furthermore, the thermal conductivity is relatively high, but the filled cage structure lends itself to substitution that has successfully reduced thermal conductivity in the skutterudite systems [210, 29]. In $RE_{12}\mathrm{Co}_5\mathrm{Bi}$ ($RE = \mathrm{Gd}$, Er), the thermal conductivity from 300 K to 800 K ranges from $4\,\mathrm{W\,m^{-1}\,K^{-1}}$ to $8\,\mathrm{W\,m^{-1}\,K^{-1}}$, comparable to the half-Heuslers [262, 214]. The electrical performance figure of merit κzT is around 0.03 at 400 K, which is actually higher than that of nearly 30% of the thermoelectrics in the Gaultois *et al.* thermoelectrics database;[205] of course, the database is a highly self-selected set of materials, consisting of literature-reported thermoelectrics, and would skew toward much higher κzT values than would a random subset of all crystalline materials. We note, of course, that the zT of several other thermoelectric materials can be significantly improved through carrier concentration tuning and microstructural engineering. For example, undoped polycrystalline Si has a 60-fold increase in performance after optimization, going from $zT < 0.01$ to 0.6 at 300 K [263].

Another observation from Figure 7.4 illustrates the scientific boon of studying entirely new classes of materials. Unexpectedly, $RE_{12}\mathrm{Co}_5\mathrm{Bi}$ ($RE = \mathrm{Gd}$, Er) exhibits *increasing* thermal conductivity with temperature. The increasing electrical resistivity with temperature indicates metallic electrical transport, so the electrical contribution to the total thermal conductivity should therefore decrease with increasing temperature. Additionally, the phonon contribution to thermal conductivity should also decrease with increasing temperature due to more phonon–phonon (Umklapp) scattering [117]. Thermal conductivity is calculated from the following relation: $\kappa = \alpha\,\rho\,C_\mathrm{p}$, where α is thermal diffusivity, C_p is heat capacity, and ρ is density. Normally, thermal diffusivity has a negative temperature dependence whereas heat capacity and density both have positive temperature dependence. However, for this compound we observe a *positive* temperature dependence for the thermal diffusivity even after multiple measurements, the origin of which is not presently understood. Materials with increasing thermal conductivity with temperature are rare, though not unprecedented [264, 265], and further studies on this class of compounds to shed light on this anomaly could thus lead to new strategies for thermoelectric materials optimization.

7.4 Conclusions

This initial experimental validation of our recommendation engine is encouraging. The present work represents the first time that machine learning has been used to suggest an experimentally viable new compound from true chemical white space, where no prior characterization had hinted at promising chemistries. The implication is that our approach–wherein a data-driven computational tool directly augments experimental capabilities and intuition–is a semi-rational way to discover new materials families that may have desirable properties. We suggest that such an paradigm could eventually replace trial-and-error and fortuity in the search for new materials across a wide variety of application areas.

Chapter 8

Summary and outlook

The work presented here has highlighted the creation and development of datamining strategies and frameworks that have been used to develop and implement design principles for oxide thermoelectric materials. Oxides can assume a wide range of possible electrical resistivities, from metallic (*e.g.*, RuO_2 or ReO_3) to insulating (*e.g.*, TiO_2 or SiO_2), and it was unclear before this work where the optimal zone of performance should lie in parameter space. For oxides, we have shown here that materials must have an electrical resistivity below $10^{-2}\,\Omega\,\text{cm}$ and Seebeck coefficient above $100\,\mu\text{V/K}$ for any reasonable thermoelectric performance. This dramatically restricts the design space of oxide thermoelectric materials, which is important to guiding future studies. The visualization tools developed in this work have been applied to the database constructed in this work, and have revealed several important features in existing thermoelectric materials:

1. Using the survey maps created in this work, we note materials tend to cluster, rather than change drastically from regions of poor to high performance.
2. Improving the electrical properties (*i.e.*, power factor) is non-trivial in even the most-studied systems (*e.g.*, band engineering, resonant-level doping, quantum wells), and unfathomable in many oxide systems.
3. Given the previous claims listed above, we should rapidly search for new materials that have good electrical properties, rather than trying to optimize systems that are far from good performance.

These findings have led to design criteria for high-performance oxide thermoelectric materials:

1. Any reasonable thermoelectric performance requires metallic electrical transport. In other words, $\rho < 10^{-2}\,\Omega\,\text{cm}$.

2. To get metallic electrical transport in oxides, structures with high polyhedral connectivity are required.

3. Highly interconnected structures often result in high thermal conductivity, which can be counteracted by employing extrinsic, secondary phase inclusions, or intrinsic, crystallographic defects.

These criteria are met in reduced early transition metal oxides, such as the Nb_2O_5–WO_3 composite materials reported here, which were *deliberately targeted* as candidate thermoelectric materials following the criteria established in this work, and which we show have promising performance for n-type oxide thermoelectric materials. These materials have metallic electrical transport and highly connected crystal structures to permit low electrical resistivity, while having intrinsic crystallographic defects that lead to a low thermal conductivity ($\sim$2.5 W m^{-1} K^{-1} from 300 K to 950 K). Additionally, we report control over the size distribution of W-rich precipitates, which reduce the thermal conductivity compared to Nb_2O_5, even at W loadings as low as 0.3 mol%, the lowest W content investigated ($x = 0.02$ in $W_xNb_{1-x}O_{2.5+0.5x-\delta}$). The best-performing composition studied displays a thermoelectric figure of merit $zT = 0.1$ at 950 K, the highest temperature measured, and zT increases at higher temperatures not accessible using our instrumentation. Even in the initial report here without optimization, these materials display superior zT values compared to other n-type oxides that have been actively researched for decades. The wide variety of reduced early-transition metal oxides is an exciting platform for future studies, and should lend itself well to exploring the phase space of possible thermoelectric materials.

The complex crystal structures and high polyhedral connectivity in these early transition metal oxide systems is a rich space to explore, and though these materials have traditionally been difficult to prepare due to issues of volatility and reactivity, we show that spark plasma sintering (SPS) overcomes these challenges and can rapidly prepare samples suitable for physical property measurement. We propose the rapid reaction times may be possible due to the reducing conditions during SPS processing, which are able to partially reduce some cations (such as Cr^{3+} and W^{6+}). This partial reduction leads to rapid diffusion of cations and anions through the creation of labile coordination environments and oxygen vacancies. The ability to quickly prepare dense materials from powdered precursors in a single step via SPS significantly reduces the time necessary to explore the compositional space of candidate thermoelectric material systems, and will be important in exploring new compositional space.

In addition to having developed rational design guidelines for the discovery of new materials, we have also developed strategies to evaluate the performance of existing materials. Much effort is spent reducing the thermal conductivity of thermoelectric materials, but before this work it was unclear to what extent thermal conductivity can be reduced, particularly for materials that have already undergone extensive microstructure engineering. We have employed a simple mathematical derivation and developed visualization tools and screening methods to visualize the performance gains possible by reducing the thermal conductivity in existing thermoelectric materials. Combined with the large thermoelectrics database described in this work, these tools allow researchers to quickly identify which materials are nearly optimized and which materials have room for improvement and deserve further study.

Assembling and visualizing large amounts of data using newly-developed plot styles and frameworks has been fruitful, but will be ultimately be limited by the low number of dimensions that can be simultaneously visualized. “Big data” strategies will ultimately be necessary to exploit large and complex datasets, and are useful to develop more complicated and less evident approaches for new material discovery. Due to the complicated nature of the underlying physics, these correlation-driven approaches may yield new insight into our understanding of what leads to high thermoelectric performance. We have trained machine learning algorithms using our thermoelectrics database, and the resulting material recommendation engine can suggest chemical compositions likely to exhibit good thermoelectric performance. This recommendation engine has successfully helped discover a new class of thermoelectric materials from chemical whitespace, and the new materials exhibit surprising thermoelectric performance given the metal composition ($RE_{12}Co_5Bi$, $RE =$ Gd, Er). Given the process of materials discovery through good fortune and keen observation is very time-consuming and leads to sporadic periods of rapid growth followed by slow optimization, computer-aided materials discovery may provide the ability to systematically explore and discover unknown chemistries as well as increase the rate of material discovery and technological progress.

A fundamental limitation to approaches based on computer learning models may be the sensitive nature of some physical properties with respect to doping. For example, the electrical resistivity of materials is incredibly sensitive to electronic dopants and defects. While computer learning models are excellent at capturing broad changes in properties that occur with large changes in composition, these models are unsuitable for predicting the dramatic changes in the properties of oxides that can happen with small amounts of dopant. For example, while $SrTiO_3$ is an electronic insulator, it becomes metallic with 0.03% to 0.1% Nb on the Ti site [266].

The complex nature of correlated oxides will remain a challenge, but future work will greatly benefit from incorporating data concerning the crystal structure of materials. Combining the compositional data currently available with crystallographic data available in structural databases will add more descriptors to create more robust predictive models. Considering relatively simple structural descriptors will be easy to implement and may prove useful, and more complicated models examining the atomic connectivity may provide a more universal and robust approach that correlates strongly with physical properties.

Bibliography

[1] T. M. Tritt and M. A. Subramanian, *Thermoelectric materials, phenomena, and applications: A bird's eye view*, *MRS Bull.* **31** (2006), no. 3 188–194. MRS Bull.

[2] J. R. Sootsman, D. Y. Chung, and M. G. Kanatzidis, *New and old concepts in thermoelectric materials*, *Angew. Chem. Int. Ed.* **48** (2009), no. 46 8616–8639.

[3] K. F. Hsu, S. Loo, F. Guo, W. Chen, J. S. Dyck, C. Uher, T. Hogan, E. K. Polychroniadis, and M. G. Kanatzidis, *Cubic $AgPb_mSbTe_{2+m}$: Bulk thermoelectric materials with high figure of merit*, *Science* **303** (2004), no. 5659 818–821.

[4] K. Biswas, J. He, I. D. Blum, C.-I. Wu, T. P. Hogan, D. N. Seidman, V. P. Dravid, and M. G. Kanatzidis, *High-performance bulk thermoelectrics with all-scale hierarchical architectures*, *Nature* **489** (2012), no. 7416 414–418.

[5] G. S. Kumar, G. Prasad, and R. O. Pohl, *Experimental determinations of the Lorenz number*, *J. Mater. Sci.* **28** (1993), no. 16 4261–4272.

[6] G. J. Snyder and E. S. Toberer, *Complex thermoelectric materials*, *Nat. Mater.* **7** (2008), no. 2 105–114.

[7] R. D. Shannon, *Revised effective ionic radii and systematic studies of interatomic distances in halides and chalcogenides*, *Acta Crystallogr.* **32** (1976), no. SEP1 751–767. Acta Crystallogr., Sect. A: Cryst. Phys., Diffr., Theor. Gen. Crystallogr.

[8] M. A. Subramanian, G. Aravamudan, and G. V. S. Rao, *Oxide pyrochlores - a review*, *Prog. Solid State Chem.* **15** (1983), no. 2 55–143. Prog. Solid State Chem.

[9] L. Q. Li and B. J. Kennedy, *Structural and electronic properties of the Ru pyrochlores $Bi_{2-y}Yb_yRu_2O_{7-\delta}$*, *Chem. Mater.* **15** (2003), no. 21 4060–4067. Chem. Mater.

[10] T. Yamamoto, R. Kanno, Y. Takeda, O. Yamamoto, Y. Kawamoto, and M. Takano, *Crystal structure and metal-semiconductor transition of the $Bi_{2-x}Ln_xRu_2O_7$ pyrochlores (Ln = Pr-Lu)*, *J. Solid State Chem.* **109** (1994), no. 2 372–383.

[11] R. Kanno, Y. Takeda, T. Yamamoto, Y. Kawamoto, and O. Yamamoto, *Crystal structure and electrical properties of the pyrochlore ruthenate $Bi_{2-x}Y_xRu_2O_7$*, *J. Solid State Chem.* **102** (1993), no. 1 106–114.

[12] R. J. Bouchard and J. L. Gillson, *A new family of bismuth - precious metal pyrochlores*, *Mater. Res. Bull.* **6** (1971), no. 8 669–680.

[13] S. Munoz-Perez, R. Cobas, J. M. Cadogan, J. Albino Aguiar, P. Bonville, T. Puig, and X. Obradors, *Metallic state induced in $Eu_2Ru_2O_7$ by hole creation and orbital overlap in the t_{2g} bands*, *J. Appl. Phys.* **111** (2012), no. 7 07E150 (3pp).

[14] R. A. Beyerlein, H. S. Horowitz, and J. M. Longo, *The electrical properties of $A_2[Ru_{2-x}A_x]O_{7-y}$ (A = Pb or Bi) pyrochlores as a function of composition and temperature*, *J. Solid State Chem.* **72** (1988), no. 1 2–13.

[15] A. W. Sleight and R. J. Bouchard, *Solid State Chem.: Proc. 5th Mater. Res. Symp., NBS Special Publication* **364** (1972) 227–232.

[16] K. S. Lee, D. K. Seo, and M. H. Whangbo, *Structural and electronic factors governing the metallic and nonmetallic properties of the pyrochlores $A_2Ru_2O_{7-y}$*, *J. Solid State Chem.* **131** (1997), no. 2 405–408.

[17] J. B. Torrance, P. Lacorre, A. I. Nazzal, E. J. Ansaldo, and C. Niedermayer, *Systematic study of insulator-metal transitions in perovskites $RNiO_3$ (R = Pr, Nd, Sm, Eu) due to closing of charge-transfer gap*, *Phys. Rev. B* **45** (1992), no. 14 8209–8212.

[18] G. Catalan, *Progress in perovskite nickelate research*, *Phase Transitions* **81** (2008), no. 7-8 729–749.

[19] R. A. Mohan Ram, L. Ganapathi, P. Ganguly, and C. N. R. Rao, *Evolution of three-dimensional character across the $La_{n+1}Ni_nO_{3n+1}$ homologous series with increase in n*, *J. Solid State Chem.* **63** (1986), no. 2.

[20] S. N. Ruddlesden and P. Popper, *The compounds $Sr_3Ti_2O_7$ and its structure*, *Acta Crystallogr.* **11** (1958), no. 1 54–55.

[21] M. R. Winter and D. R. Clarke, *Oxide materials with low thermal conductivity*, *J. Am. Ceram. Soc.* **90** (2007), no. 2 533–540.

[22] J. S. Anderson and R. J. D. Tilley, *Crystallographic shear and non-stoicheiometry*, in *Surface and defect properties of solids* (M. W. Roberts and J. M. Thomas, eds.), vol. 3, pp. 1–56. The Royal Society of Chemistry, 1974.

[23] E. S. Toberer, L. L. Baranowski, and C. Dames, *Advances in thermal conductivity*, *Annu. Rev. Mater. Res.* **42** (2012) 179–209.

[24] M. G. Kanatzidis, *Nanostructured thermoelectrics: The new paradigm?*, *Chem. Mater.* **22** (2010), no. 3 648–659.

[25] H. J. Snaith, *Perovskites: The emergence of a new era for low-cost, high-efficiency solar cells*, *J. Phys. Chem. Lett.* **4** (2013), no. 21 3623–3630.

[26] I. Terasaki, Y. Sasago, and K. Uchinokura, *Large thermoelectric power in* $NaCo_2O_4$ *single crystals*, *Phys. Rev. B* **56** (1997), no. 20 R12685–R12687.

[27] Y. Kamihara, T. Watanabe, M. Hirano, and H. Hosono, *Iron-Based Layered Superconductor* $La[O_{1-x}F_x]FeAs$ *(x = 0.05–0.12) with* $T_c = 26\,K$, *J. Am. Chem. Soc.* **130** (2008), no. 11 3296–3297.

[28] G. S. Nolas, J. Sharp, and H. J. Goldsmid, *Thermoelectrics: Basic principles and new materials developments.* No. 45 in Springer series in materials science. Springer, Berlin, 2001.

[29] G. S. Nolas, J. Poon, and M. Kanatzidis, *Recent developments in bulk thermoelectric materials*, *MRS Bull.* **31** (2006), no. 3 199–205.

[30] J. E. Garay, *Current-activated, pressure-assisted densification of materials*, *Annu. Rev. Mater. Res.* **40** (2010) 445–468.

[31] R. S. Roth and A. D. Wadsley, *Multiple phase formation in the binary system* Nb_2O_5*–*WO_3*. I. Preparation and identification of phases*, *Acta Crystallogr.* **19** (1965) 26–32.

[32] M. W. Gaultois, P. T. Barton, C. S. Birkel, L. M. Misch, E. E. Rodriguez, G. D. Stucky, and R. Seshadri, *Structural disorder, magnetism, and electrical and thermoelectric properties of pyrochlore* $Nd_2Ru_2O_7$, *J. Phys.: Cond. Matter* **25** (2013) 186004 (10pp).

[33] P. A. Cox, R. G. Egdell, J. B. Goodenough, A. Hamnett, and C. C. Naish, *The metal-to-semiconductor transition in ternary ruthenium (IV) oxides: A study by electron spectroscopy*, *J. Phys. C: Solid State Phys.* **16** (1983), no. 32 6221–6239.

[34] D. P. Shoemaker, R. Seshadri, M. Tachibana, and A. L. Hector, *Incoherent Bi off-centering in* $Bi_2Ti_2O_6O\prime$ *and* $Bi_2Ru_2O_6O\prime$*: Insulator versus metal*, *Phys. Rev. B* **84** (2011), no. 6 064117 (6pp).

[35] J. S. Gardner, M. J. P. Gingras, and J. E. Greedan, *Magnetic pyrochlore oxides*, *Rev. Mod. Phys.* **82** (2010), no. 1 53–107.

[36] N. Taira, M. Wakeshima, and Y. Hinatsu, *Magnetic properties of ruthenium pyrochlores* $R_2Ru_2O_7$ *(R = rare earth)*, *J. Phys.: Condens. Matter* **11** (1999), no. 36 6983–6990.

[37] N. Taira, M. Wakeshima, and Y. Hinatsu, *Specific heat and ac susceptibility studies on ruthenium pyrochlores $R_2Ru_2O_7$ (R = Rare earths)*, *J. Solid State Chem.* **152** (2000), no. 2 441–446.

[38] M. Ito, Y. Yasui, M. Kanada, H. Harashina, S. Yoshii, K. Murata, M. Sato, H. Okumura, and K. Kakurai, *Neutron diffraction study of pyrochlore compound $R_2Ru_2O_7$ (R = Y, Nd) above and below the spin freezing temperature*, *J. Phys. Soc. Jpn.* **69** (2000), no. 3 888–894.

[39] M. Ito, Y. Yasui, M. Kanada, H. Harashina, S. Yoshii, K. Murata, M. Sato, H. Okumura, and K. Kakurai, *Nature of spin freezing transition of geometrically frustrated pyrochlore system $R_2Ru_2O_7$ (R = rare earth elements and Y)*, *J. Phys. Chem. Solids* **62** (2001), no. 1-2 337–341.

[40] J. He, Y. Liu, and R. Funahashi, *Oxide thermoelectrics: The challenges, progress, and outlook*, *J. Mater. Res.* **26** (2011), no. 15 1762–1772.

[41] S. E. Skrabalak and K. S. Suslick, *Porous carbon powders prepared by ultrasonic spray pyrolysis*, *J. Am. Chem. Soc.* **128** (2006), no. 39 12642–12643.

[42] L. M. Misch, J. A. Kurzman, A. R. Derk, Y.-I. Kim, R. Seshadri, H. Metiu, E. W. McFarland, and G. D. Stucky, *C-H Bond activation by Pd-substituted CeO_2: Substituted ions versus reduced species*, *Chem. Mater.* **23** (2011), no. 24 5432–5439.

[43] J. Wang, B. H. Toby, P. L. Lee, L. Ribaud, S. M. Antao, C. Kurtz, M. Ramanathan, R. B. Von Dreele, and M. A. Beno, *A dedicated powder diffraction beamline at the Advanced Photon Source: Commissioning and early operational results*, *Rev. Sci. Instrum.* **79** (2008), no. 8 085105 (7pp).

[44] X. Qiu, J. W. Thompson, and S. J. L. Billinge, *PDFgetX2: a GUI-driven program to obtain the pair distribution function from X-ray powder diffraction data*, *J. Appl. Crystallogr.* **37** (2004), no. 4 678–678.

[45] C. L. Farrow, P. Juhas, J. W. Liu, D. Bryndin, E. S. Bozin, J. Bloch, T. Proffen, and S. J. L. Billinge, *PDFfit2 and PDFgui: Computer programs for studying nanostructure in crystals*, *J. Phys.: Condens. Matter* **19** (2007), no. 33 335219 (7pp).

[46] T. A. Vanderah, I. Levin, and M. W. Lufaso, *An unexpected crystal-chemical principle for the pyrochlore structure*, *Eur. J. Inorg. Chem.* **2005** (2005), no. 14 2895–2901.

[47] G. C. Lau, B. D. Muegge, T. M. McQueen, E. L. Duncan, and R. J. Cava, *Stuffed rare earth pyrochlore solid solutions*, *J. Solid State Chem.* **179** (2006), no. 10 3126–3135.

[48] K. A. Ross, T. Proffen, H. A. Dabkowska, J. A. Quilliam, L. R. Yaraskavitch, J. B. Kycia, and B. D. Gaulin, *Lightly stuffed pyrochlore structure of single-crystalline $Yb_2Ti_2O_7$ grown by the optical floating zone technique*, *Phys. Rev. B* **86** (2012), no. 17 174424.

[49] M. Avdeev, M. K. Haas, J. D. Jorgenson, and R. J. Cava, *Static disorder from lone-pair electrons in $Bi_{2-x}M_xRu_2O_{7-y}$ (M = Cu, Co; x = 0, 0.4) pyrochlores*, *J. Solid State Chem.* **169** (2002), no. 1 24–34.

[50] B. J. Kennedy and T. Vogt, *Structural and bonding trends in ruthenium pyrochlores*, *J. Solid State Chem.* **126** (1996), no. 2 261–270.

[51] G. Baldinozzi, J. F. Berar, M. Gautier-Soyer, and G. Calvarin, *Segregation and site selectivity in Zr-doped Y_2O_3*, *J. Phys.: Condens. Matter* **9** (1997), no. 45 9731–9744.

[52] K. Momma and F. Izumi, *VESTA 3 for three-dimensional visualization of crystal, volumetric and morphology data*, *J. Appl. Crystallogr.* **44** (2011) 1272–1276.

[53] M. Field, B. J. Kennedy, and B. A. Hunter, *Structural studies of the metal-nonmetal transition in Ru pyrochlores*, *J. Solid State Chem.* **151** (2000), no. 1 25–30. J. Solid State Chem.

[54] V. F. Sears, *Neutron scattering lengths and cross sections*, *Neutron News* **3** (1992), no. 3 26–37.

[55] W. C. Hamilton, *Significance tests on the crystallographic R factor*, *Acta Crystallogr.* **18** (1965) 502–510.

[56] J. A. Kurzman, X. Ouyang, W. Bin Im, J. Li, J. Hu, S. L. Scott, and R. Seshadri, *La_4LiAuO_8 and La_2BaPdO_5: Comparing two highly stable d^8 square-planar oxides*, *Inorg. Chem.* **49** (2010), no. 10 4670–4680.

[57] B. C. Melot, J. E. Drewes, R. Seshadri, E. M. Stoudenmire, and A. P. Ramirez, *Magnetic phase evolution in the spinel compounds $Zn_{1-x}Co_xCr_2O_4$*, *J. Phys.: Condens. Matter* **21** (2009), no. 21 216007.

[58] A. P. Ramirez, *Strongly geometrically frustrated magnets*, *Annu. Rev. Mater. Sci.* **24** (1994) 453–480.

[59] N. Taira, M. Wakeshima, Y. Hinatsu, A. Tobo, and K. Ohoyama, *Magnetic structure of pyrochlore-type $Er_2Ru_2O_7$*, *J. Solid State Chem.* **176** (2003), no. 1 165–169.

[60] J. S. Gardner and G. Ehlers, *Magnetic order and crystal field excitations in $Er_2Ru_2O_7$: A neutron scattering study*, *J. Phys.: Condens. Matter* **21** (2009), no. 43 436004.

[61] J. Gurgul, M. Rams, Z. Swiatkowska, R. Kmiec, and K. Tomala, *Bulk magnetic measurements and* ^{99}*Ru and* ^{155}*Gd Mossbauer spectroscopies of* $Gd_2Ru_2O_7$, *Phys. Rev. B* **75** (2007), no. 6 064426 (8pp).

[62] M. Tachibana, Y. Kohama, T. Atake, and E. Takayama-Muromachi, *Heat capacity of pyrochlore* $Pr_2Ru_2O_7$, *J. Appl. Phys.* **101** (2007), no. 9 09D502 (3pp).

[63] N. F. Mott, *Conduction in glasses containing transition metal ions*, *J. Non-Cryst. Solids* **1** (1968), no. 1 1–17.

[64] R. Rosenbaum, N. V. Lien, M. R. Graham, and M. Witcomb, *A useful Mott-Efros-Shklovskii resistivity crossover formulation for three-dimensional films*, *J. Phys.: Condens. Matter* **9** (1997), no. 29 6247–6256.

[65] R. Kmiec, Z. Swiatkowska, J. Gurgul, M. Rams, A. Zarzycki, and K. Tomala, *Investigation of the magnetic properties of* $Y_2Ru_2O_7$ *by* ^{99}*Ru Mossbauer spectroscopy*, *Phys. Rev. B* **74** (2006), no. 10 104425 (9pp).

[66] K. H. Fischer, *Spin-glasses (II)*, *Phys. Status Solidi B* **130** (1985), no. 1 13–71.

[67] K. Binder and A. P. Young, *Spin glasses: Experimental facts, theoretical concepts, and open questions*, *Rev. Mod. Phys.* **58** (1986), no. 4 801–976.

[68] D. Harada, Y. Hinatsu, and Y. Ishii, *Studies on the magnetic and structural phase transitions of* Nd_3RuO_7, *J. Phys.: Condens. Matter* **13** (2001), no. 48 10825–10836.

[69] T. Takeda, M. Nagata, H. Kobayashi, R. Kanno, Y. Kawamoto, and M. Takano, *High-pressure synthesis, crystal structure, and metal-semiconductor transitions in the* $Tl_2Ru_2O_{7-\delta}$ *pyrochlore*, *J. Solid State Chem.* **140** (1998), no. 2 182–193.

[70] F. Ishii and T. Oguchi, *Electronic band structure of the pyrochlore ruthenium oxides* $A_2Ru_2O_7$ *(A = Bi, Tl and Y)*, *J. Phys. Soc. Jpn.* **69** (2000), no. 2 526–531.

[71] M. Tachibana, Y. Kohama, T. Shimoyama, A. Harada, T. Taniyama, M. Itoh, H. Kawaji, and T. Atake, *Electronic properties of the metallic pyrochlore ruthenates* $Pb_2Ru_2O_{6.5}$ *and* $Bi_2Ru_2O_7$, *Phys. Rev. B* **73** (2006), no. 19 193107 (4pp).

[72] L. Cai, A. L. Arias, and J. C. Nino, *The tolerance factors of the pyrochlore crystal structure*, *J. Mater. Chem.* **21** (2011), no. 11 3611–3618. J. Mater. Chem.

[73] H. Kobayashi, R. Kanno, Y. Kawamoto, T. Kamiyama, F. Izumi, and A. W. Sleight, *Synthesis, crystal structure, and electrical properties of the pyrochlores* $Pb_{2-x}Ln_xRu_2O_{7-y}$ *(Ln = Nd, Gd)*, *J. Solid State Chem.* **114** (1995), no. 1 15–23.

[74] R. Funahashi, I. Matsubara, H. Ikuta, T. Takeuchi, U. Mizutani, and S. Sodeoka, *An oxide single crystal with high thermoelectric performance in air*, *Jpn. J. Appl. Phys., Part 2* **39** (2000), no. 11B L1127–L1129.

[75] C. B. Vining, W. Laskow, J. O. Hanson, R. R. Vanderbeck, and P. D. Gorsuch, *Thermoelectric properties of pressure-sintered $Si_{0.8}Ge_{0.2}$ thermoelectric alloys*, *J. Appl. Phys.* **69** (1991), no. 8 4333–4340.

[76] E. A. Skrabek and D. S. Trimmer, *Properties of the general TAGS system*, in *CRC Handbook of thermoelectrics* (D. M. Rowe, ed.). CRC Press, Boca Raton, FL, 1995.

[77] Y. Pei, X. Shi, A. LaLonde, H. Wang, L. Chen, and G. J. Snyder, *Convergence of electronic bands for high performance bulk thermoelectrics*, *Nature* **473** (2011), no. 7345 66–69.

[78] G. H. Jonker, *Application of combined conductivity and Seebeck-effect plots for analysis of semiconductor properties*, *Philips Res. Rep.* **23** (1968), no. 2 131–138. Philips Res. Rep.

[79] T. Bak and J. Nowotny, *Semiconducting properties of oxidized and reduced polycrystalline TiO_2. Jonker analysis*, *J. Phys. Chem. C* **115** (2011), no. 19 9746–9752.

[80] Q. Zhu, E. M. Hopper, B. J. Ingram, and T. O. Mason, *Combined Jonker and Ioffe analysis of oxide conductors and semiconductors*, *J. Am. Ceram. Soc.* **94** (2011), no. 1 51–57.

[81] B. C. Sales, D. Mandrus, and R. K. Williams, *Filled skutterudite antimonides: A new class of thermoelectric materials*, *Science* **272** (1996), no. 5266 1325–1328. Science.

[82] L. D. Hicks and M. S. Dresselhaus, *Effect of quantum-well structures on the thermoelectric figure of merit*, *Phys. Rev. B* **47** (1993), no. 19 12727–12731.

[83] M. S. Dresselhaus, G. Chen, M. Y. Tang, R. G. Yang, H. Lee, D. Z. Wang, Z. F. Ren, J. P. Fleurial, and P. Gogna, *New directions for low-dimensional thermoelectric materials*, *Adv. Mater.* **19** (2007), no. 8 1043–1053.

[84] S. M. Kauzlarich, S. R. Brown, and G. J. Snyder, *Zintl phases for thermoelectric devices*, *Dalton Trans.* (2007), no. 21 2099–2107.

[85] K. Biswas, M. S. Good, K. C. Roberts, M. A. Subramanian, and T. J. Hendricks, *Thermoelectric and structural properties of high-performance In-based skutterudites for high-temperature energy recovery*, *J. Mater. Res.* **26** (2011), no. 15 1827–1835.

[86] H. J. Goldsmid, *Introduction to thermoelectricity.* Springer, Heidelberg, 2009.

[87] D. M. Rowe, *CRC Handbook of thermoelectrics.* CRC Press, Boca Raton, FL, 1995.

[88] D. M. Rowe, *Thermoelectrics handbook: Macro to nano.* CRC press, Boca Raton, FL, 2006.

[89] E. W. Bucholz, C. S. Kong, K. R. Marchman, W. G. Sawyer, S. R. Phillpot, S. B. Sinnott, and K. Rajan, *Data-driven model for estimation of friction coefficient via informatics methods*, *Tribol. Lett.* **47** (2012), no. 2 211–221.

[90] C. S. Kong, P. Villars, S. Iwata, and K. Rajan, *Mapping the 'materials gene' for binary intermetallic compounds: A visualization schema for crystallographic databases*, *Comput. Sci. Discovery* **5** (2012), no. 1 015004.

[91] S. Curtarolo, G. L. W. Hart, M. B. Nardelli, N. Mingo, S. Sanvito, and O. Levy, *The high-throughput highway to computational materials design*, *Nat. Mater.* **12** (2013), no. 3 191–201.

[92] T. E. Graedel, *On the future availability of the energy metals*, *Annu. Rev. Mater. Res.* **41** (2011) 323–335.

[93] G. Homm and P. J. Klar, *Thermoelectric materials: Compromising between high efficiency and materials abundance*, *Phys. Status Solidi RRL* **5** (2011), no. 9 324–331.

[94] O. C. Herfindahl, *Concentration in the US steel industry.* PhD thesis, Columbia University, 1950.

[95] A. O. Hirschman, *National power and the structure of foreign trade.* California University Press, Berkeley, 1980.

[96] D. Rosenau-Tornow, P. Buchholz, A. Riemann, and M. Wagner, *Assessing the long-term supply risks for mineral raw materials: A combined evaluation of past and future trends*, *Resour. Policy* **34** (2009), no. 4 161–175.

[97] *First Solar, Inc. and subsidiaries form 10-K for the fiscal year ended December 31, 2011*, tech. rep., 2012.

[98] J. A. Huwaldt, *Plot Digitizer*, 2013.

[99] B. Tummers, *DataThief III*, 2006.

[100] U.S. Department of Justice and the Federal Trade Commission, *Horizontal merger guidelines.* 2010.

[101] W. Haynes, ed., *CRC Handbook of chemistry and physics.* CRC Press, Boca Raton, FL, 93 ed., 2012.

[102] J. P. Heremans, V. Jovovic, E. S. Toberer, A. Saramat, K. Kurosaki, A. Charoenphakdee, S. Yamanaka, and G. J. Snyder, *Enhancement of thermoelectric efficiency in PbTe by distortion of the electronic density of states*, *Science* **321** (2008), no. 5888 554–557.

[103] W. Koshibae, K. Tsutsui, and S. Maekawa, *Thermopower in cobalt oxides*, *Phys. Rev. B* **62** (2000), no. 11 6869–6872.

[104] D. J. Singh and D. Kasinathan, *Thermoelectric properties of* Na_xCoO_2 *and prospects for other oxide thermoelectrics*, *J. Electron. Mater.* **36** (2007), no. 7 736–739.

[105] T. Tsubota, M. Ohtaki, K. Eguchi, and H. Arai, *Thermoelectric properties of Al-doped ZnO as a promising oxide material for high-temperature thermoelectric conversion*, *J. Mater. Chem.* **7** (1997), no. 1 85–90.

[106] K. Fujita, T. Mochida, and K. Nakamura, *High-temperature thermoelectric properties of* $Na_xCoO_{2-\delta}$ *single crystals*, *Jpn. J. Appl. Phys., Part 1* **40** (2001), no. 7 4644–4647.

[107] S. Sakurada and N. Shutoh, *Effect of Ti substitution on the thermoelectric properties of (Zr,Hf)NiSn half-Heusler compounds*, *Appl. Phys. Lett.* **86** (2005), no. 8 082105 (3pp).

[108] S. K. Bux, M. T. Yeung, E. S. Toberer, G. J. Snyder, R. B. Kaner, and J. P. Fleurial, *Mechanochemical synthesis and thermoelectric properties of high quality magnesium silicide*, *J. Mater. Chem.* **21** (2011), no. 33 12259–12266.

[109] M. Fukano, T. Iida, K. Makino, M. Akasaka, Y. Oguni, and Y. Takanashi, *Crystal Growth of* Mg_2Si *by the vertical Bridgman method and the doping effect of Bi and Al on thermoelectric characteristics*, *MRS Proc.* **1044** (2007) 1044–U06–13.

[110] D. Y. Chung, T. Hogan, P. Brazis, M. Rocci-Lane, C. Kannewurf, M. Bastea, C. Uher, and M. G. Kanatzidis, $CsBi_4Te_6$*: A high-performance thermoelectric material for low-temperature applications*, *Science* **287** (2000), no. 5455 1024–1027.

[111] H. Anno, M. Hokazono, M. Kawamura, J. Nagao, and K. Matsubara, *Thermoelectric properties of* $Ba_8Ga_xGe_{46-x}$ *clathrate compounds.* 21st International Conference on Thermoelectrics. Long Beach, CA, 2002.

[112] E. S. Toberer, M. Christensen, B. B. Iversen, and G. J. Snyder, *High temperature thermoelectric efficiency in* $Ba_8Ga_{16}Ge_{30}$, *Phys. Rev. B* **77** (2008), no. 7 075203 (8pp).

[113] T. He, J. Z. Chen, H. D. Rosenfeld, and M. A. Subramanian, *Thermoelectric properties of indium-filled Skutterudites*, *Chem. Mater.* **18** (2006), no. 3 759–762.

[114] R. Funahashi, M. Mikami, S. Urata, M. Kitawaki, T. Kouuchi, and K. Mizuno, *High-throughput screening of thermoelectric oxides and power generation modules consisting of oxide unicouples*, *Meas. Sci. Technol.* **16** (2005), no. 1 70–80.

[115] F. J. DiSalvo, *Thermoelectric cooling and power generation*, *Science* **285** (1999), no. 5428 703–706.

[116] D. R. Clarke, *Materials selection guidelines for low thermal conductivity thermal barrier coatings*, *Surf. Coat. Technol.* **163** (2003) 67–74.

[117] G. Grimvall, *Thermophysical properties of materials.* Elsevier, Amsterdam, 1 ed., 1999.

[118] J. Lan, Y. Lin, A. Mei, C. Nan, Y. Liu, B. Zhang, and J. Li, *High-temperature electric properties of polycrystalline La-doped* $CaMnO_3$ *ceramics*, *J. Mater. Sci. Technol.* **25** (2009), no. 4 535–538.

[119] J. W. Park, D. H. Kwak, S. H. Yoon, and S. C. Choi, *Thermoelectric properties of Bi, Nb co-substituted* $CaMnO_3$ *at high temperature*, *J. Alloys Compd.* **487** (2009), no. 1-2 550–555.

[120] S. Populoh, M. Trottmann, M. H. Aguire, and A. Weidenkaff, *Nanostructured Nb-substituted* $CaMnO_3$ *n-type thermoelectric material prepared in a continuous process by ultrasonic spray combustion*, *J. Mater. Res.* **26** (2011), no. 15 1947–1952.

[121] Y. Q. Zhou, I. Matsubara, R. Funahashi, G. J. Xu, and M. Shikano, *Influence of Mn-site doped with Ru on the high-temperature thermoelectric performance of* $CaMnO_{3-\delta}$, *Mater. Res. Bull.* **38** (2003), no. 2 341–346.

[122] J. L. Lan, Y. H. Lin, H. Fang, A. Mei, C. W. Nan, Y. Liu, S. L. Xu, and M. Peters, *High-temperature thermoelectric behaviors of fine-grained Gd-doped* $CaMnO_3$ *ceramics*, *J. Am. Ceram. Soc.* **93** (2010), no. 8 2121–2124.

[123] D. Flahaut, T. Mihara, R. Funahashi, N. Nabeshima, K. Lee, H. Ohta, and K. Koumoto, *Thermoelectrical properties of A-site substituted* $Ca_{1-x}Re_xMnO_3$ *system*, *J. Appl. Phys.* **100** (2006), no. 8 084911 (4pp).

[124] T. Kobayashi, H. Takizawa, T. Endo, T. Sato, M. Shimada, H. Taguchi, and M. Nagao, *Metal-insulator transition and thermoelectric properties in the system* $(R_{1-x}Ca_x)MnO_{3-\delta}$ *(R: Tb, Ho, Y)*, *J. Solid State Chem.* **92** (1991), no. 1 116–129.

[125] T. D. Sparks, A. Gurlo, and D. R. Clarke, *Enhanced n-type thermopower in distortion-free* $LiMn_2O_4$, *J. Mater. Chem.* **22** (2012), no. 11 4631–4636.

[126] D. Flahaut, R. Funahashi, K. Lee, H. Ohta, and K. Koumoto, *Effect of the Yb substitutions on the thermoelectric properties of* $CaMnO_3$. 25th International Conference on Thermoelectrics. Vienna, Austria, 2006.

[127] J. Hejtmanek, Z. Jirak, M. Marysko, C. Martin, A. Maignan, M. Hervieu, and B. Raveau, *Interplay between transport, magnetic, and ordering phenomena in* $Sm_{1-x}Ca_xMnO_3$, *Phys. Rev. B* **60** (1999), no. 20 14057–14065.

[128] W. Kobayashi, I. Terasaki, M. Mikami, R. Funahashi, T. Nomura, and T. Katsufuji, *Universal charge transport of the Mn oxides in the high temperature limit*, *J. Appl. Phys.* **95** (2004), no. 11 6825–6827.

[129] M. Ohtaki, H. Koga, T. Tokunaga, K. Eguchi, and H. Arai, *Electrical transport properties and high-temperature thermoelectric performance of* $(Ca_{0.9}M_{0.1})MnO_3$ *(M = Y, La, Ce, Sm, In, Sn, Sb, Pb, Bi)*, *J. Solid State Chem.* **120** (1995), no. 1 105–111.

[130] K. H. Kim, S. H. Shim, K. B. Shim, K. Niihara, and J. Hojo, *Microstructural and thermoelectric characteristics of zinc oxide-based thermoelectric materials fabricated using a spark plasma sintering process*, *J. Am. Ceram. Soc.* **88** (2005), no. 3 628–632.

[131] D. Berardan, E. Guilmeau, A. Maignan, and B. Raveau, In_2O_3*:Ge, a promising n-type thermoelectric oxide composite*, *Solid State Commun.* **146** (2008), no. 1-2 97–101.

[132] E. Guilmeau, A. Maignan, and C. Martin, *Thermoelectric oxides: Effect of doping in Delafossites and zinc oxide*, *J. Electron. Mater.* **38** (2009), no. 7 1104–1108.

[133] S. Hebert, D. Flahaut, C. Martin, S. Lemonnier, J. Noudem, C. Goupil, A. Maignan, and J. Hejtmanek, *Thermoelectric properties of perovskites: Sign change of the Seebeck coefficient and high temperature properties*, *Prog. Solid State Chem.* **35** (2007), no. 2-4 457–467.

[134] Y. Wang, K. H. Lee, H. Ohta, and K. Koumoto, *Thermoelectric properties of electron doped* $SrO(SrTiO_3)_n$ *(n = 1, 2) ceramics*, *J. Appl. Phys.* **105** (2009), no. 10 103701 (6pp).

[135] H. Muta, K. Kurosaki, and S. Yamanaka, *Thermoelectric properties of rare earth doped* $SrTiO_3$, *J. Alloys Compd.* **350** (2003), no. 1-2 292–295.

[136] K. Park, K. Y. Ko, W. S. Seo, W. S. Cho, J. G. Kim, and J. Y. Kim, *High-temperature thermoelectric properties of polycrystalline* $Zn_{1-x-y}Al_xTi_yO$ *ceramics*, *J. Eur. Ceram. Soc.* **27** (2007), no. 2-3 813–817.

[137] M. Sonne, N. van Nong, Z. He, N. Pryds, and S. Linderoth, *8th European Conference on Thermoelectrics.* 2010.

[138] N. Wang, H. C. He, X. A. Li, L. Han, and C. Q. Zhang, *Enhanced thermoelectric properties of Nb-doped $SrTiO_3$ polycrystalline ceramic by titanate nanotube addition*, *J. Alloys Compd.* **506** (2010), no. 1 293–296.

[139] H. Obara, A. Yamamoto, C. H. Lee, K. Kobayashi, A. Matsumoto, and R. Funahashi, *Thermoelectric properties of Y-doped polycrystalline $SrTiO_3$*, *Jpn. J. Appl. Phys., Part 2* **43** (2004), no. 4B L540–L542.

[140] H. Muta, K. Kurosaki, and S. Yamanaka, *Thermoelectric properties of doped $BaTiO_3$–$SrTiO_3$ solid solution*, *J. Alloys Compd.* **368** (2004), no. 1-2 22–24.

[141] P. Jood, R. J. Mehta, Y. Zhang, G. Peleckis, X. Wang, R. W. Siegel, T. Borca-Tasciuc, S. X. Dou, and G. Ramanath, *Al-doped zinc oxide nanocomposites with enhanced thermoelectric properties*, *Nano Lett.* **11** (2011), no. 10 4337–4342.

[142] R. Funahashi and M. Shikano, *$Bi_2Sr_2Co_2O_y$ whiskers with high thermoelectric figure of merit*, *Appl. Phys. Lett.* **81** (2002), no. 8 1459–1461.

[143] K. Iwasaki, T. Ito, T. Nagasaki, Y. Arita, M. Yoshino, and T. Matsui, *Thermoelectric properties of polycrystalline $La_{1-x}Sr_xCoO_3$*, *J. Solid State Chem.* **181** (2008), no. 11 3145–3150.

[144] J. Nan, J. Wu, Y. Deng, and C. W. Nan, *Thermoelectric properties of La-doped Ca-Co-O misfit cobaltites*, *Solid State Commun.* **124** (2002), no. 7 243–246.

[145] M. Shikano and R. Funahashi, *Electrical and thermal properties of single-crystalline $(Ca_2CoO_3)_{0.7}CoO_2$ with a $Ca_3Co_4O_9$ structure*, *Appl. Phys. Lett.* **82** (2003), no. 12 1851–1853.

[146] G. J. Xu, R. Funahashi, M. Shikano, I. Matsubara, and Y. Q. Zhou, *Thermoelectric properties of the Bi- and Na- substituted $Ca_3Co_4O_9$ system*, *Appl. Phys. Lett.* **80** (2002), no. 20 3760–3762.

[147] W. Shin and N. Murayama, *Li-doped nickel oxide as a thermoelectric material*, *Jpn. J. Appl. Phys., Part 2* **38** (1999), no. 11B L1336–L1338.

[148] Y. Q. Zhou, I. Matsubara, R. Funahashi, and S. Sodeoka, *Thermoelectric properties of $Ln_{2-x}Bi_xRu_2O_7$ pyrochlores (Ln = Nd and Yb)*, *Mater. Lett.* **51** (2001), no. 4 347–350. Mater. Lett.

[149] M. Yasukawa, S. Kuniyoshi, and T. Kono, *Thermoelectric properties of the $Bi_{2-x}Y_xRu_2O_7$ (x = 0–2) pyrochlores*, *Solid State Commun.* **126** (2003), no. 4 213–216. Solid State Commun.

[150] M. Yasukawa and N. Murayama, *High-temperature thermoelectric properties of the oxide material:* $Ba_{1-x}Sr_xPbO_3$ *(x = 0–0.6)*, *J. Mater. Sci. Lett.* **16** (1997), no. 21 1731–1734. J. Mater. Sci. Lett.

[151] R. Funahashi, M. Mikami, S. Urata, T. Kouuchi, K. Mizuno, and K. Chong, *Thermoelectric properties of Ni-based oxides*, *MRS Proc.* **793** (2003) S3.3.

[152] C. S. Sanmathi, R. Retoux, and J. G. Noudem, *Thermoelectric properties of nanosized* $Ca_{1-x}Sm_xMnO_3$ *(0.01< x <0.05), synthesised by co-precipitation technique*, in *26th International Conference on Thermoelectrics, 2007. ICT 2007.*, pp. 171–174, 2007.

[153] M. Y. Choi and J. S. Kim, *Thermopower of high-*T_C *cuprates*, *Phys. Rev. B* **59** (1999), no. 1 192–194.

[154] C. Wang, X. Chen, and A. Zhu, *Thermopower and transport mechanism of the* $La_{2-x}Sr_xCu_{0.94}Ti_{0.06}O_4$ *system*, *Solid State Commun.* **152** (2012), no. 12 1067–1071.

[155] H. Takagi, B. Batlogg, H. L. Kao, J. Kwo, R. J. Cava, J. J. Krajewski, and W. F. Peck, *Systematic evolution of temperature-dependent resistivity in* $La_{2-x}Sr_xCuO_4$, *Phys. Rev. Lett.* **69** (1992), no. 20 2975–2978.

[156] X. Dong, H. Wang, Z. Hua, S. Peng, L. Dong, and Y. Wang, *Thermoelectric properties of* WO_3*-based ceramics doped with* Co_2O_3, *J. Mater. Sci.: Mater. Electron.* **23** (2012), no. 6 1210–1214.

[157] H. Kuriyama, M. Nohara, T. Sasagawa, K. Takubo, T. Mizokawa, K. Kimura, and H. Takagi, *High-temperature thermoelectric properties of Delafossite oxide* $CuRh_{1-x}Mg_xO_2$, in *25th International Conference on Thermoelectrics*, pp. 97–98, 2006.

[158] Y. Ono, K. Satoh, T. Nozaki, and T. Kajitani, *Structural, magnetic and thermoelectric properties of Delafossite-type oxide,* $CuCr_{1-x}Mg_xO_2$ *(*$0 \leq x \leq 0.05$*)*, *Jpn. J. Appl. Phys., Part 1* **46** (2007), no. 3A 1071–1075.

[159] N. Tinh and T. Tsuji, *Thermoelectric properties of heavily doped polycrystalline srtio3*, in *Physics and Engineering of New Materials* (D. Cat, A. Pucci, and K. Wandelt, eds.), vol. 127, pp. 209–217. Springer Berlin Heidelberg, 2009.

[160] A. Maignan, V. Eyert, C. Martin, S. Kremer, R. Fresard, and D. Pelloquin, *Electronic structure and thermoelectric properties of* $CuRh_{1-x}Mg_xO_2$, *Phys. Rev. B* **80** (2009), no. 11 115103.

[161] H. Muta, K. Kurosaki, M. Uno, and S. Yamanaka, *Thermoelectric properties of Ti- and Sn-doped* α*-*Fe_2O_3, *J. Alloys Compd.* **335** (2002), no. 1-2 200–202.

[162] K. Kurosaki, H. Kobayashi, and S. Yamanaka, *Thermoelectric properties of Ni- and Zn-doped Nd_2CuO_4*, *J. Alloys Compd.* **350** (2003), no. 1-2 340–343.

[163] S. Lee, R. H. T. Wilke, S. Trolier-McKinstry, S. Zhang, and C. A. Randall, *$Sr_xBa_{1-x}Nb_2O_{6-\delta}$ Ferroelectric-thermoelectrics: Crystal anisotropy, conduction mechanism, and power factor*, *Appl. Phys. Lett.* **96** (2010), no. 3 031910 (3pp).

[164] S. Lee, S. Dursun, C. Duran, and C. A. Randall, *Thermoelectric power factor enhancement of textured ferroelectric $Sr_xBa_{1-x}Nb_2OP_{6-\delta}$ ceramics*, *J. Mater. Res.* **26** (2011), no. 1 26–30.

[165] A. Sakai, T. Kanno, K. Takahashi, A. Omote, H. Adachi, and Y. Yamada, *Thermoelectric responses in layered strontium-niobates via two ways of charge carrier control techniques*, *J. Am. Ceram. Soc.* **95** (2012), no. 5 1750–1755.

[166] G. Joshi, H. Lee, Y. Lan, X. Wang, G. Zhu, D. Wang, R. W. Gould, D. C. Cuff, M. Y. Tang, M. S. Dresselhaus, G. Chen, and Z. Ren, *Enhanced thermoelectric figure-of-merit in nanostructured p-type silicon germanium bulk alloys*, *Nano Lett.* **8** (2008), no. 12 4670–4674.

[167] A. Saramat, G. Svensson, A. E. C. Palmqvist, C. Stiewe, E. Mueller, D. Platzek, S. G. K. Williams, D. M. Rowe, J. D. Bryan, and G. D. Stucky, *Large thermoelectric figure of merit at high temperature in Czochralski-grown clathrate $Ba_8Ga_{16}Ge_{30}$*, *J. Appl. Phys.* **99** (2006), no. 2 023708 (5pp).

[168] B. Wolfing, C. Kloc, J. Teubner, and E. Bucher, *High performance thermoelectric Tl_9BiTe_6 with an extremely low thermal conductivity*, *Phys. Rev. Lett.* **86** (2001), no. 19 4350–4353.

[169] C. Candolfi, U. Aydemir, M. Baitinger, N. Oeschler, F. Steglich, and Y. Grin, *High temperature thermoelectric properties of the type-I clathrate $Ba_8Au_xSi_{46-x}$*, *J. Appl. Phys.* **111** (2012), no. 4 043706.

[170] G. S. Nolas, J. L. Cohn, G. A. Slack, and S. B. Schujman, *Semiconducting Ge clathrates: Promising candidates for thermoelectric applications*, *Appl. Phys. Lett.* **73** (1998), no. 2 178–180.

[171] V. I. Kuznetsov, L. A. Kuznetsova, A. E. Kaliazin, and D. M. Rowe, *Preparation and thermoelectric properties of $A_8^{II}B_{16}^{III}B_{30}^{IV}$ clathrate compounds*, in *18th International Conference on Thermoelectrics*, pp. 177–180, 1999.

[172] J. H. Roudebush, E. S. Toberer, H. Hope, G. J. Snyder, and S. M. Kauzlarich, *Crystal structure, characterization and thermoelectric properties of the type-I clathrate $Ba_{8-y}Sr_yAl_{14}Si_{32}$ ($0.6 \leq y \leq 1.3$) prepared by aluminum flux*, *J. Solid State Chem.* **184** (2011), no. 5 1176–1185.

[173] S. Katsuyama, H. Matsushima, and M. Ito, *Effect of substitution for Ni by Co and/or Cu on the thermoelectric properties of half-Heusler ZrNiSn*, *J. Alloys Compd.* **385** (2004), no. 1-2 232–237. J. Alloy. Compd.

[174] Y. Kimura, Y. Tamura, and T. Kita, *Thermoelectric properties of directionally solidified half-Heusler compound NbCoSn alloys*, *Appl. Phys. Lett.* **92** (2008), no. 1 012105.

[175] H. Muta, T. Kanemitsu, K. Kurosaki, and S. Yamanaka, *High-temperature thermoelectric properties of Nb-doped MNiSn (M = Ti, Zr) half-Heusler compound*, *J. Alloys Compd.* **469** (2009), no. 1-2 50–55.

[176] N. Shutoh and S. Sakurada, *Thermoelectric properties of the* $Ti_x(Zr_{0.5}Hf_{0.5})_{1-x}NiSn$ *half-Heusler compounds*, *J. Alloys Compd.* **389** (2005), no. 1-2 204–208.

[177] J. P. Fleurial, A. Borshchevsky, T. Caillat, D. T. Morelli, and G. P. Meisner, *High figure of merit in Ce-filled skutterudites*, in *15th International Conference on Thermoelectrics*, (Pasadena, CA, USA), pp. 91–95, 1996.

[178] H. Scherrer and S. Scherrer, *Bismuth telluride, antimony telluride, and their solid solutions*, in *CRC Handbook of thermoelectrics* (D. M. Rowe, ed.). CRC Press, Boca Raton, FL, 1995.

[179] D. Y. Chung, K. S. Choi, L. Iordanidis, J. L. Schindler, P. W. Brazis, C. R. Kannewurf, B. X. Chen, S. Q. Hu, C. Uher, and M. G. Kanatzidis, *High thermopower and low thermal conductivity in semiconducting ternary K-Bi-Se compounds. Synthesis and properties of* β-$K_2Bi_8Se_{13}$ *and* $K_{2.5}Bi_{8.5}Se_{14}$ *and their Sb analogues*, *Chem. Mater.* **9** (1997), no. 12 3060–3071.

[180] F. Gascoin and A. Maignan, *Order-disorder transition in* $AgCrSe_2$*: A new route to efficient thermoelectrics*, *Chem. Mater.* **23** (2011), no. 10 2510–2513.

[181] K. Kurosaki, A. Kosuga, and S. Yamanaka, *Thermoelectric properties of chevrel phase* $Mo_6Te_{8-x}S_x$, *J. Alloys Compd.* **351** (2003), no. 1-2 208–211.

[182] M. Ohta, A. Yamamoto, and H. Obara, *Thermoelectric Properties of Chevrel-Phase Sulfides* $M_xMo_6S_8$ *(M: Cr, Mn, Fe, Ni)*, *J. Electron. Mater.* **39** (2010), no. 9 2117–2121.

[183] C. L. Wan, Y. F. Wang, N. Wang, and K. Koumoto, *Low-thermal-conductivity* $(MS)_{1+x}(TiS_2)_2$ *(M = Pb, Bi, Sn) misfit layer compounds for bulk thermoelectric materials*, *Materials* **3** (2010), no. 4 2606–2617.

[184] M. G. Kanatzidis, T. J. McCarthy, T. A. Tanzer, L. H. Chen, L. Iordanidis, T. Hogan, C. R. Kannewurf, C. Uher, and B. X. Chen, *Synthesis and thermoelectric properties of the new ternary bismuth sulfides* $KBi_{6.33}S_{10}$ *and* $K_2Bi_8S_{13}$, *Chem. Mater.* **8** (1996), no. 7 1465–1474.

[185] M. A. McGuire, T. K. Reynolds, and F. J. DiSalvo, *Exploring thallium compounds as thermoelectric materials: Seventeen new thallium chalcogenides*, *Chem. Mater.* **17** (2005), no. 11 2875–2884.

[186] K. Kurosaki, A. Kosuga, H. Muta, M. Uno, and S. Yamanaka, Ag_9TITe_5*: A high-performance thermoelectric bulk material with extremely low thermal conductivity*, *Appl. Phys. Lett.* **87** (2005), no. 6 061919 (3pp).

[187] J. W. Sharp, B. C. Sales, D. G. Mandrus, and B. C. Chakoumakos, *Thermoelectric properties of* Tl_2SnTe_5 *and* Tl_2GeTe_5, *Appl. Phys. Lett.* **74** (1999), no. 25 3794–3796.

[188] H. L. Liu, X. Shi, F. F. Xu, L. L. Zhang, W. Q. Zhang, L. D. Chen, Q. Li, C. Uher, T. Day, and G. J. Snyder, *Copper ion liquid-like thermoelectrics*, *Nat. Mater.* **11** (2012), no. 5 422–425.

[189] A. F. May, E. Flage-Larsen, and G. J. Snyder, *Electron and phonon scattering in the high-temperature thermoelectric* $La_3Te_{4-z}M_z$ *(M = Sb, Bi)*, *Phys. Rev. B* **81** (2010), no. 12 125205.

[190] N. Raghavendra, F. Gascoin, H. Takahashi, S. Hebert, E. Guilmeau, and I. Terasaki, *Thermoelectric properties of Hollandite chalcogenides* AM_5X_8, in *EMRS 2012 Spring Meeting*, (Strasbourg, France), 2012.

[191] K. Mars, H. Ihou-Mouko, G. Pont, J. Tobola, and H. Scherrer, *Thermoelectric properties and electronic structure of Bi- and Ag-doped* $Mg_2Si_{1-x}Ge_x$ *compounds*, *J. Electron. Mater.* **38** (2009), no. 7 1360–1364.

[192] Q. Zhang, X. B. Zhao, H. Yin, and T. J. Zhu, *Thermoelectric performance of* $Mg_{2-x}Ca_xSi$ *compounds*, *J. Alloys Compd.* **464** (2008), no. 1-2 9–12.

[193] M. Ito, T. Tada, and S. Hara, *Thermoelectric properties of hot-pressed* β*-*$FeSi_2$ *with yttria dispersion by mechanical alloying*, *J. Alloys Compd.* **408-412** (2006) 363–367.

[194] M. Akasaka, T. Iida, T. Nemoto, J. Soga, J. Sato, K. Makino, M. Fukano, and Y. Takanashi, *Non-wetting crystal growth of* Mg_2Si *by vertical Bridgman method and thermoelectric characteristics*, *J. Cryst. Growth* **304** (2007), no. 1 196–201.

[195] S. R. Brown, S. M. Kauzlarich, F. Gascoin, and G. J. Snyder, $Yb_{14}MnSb_{11}$*: New high efficiency thermoelectric material for power generation*, *Chem. Mater.* **18** (2006), no. 7 1873–1877.

[196] T. Caillat, J. P. Fleurial, and A. Borshchevsky, *Preparation and thermoelectric properties of semiconducting* Zn_4Sb_3, *J. Phys. Chem. Solids* **58** (1997), no. 7 1119–1125.

[197] H. Kitagawa, H. Noguchi, T. Kiyabu, M. Itoh, and Y. Noda, *Thermoelectric properties of Bi-Sb semiconducting alloys prepared by quenching and annealing*, *J. Phys. Chem. Solids* **65** (2004), no. 7 1223–1227.

[198] E. S. Toberer, P. Rauwel, S. Gariel, J. Tafto, and G. J. Snyder, *Composition and the thermoelectric performance of* β-Zn_4Sb_3, *J. Mater. Chem.* **20** (2010), no. 44 9877–9885.

[199] A. Zevalkink, E. S. Toberer, W. G. Zeier, E. Flage-Larsen, and G. J. Snyder, Ca_3AlSb_3*: An inexpensive, non-toxic thermoelectric material for waste heat recovery*, *Energy Environ. Sci.* **4** (2011), no. 2 510–518.

[200] E. S. Toberer, A. Zevalkink, N. Crisosto, and G. J. Snyder, *The Zintl compound* $Ca_5Al_2Sb_6$ *for low-cost thermoelectric power generation*, *Adv. Funct. Mater.* **20** (2010), no. 24 4375–4380.

[201] A. Naumov, *Rhythms of rhenium*, *Russ. J. Non-Ferrous Met.* **48** (2007), no. 6 418–423.

[202] K. Yazawa and A. Shakouri, *Cost-efficiency trade-off and the design of thermoelectric power generators*, *Environ. Sci. Technol.* **45** (2011), no. 17 7548–7553.

[203] C. J. Vineis, A. Shakouri, A. Majumdar, and M. G. Kanatzidis, *Nanostructured thermoelectrics: Big efficiency gains from small features*, *Adv. Mater.* **22** (2010), no. 36 3970–3980.

[204] D. G. Cahill, S. K. Watson, and R. O. Pohl, *Lower limit to the thermal conductivity of disordered crystals*, *Phys. Rev. B* **46** (1992), no. 10 6131–6140.

[205] M. W. Gaultois, T. D. Sparks, C. K. H. Borg, R. Seshadri, W. D. Bonificio, and D. R. Clarke, *Data-driven review of thermoelectric materials: Performance and resource considerations*, *Chem. Mater.* **25** (2013), no. 15 2911–2920.

[206] G. V. Chester and A. Thellung, *The law of Wiedemann and Franz*, *Proc. Phys. Soc. London* **77** (1961), no. 497 1005–1013.

[207] D. J. Singh, *Doping-dependent thermopower of PbTe from Boltzmann transport calculations*, *Phys. Rev. B* **81** (2010), no. 19 195217 (6pp).

[208] C. Chiritescu, D. G. Cahill, N. Nguyen, D. Johnson, A. Bodapati, P. Keblinski, and P. Zschack, *Ultralow thermal conductivity in disordered, layered* WSe_2 *crystals*, *Science* **315** (2007), no. 5810 351–353.

[209] G. A. Slack, *New materials and performance limits for thermoelectric cooling*, in *CRC Handbook of thermoelectrics* (D. M. Rowe, ed.). CRC Press, Boca Raton, FL, 1995.

[210] G. S. Nolas, G. A. Slack, D. T. Morelli, T. M. Tritt, and A. C. Ehrlich, *The effect of rare-earth filling on the lattice thermal conductivity of skutterudites*, *J. Appl. Phys.* **79** (1996), no. 8 4002–4008.

[211] N. W. Ashcroft and N. D. Mermin, *Solid state physics*. Holt, New York, 1976.

[212] G. A. Slack, *The thermal conductivity of nonmetallic crystals*, in *Solid State Physics* (H. Ehrenreich, F. Seitz, and D. Turnbull, eds.), vol. 34, p. 31. Academic Press, New York, 1979.

[213] E. S. Toberer, A. F. May, and G. J. Snyder, *Zintl chemistry for designing high efficiency thermoelectric materials*, *Chem. Mater.* **22** (2010), no. 3 624–634.

[214] J. E. Douglas, C. S. Birkel, M.-S. Miao, C. J. Torbet, G. D. Stucky, T. M. Pollock, and R. Seshadri, *Enhanced thermoelectric properties of bulk TiNiSn via formation of a $TiNi_2Sn$ second phase*, *Appl. Phys. Lett.* **101** (2012), no. 18 183902 (4pp).

[215] G. Kieslich, I. Veremchuk, I. Antonyshyn, W. G. Zeier, C. S. Birkel, K. Weldert, C. P. Heinrich, E. Visnow, M. Panthoefer, U. Burkhardt, Y. Grin, and W. Tremel, *Using crystallographic shear to reduce lattice thermal conductivity: High temperature thermoelectric characterization of the spark plasma sintered Magneli phases $WO_{2.90}$ and $WO_{2.722}$*, *Phys. Chem. Chem. Phys.* **15** (2013), no. 37 15399–15403.

[216] M. C. Montmory, E. F. Bertaut, and P. Mollard, *Structure magnétique de Cr_2WO_6*, *Solid State Commun.* **4** (1966), no. 5 249–253.

[217] W. Kunnmann, S. Laplaca, L. M. Corliss, J. M. Hastings, and E. Banks, *Magnetic structures of the ordered trirutiles Cr_2WO_6, Cr_2TeO_6 and Fe_2TeO_6*, *J. Phys. Chem. Solids* **29** (1968), no. 8 1359–1364.

[218] R. M. Hornreich, *The magnetoelectric effect: Some likely candidates*, *Solid State Commun.* **7** (1969), no. 15 1081–1085.

[219] Y. Fang, L. Y. Wang, Y. Q. Song, T. Tang, D. H. Wang, and Y. W. Du, *Manipulation of magnetic field on dielectric constant and electric polarization in Cr_2WO_6*, *Appl. Phys. Lett.* **104** (2014), no. 13 132908 (4pp).

[220] T. D. Sparks, M. C. Kemei, P. T. Barton, R. Seshadri, E.-D. Mun, and V. S. Zapf, *Magnetocapacitance as a sensitive probe of magnetostructural changes in $NiCr_2O_4$*, *Phys. Rev. B* **89** (2014), no. 2 024405 (6pp).

[221] P. T. Barton, M. C. Kemei, M. W. Gaultois, S. L. Moffitt, L. E. Darago, R. Seshadri, M. R. Suchomel, and B. C. Melot, *Structural distortion below the Neel temperature in spinel* $GeCo_2O_4$, *Phys. Rev. B* **90** (2014), no. 6 064105 (7pp).

[222] A. A. Coelho, *TOPAS Academic V5*, 2013.

[223] B. H. Toby and R. B. Von Dreele, *GSAS-II: The genesis of a modern open-source all purpose crystallography software package*, *J. Appl. Crystallogr.* **46** (2013) 544–549.

[224] L. Helm, G. M. Nicolle, and A. E. Merbach, *Water and proton exchange processes on metal ions*, *Adv. Inorg. Chem.* **57** (2005) 327–379.

[225] M. Yamaguchi and M. Ishikawa, *Magnetic phase transitions in inverse trirutile-type compounds*, *J. Phys. Soc. Jpn.* **63** (1994), no. 5 1666–1669.

[226] G. Catalan, *Magnetocapacitance without magnetoelectric coupling*, *Appl. Phys. Lett.* **88** (2006), no. 10 102902 (6pp).

[227] T. Kimura, T. Goto, H. Shintani, K. Ishizaka, T. Arima, and Y. Tokura, *Magnetic control of ferroelectric polarization*, *Nature* **426** (2003), no. 6962 55–58.

[228] G. Lawes, B. Melot, K. Page, C. Ederer, M. A. Hayward, T. Proffen, and R. Seshadri, *Dielectric anomalies and spiral magnetic order in* $CoCr_2O_4$, *Phys. Rev. B* **74** (2006), no. 2 024413.

[229] R. Tackett, G. Lawes, B. C. Melot, M. Grossman, E. S. Toberer, and R. Seshadri, *Magnetodielectric coupling in* Mn_3O_4, *Phys. Rev. B* **76** (2007), no. 2 024409 (6pp).

[230] T. Kimura and Y. Tokura, *Magnetoelectric phase control in a magnetic system showing cycloidal/conical spin order*, *J. Phys.: Condens. Matter* **20** (2008), no. 43 434204.

[231] N. Mufti, A. A. Nugroho, G. R. Blake, and T. T. M. Palstra, *Magnetodielectric coupling in frustrated spin systems: The spinels* MCr_2O_4 *(*M *= Mn, Co and Ni)*, *J. Phys.: Condens. Matter* **22** (2010), no. 7 075902 (6pp).

[232] M. C. Montmory and R. Newnham, *Structures magnétiques des composes trirutiles* Cr_2TeO_6 *et* Cr_2WO_6, *Solid State Commun.* **6** (1968), no. 5 323–326.

[233] M. C. Kemei, J. K. Harada, R. Seshadri, and M. R. Suchomel, *Structural change and phase coexistence upon magnetic ordering in the magnetodielectric spinel* Mn_3O_4, *Phys. Rev. B* **90** (2014), no. 6 064418 (8pp).

[234] R. S. Roth and A. D. Wadsley, *Multiple phase formation in the binary system* Nb_2O_5*-*WO_3*. IV. The block principle*, *Acta Crystallogr.* **19** (1965) 42–47.

[235] K. Kato, *Structure refinement of H-Nb_2O_5*, *Acta Crystallogr.* **B32** (1976), no. MAR15 764–767.

[236] C. A. Schneider, W. S. Rasband, and K. W. Eliceiri, *NIH Image to ImageJ: 25 years of image analysis*, *Nat. Methods* **9** (2012), no. 7 671–675.

[237] H. Wang, W. D. Porter, H. Boettner, J. Koenig, L. Chen, S. Bai, T. M. Tritt, A. Mayolet, J. Senawiratne, C. Smith, F. Harris, P. Gilbert, J. W. Sharp, J. Lo, H. Kleinke, and L. Kiss, *Transport properties of bulk thermoelectrics: An international round-robin study, Part I: Seebeck coefficient and electrical resistivity*, *J. Electron. Mater.* **42** (2013), no. 4 654–664.

[238] M. W. Chase, ed., *NIST-JANAF thermochemical tables.* No. 9 in Journal of Physical and Chemical Reference Data. American Chemical Society, Washington, D.C., 4th ed., 1998.

[239] J. Leitner, P. Vonka, D. Sedmidubsky, and P. Svoboda, *Application of Neumann-Kopp rule for the estimation of heat capacity of mixed oxides*, *Thermochim. Acta* **497** (2010), no. 1-2 7–13.

[240] L. M. Clark and R. E. Taylor, *Radiation loss in the flash method for thermal diffusivity*, *J. Appl. Phys.* **46** (1975), no. 2 714–719.

[241] G. Kieslich, C. S. Birkel, J. E. Douglas, M. Gaultois, I. Veremchuk, R. Seshadri, G. D. Stucky, Y. Grin, and W. Tremel, *SPS-assisted preparation of the Magneli phase $WO_{2.90}$ for thermoelectric applications*, *J. Mater. Chem. A* **1** (2013), no. 42 13050–13054.

[242] M. W. Gaultois, M. C. Kemei, J. K. Harada, and R. Seshadri, *Rapid preparation and magnetodielectric properties of trirutile Cr_2WO_6*, *J. Appl. Phys.* **117** (2015), no. 1 014105 (5pp).

[243] R. S. Roth and J. L. Waring, *Phase equilibria as related to crystal structure in the system niobium pentoxide-tungsten trioxide*, *J. Res. Nat. Bur. Stand.* **A70** (1966), no. 4 281–303.

[244] J. G. Allpress, J. V. Sanders, and A. D. Wadsley, *Electron microscopy of high-temperature Nb_2O_5 and related phases*, *Phys. Status Solidi B* **25** (1968), no. 2 541–550.

[245] J. G. Allpress, J. V. Sanders, and A. D. Wadsley, *Multiple phase formation in the binary system Nb_2O_5–WO_3. VI. Electron microscopic observation and evaluation of non-periodic shear structures*, *Acta Crystallogr.* **B25** (1969) 1156–64.

[246] R. Zallen, *The percolation model*, in *The Physics of Amorphous Solids*, pp. 135–204. Wiley-VCH Verlag GmbH, 1998.

[247] J. Carrete, W. Li, N. Mingo, S. Wang, and S. Curtarolo, *Finding unprecedentedly low-thermal-conductivity half-Heusler semiconductors via high-throughput materials modeling*, *Physical Review X* **4** (2014), no. 1 011019 (9 pp).

[248] A. Jain, O. Shyue Ping, G. Hautier, W. Chen, W. D. Richards, S. Dacek, S. Cholia, D. Gunter, D. Skinner, G. Ceder, and K. A. Persson, *Commentary: The Materials Project: A materials genome approach to accelerating materials innovation*, *APL Mater.* **1** (2013), no. 1 011002 (11pp).

[249] B. Meredig, A. Agrawal, S. Kirklin, J. E. Saal, J. W. Doak, A. Thompson, K. Zhang, A. Choudhary, and C. Wolverton, *Combinatorial screening for new materials in unconstrained composition space with machine learning*, *Phys. Rev. B* **89** (2014), no. 9 094104 (7pp).

[250] B. Meredig and C. Wolverton, *Dissolving the periodic table in cubic zirconia: Data mining to discover chemical trends*, *Chem. Mater.* **26** (2014), no. 6 1985–1991.

[251] S. P. Ong, W. D. Richards, A. Jain, G. Hautier, M. Kocher, S. Cholia, D. Gunter, V. L. Chevrier, K. A. Persson, and G. Ceder, *Python Materials Genomics (pymatgen): A robust, open-source python library for materials analysis*, *Comput. Mater. Sci.* **68** (2013) 314–319.

[252] H. Chahboun, D. Groult, M. Hervieu, and B. Raveau, *β-$NbPO_5$ and β-$TaPO_5$: Bronzoïds, second members of the monophosphate tungsten bronze series $(PO_2)_4(WO_3)_{2m}$*, *J. Solid State Chem.* **65** (1986), no. 3 331–342.

[253] H. Chahboun, D. Groult, and B. Raveau, *$TaVO_5$, a novel derivative of the series of monophosphate tungsten bronzes $(PO_2)_4(WO_3)_{2m}$*, *Mater. Res. Bull.* **23** (1988), no. 6 805–812.

[254] M. Greenblatt, *Phosphate tungsten bronzes: A new family of quasi-low-dimensional metallic oxides*, *Int. J. Mod. Phys. B* **7** (1993), no. 23-24 3937–3971.

[255] X. Wang, Q. Huang, J. Deng, R. Yu, J. Chen, and X. Xing, *Phase transformation and negative thermal expansion in $TaVO_5$*, *Inorg. Chem.* **50** (2011), no. 6 2685–2690.

[256] Q. Guo, M. Chan, B. A. Kuropatwa, and H. Kleinke, *Enhanced thermoelectric properties of variants of Tl_9SbTe_6 and Tl_9BiTe_6*, *Chem. Mater.* **25** (2013), no. 20 4097–4104.

[257] L. E. Depero and L. Sangaletti, *Cation sublattice and coordination polyhedra in ABO_4 type of structures*, *J. Solid State Chem.* **129** (1997), no. 1 82–91.

[258] K. M. Ok, N. S. P. Bhuvanesh, and P. S. Halasyamani, *$SbSb_xM_{1x}O_4$ (M = NbV or TaV): Solid solution behavior and second-harmonic generating properties*, *J. Solid State Chem.* **161** (2001), no. 1 57–62.

[259] A. C. Komarek, T. Moeller, M. Isobe, Y. Drees, H. Ulbrich, M. Azuma, M. T. Fernandez-Diaz, A. Senyshyn, M. Hoelzel, G. Andre, Y. Ueda, M. Grueninger, and M. Braden, *Magnetic order, transport and infrared optical properties in the $ACrO_3$ system (A = Ca, Sr, and Pb)*, *Phys. Rev. B* **84** (2011), no. 12 125114 (14pp).

[260] Y. X. Ni, J. M. Hughes, and A. N. Mariano, *Crystal chemistry of the monazite and xenotime structures*, *Am. Mineral.* **80** (1995), no. 1-2 21–26.

[261] A. V. Tkachuk and A. Mar, *Structure and physical properties of ternary rare-earth cobalt bismuth intermetallics $RE_{12}Co_5Bi$ (RE = Y, Gd, Tb, Dy, Ho, Er, Tm)*, *Inorg. Chem.* **44** (2005), no. 7 2272–2281.

[262] T. Graf, C. Felser, and S. S. P. Parkin, *Simple rules for the understanding of Heusler compounds*, *Prog. Solid State Chem.* **39** (2011), no. 1 1–50.

[263] A. I. Hochbaum, R. K. Chen, R. D. Delgado, W. J. Liang, E. C. Garnett, M. Najarian, A. Majumdar, and P. D. Yang, *Enhanced thermoelectric performance of rough silicon nanowires*, *Nature* **451** (2008), no. 7175 163–167. Nature Nature.

[264] P. Jacobsson and B. Sundqvist, *Thermal conductivity and electrical resistivity of gadolinium as functions of pressure and temperature*, *Phys. Rev. B* **40** (1989), no. 14 9541–9551.

[265] T. M. Tritt, *Thermal conductivity: Theory, properties, and applications.* Physics of Solids and Liquids. Springer, 2004.

[266] K. Page, T. Kolodiazhnyi, T. Proffen, A. K. Cheetham, and R. Seshadri, *Local structural origins of the distinct electronic properties of Nb-substituted $SrTiO_3$ and $BaTiO_3$*, *Phys. Rev. Lett.* **101** (2008), no. 20 205502 (4pp).